NORTHWESTERN UNIVERSITY

Emergent Simplicity in Mathematical Models for Morphogenesis

A DISSERTATION

SUBMITTED TO THE GRADUATE SCHOOL
IN PARTIAL FULFILLMENT OF THE REQUIREMENTS

for the degree

DOCTOR OF PHILOSOPHY

Field of Applied Mathematics

By

Siqi Liu

EVANSTON, ILLINOIS

September 2023

© Copyright by Siqi Liu 2023

All Rights Reserved

ABSTRACT

Emergent Simplicity in Mathematical Models for Morphogenesis

Siqi Liu

The simplicity of morphogenesis, manifested as collective shape changes, emerges from complex biophysical regulations within a multicellular embryo. Constructing a spatio-temporal atlas of mechanical stresses is central for understanding the emergence of this simplicity. Developing a new mathematical theory for the static mechanics of three-dimensional multicellular aggregates involving pressures and tensions, I present an image-based approach of inferring forces with high accuracy and robustness. The underlying attributes in the modeling imply the low-dimensionality of morphological geometry space, and the mechanical flexibility of tension allocation. The ensuing mechanical atlas, within the context of ascidian gastrulation, reveals the adiabatic nature of mechanical dynamics, its dependencies on cell-cycle and cell-lineage, and the novel correlations and variations in the spatio-temporal patterns.

Acknowledgements

Foremost, I would like to express my profound gratitude to my advisor, Professor Madhav Mani. His role has not been confined merely to that of an advisor; he has also been a remarkable teacher, an inspiring supervisor, and a steadfast friend. Working alongside him has been an enriching and joyful journey. His wisdom has significantly deepened my comprehension of science and broadened my academic perspectives.

I would also like to extend my heartfelt appreciation to my esteemed collaborators, Professor Edwin Munro and Professor Patrick Lemaire. Their brilliance as biologists and their hands-on assistance have been instrumental throughout my projects. Their teachings have had an indelible impact on my academic growth and professional development.

Lastly, my sincere thanks go to my committee members, Professors Michael Miksis and Petia Vlahovska. Their unwavering guidance throughout my PhD journey and their invaluable academic insights have been pivotal. Their constructive critiques and suggestions have shaped my research trajectory, enhancing my overall academic experience.

The successful completion of this thesis would not have been possible without the mentorship, encouragement, and support of these remarkable individuals. I am fortunate and honored to have had the opportunity to learn from and work with them.

Table of Contents

ABSTRACT 3

Acknowledgements 4

Table of Contents 5

List of Figures 8

Chapter 1. Introduction 11

1.1. Background 11

1.2. Research problem 15

1.3. Overview 19

Chapter 2. Model and Inference for Three-dimensional Cellular Aggregate 21

2.1. Background 21

2.2. Assumptions and models 22

2.3. Geometry in equilibrium 32

2.4. Analytical solutions of mechanics 44

2.5. Numerical scheme 59

2.6. Conclusion 65

Chapter 3. A mechanical atlas of ascidian gastrulation 68

3.1. Background 68

3.2. Geometry reconstruction of ascidian embryo 73

3.3. Patterns of mechanical atlas 78

3.4. Mechanical flexibility in ascidian embryogenesis 91

3.5. Conclusion 98

Chapter 4. Anisotropic Model for Three-dimensional Cellular Aggregate 100

4.1. Background 100

4.2. Anisotropic tension balance on Polyhedral tessellation 101

4.3. Anisotropic force balance on Ellipsoidal-Curved Polyhedral tessellation 111

4.4. Anisotropic force inference 120

Chapter 5. Dynamical model of embryo morphogenesis 122

5.1. Background 122

5.2. Dynamical model on 2d cellular lattice 123

5.3. Dynamical force inference method 126

5.4. Results on drosophila germ-band extension 128

5.5. Mechanical-feedback model based on myosin-driven contractility 130

Chapter 6. Discussion 134

6.1. Summary 134

6.2. Future 135

References 136

Appendix A. The MATLAB codes for numerical schemes 140

A.1. Force inference code 140

A.2. Synthetic analysis 143

Vita 146

List of Figures

2.1 Model and inference of three-dimensional cellular aggregate 22

2.2 Geometry components of three-dimensional cellular aggregate 24

2.3 Mechanical inputs and molecular basis of cellular aggregate 26

2.4 Force directions on faces and edges 27

2.5 Balance between mechanical forces 29

2.6 Mechanical inverse problem 31

2.7 Geometric constraints 34

2.8 Dependency among geometric constraints in Polyhedron tessellation 37

2.9 Dependency among geometric constraints in SCP tessellation 39

2.10 Generalized Weighted Voronoi tessellation in 2d 41

2.11 Divergence theorem in 3d and 2d 45

2.12 Mechanical duality in polygonal tessellation 46

2.13 Dual graph construction in CAP tessellation 47

2.14 Mechanical duality in CAP tessellation 49

2.15 Rescaled dual graph construction 50

2.16 Mechanical duality in Polyhedral tessellation 51

2.17 Mechanical duality in SCP tessellation 53

2.18	Two-cell example of mechanical zero-modes	56
2.19	Images of segmentation	60
2.20	Least-square fitting and synthetic 3d image	61
2.21	Precision and robustness	64
2.22	Summary of physical model and inference method	67
3.1	Developmental stages of ascidian embryo	69
3.2	Early gastrulation of ascidian embryo	70
3.3	Cell fates of ascidian gastrulation	72
3.4	Geometry reconstruction of ascidian embryo	73
3.5	Error distributions of geometry fitting	75
3.6	Improvement of fitting by re-segmentation	76
3.7	Mechanical atlas of ascidian gastrulation	80
3.8	Five groups of ascidian membranes	81
3.9	Reproducible pressure patterns in three embryos	82
3.10	Symmetries and asymmetries of ascidian mechanical patterns	83
3.11	Mechanical atlas of surface tensions in ascidian gastrulation	86
3.12	Correlations between pressures and membrane tensions	87
3.13	Mechanical atlas of line tensions in ascidian gastrulation	88
3.14	Correlations between pressures and line tensions	89
3.15	Lineage map of pressures in ascidian gastrulation	90

3.16 Cellular stress tensor 93
3.17 Flexibility in contractile stress 94
3.18 Von Mises shear stress 96
3.19 Lineage map of pressures relative to ectoderm 97

4.1 Anisotropic surface tension 103
4.2 Membrane anisotropy and cellular anisotropy tensors 106
4.3 Global anisotropy tensor of cellular aggregate 108
4.4 Anisotropic Young-Laplace relation 113
4.5 Analytical solution of anisotropic tension on ellipsoid 117

5.1 Dynamical model on 2d cellular lattice 125
5.2 Robustness of dynamical force inference method 128
5.3 Results on drosophila germ-band extension 129
5.4 Mechanical and geoemtry subspace 131

CHAPTER 1

Introduction

The immeasurable complexity at every level of the nature creates a tough mission for understanding the world. Yet, it is intriguing to observe that the majority of natural systems exhibit remarkable organization and rarely descend into chaos. How does this order materialize amidst such complexity? Mathematical modeling offers a powerful method for navigating this complexity by simplifying objects and their interactions, effectively distilling their core features. In multi-component systems, we often observe the emergence of collective behaviors among the components. Interestingly, this simplicity arises not from the modeling process itself, but rather emerges from the intrinsic properties of the mathematical structures in play. Such phenomena suggest that mathematical structures may provide a gateway to understanding the emergent simplicity from the complex basis of natural systems.

1.1. Background

1.1.1. Morphogenesis

This dissertation delves into the captivating domain of morphogenesis, a natural phenomenon that epitomizes the elegance of simplicity emerging from an intricate foundation. Morphogenesis refers to the biological process that drives an organism or tissue to develop its form and shape [**1**]. This process unfolds through local interactions across cellular contacts by individual cells, guided by genetic and epigenetic information. The emergent phenomenon of the multi-cellular system is the consistent manifestation of well-structured patterns and shapes across diverse organisms, demonstrating robustness essential for current functionality and future growth. The biggest mystery in this field is how these cells collectively collaborate to achieve the formation of organism shape and patterns, exemplifying 'group intelligence' within the living system. This intriguing question draws the attention of scientists from varied disciplines, including applied mathematicians, inspiring them to delve into this subject to decipher this emergence.

There are numerous examples that illuminate this mystery of morphogenesis, one of which is the process of gastrulation in an ascidian embryo. Gastrulation is a critical stage in embryogenesis where the initial round-shape blastula is reorganized into a gastrula, which forms the structure of the gut [**2**]. Ascidians, or sea squirts, have become model organisms for studying this process due to their simple body plan and the highly reproducible and stereotyped nature of their embryonic development [**3**]. During the early stages of ascidian gastrulation, individual cells within the embryo engage in mechanical interactions, causing a specific group of cells - the endoderm - to invaginate and become enveloped by other cells [**4**]. This process results in the embryo taking on a distinctive cup-like shape, setting the stage for gut formation and orchestrating the proper positioning of differentiated cells to evolve into functional organs. Yet, our understanding remains limited regarding how individual cells cooperate to control and direct the embryo in such a complex manner.

Another illustrative example is the germ-band extension in *Drosophila melanogaster*, a well-known model organism commonly referred to as the fruit fly. This stage represents a crucial developmental milestone in the fruit fly's early life [**5**]. During the germ band extension stage, the individual cell mechanics facilitate intercalation, causing the epithelium to elongate along the anterior-posterior axis while simultaneously narrowing along the dorsal-ventral axis. This process ingeniously remodels a short and broad germ band into a long and slender one, a transformative alteration of shape that is vital for the organism's subsequent development. Many scientists are intensely studying this phenomenon in attempt to comprehend how the collective behavior emerges from local interactions between individual cells.

1.1.2. Forces in morphogenesis

For these processes of morphogenesis, we have learned a great deal about the molecular machinery that regulates cell interactions [**6, 7**]. Furthermore, we have started to learn how this machinery's spatial and temporal regulation is orchestrated by programmed gene expression [**8, 9**]. Yet, despite these biochemical signals, as stated in the aforementioned examples, these 'controls' must speak to the common language of mechanical forces to directly cause cell shape changes, cell movements and cell rearrangements. There are principally two types of mechanical forces at play: the adhesion that binds and arranges cells [**10**], and the stress that induces cell shape changes [**11**]. In this dissertation, we only focus on the stress, considering it as the primary interactions between cells.

Mechanical forces play a crucial role in morphogenesis, yet the molecular framework facilitating cellular force generation is complex [**6, 7**]. Active forces within cells are primarily driven by cytoskeletal cortices, a dynamic network of protein filaments [**12**]. Key components of the cytoskeleton, such as actin filaments and microtubules, along with motor proteins like myosin, kinesin, and dynein, contribute fundamentally to this process. For example, myosin motor proteins move along actin filaments, thereby generating contractile forces within cells. Cellular forces are not only limited to active forces but also include passive forces that arise from the intrinsic material properties of cells. For instance, hydrostatic pressures stem from material properties that resist alterations in cell volume [**13**]. Additionally, the viscosity is produced by the material properties that resist movement relative to the substrate [**14**]. The intricate molecular basis of force generation poses significant challenges when attempting to model the forces involved in morphogenesis.

In addition to the intricacies inherent in the molecular basis of force generation, the measurement of mechanical forces across time and space in developing embryos presents a substantial challenge. To address this, a range of experimental methods have been created to quantify forces in living embryos. One broad category of these techniques involves the local exertion of force, such as via local mechanical indentation [**15**], micropipette aspiration [**16, 17**], or optical/magnetic tweezers [**18, 19**]. Alternatively, local disruption of mechanical continuity may be used, such as through laser ablation [**20, 21**]. These interventions are coupled with measurements of subsequent deformations. A corresponding category of methods is centered around the observation of ”force sensors”. These could be molecular FRET sensors, liquid droplets, or elastic beads [**22, 23**], embedded within force-producing tissue, with their deformations serving as indicators of internally generated forces. Significantly, all these techniques necessitate the employment of mathematical models to deduce forces or material properties from observed displacements. These methods have imparted invaluable knowledge regarding the mechanics of cell and tissue morphogenesis across various spatial and temporal scales [**24**]. However, their application is predominantly invasive and/or allows for only sparse sampling at a limited number of locations at a certain time, restricting their utility in charting spatiotemporal patterns of forces pivotal to the collective mechanics of multicellular tissue morphogenesis.

Recent progress in imaging cell and tissue morphologies and deformations within living embryos has fostered the development of a third class of force measurement, typically referred to as image-based force inference methods [**25, 26**]. These methods leverage the shapes of cells within a multicellular aggregate as sensors, utilizing microscopic observations of cell shape and deformation at the tissue-scale to deduce the forces at play. As with the other approaches, image-based force inference method depend on physics-based mathematical models that relate the shapes of cells within a tissue to the nature, organization, and magnitudes of the mechanical forces operating within individual cells and across cell boundaries. The core concept is to address an inverse mechanics problem, aiming to construct a mapping from images of living tissues – the geometries of cells and cell-cell contacts – to the hidden variables such as tensions and pressures, which dictate the mechanical state of a tissue. An essential advantage of image-based approaches is their non-invasive nature, and they inherently present the opportunity to infer forces at many simultaneously observed points within living embryos over time.

1.2. Research problem

1.2.1. Research aims

On the one hand, we aim to quantitatively understand the emergent collective phenomena in morphogenesis, thereby unveiling the intrinsic mathematical properties concealed within the multi-cellular structure. On the other hand, we strive to investigate the mechanical foundation of this biophysical system, taking steps to measure and analyze the magnitude of mechanical forces from real live-image data. Both objectives require the construction of a physics-based mathematical model and the establishment of an force inference method. This will form the core task of our research.

1.2.2. Current studies

Thus far, numerous mathematical models and inference methods have been developed to achieve these research goals. The majority are designed for two-dimensional morphogenesis, primarily applied in the study of epithelial tissues.

The Vertex Model [**27**] is one of the widely employed approaches for simulating cellular dynamics within two-dimensional epithelial tissue. This model represents a tissue as an assembly of interconnected, non-overlapping polygons, where each polygon signifies a cell and its vertices are mobile. The operative driving forces within the model are determined by the derivative of the total elastic energy. These forces counterbalance the viscous drag term, culminating in the differential equation governing the vertices' movements. Through the application of this equation, researchers can simulate vertex movement, providing insights into cell movement and morphological alterations.

Building upon the principles of the Vertex Model, Chiou et al. [**26**] proposed an inference method for a two-dimensional cellular lattice, referred to as the Mechanical Inverse Method. This method primarily presumes that the cellular lattice is in mechanical equilibrium, thereby negating the need for a drag term in the Vertex Model equation. Such an assumption leads to a balance between membrane tensions and pressures at each vertex, giving rise to linear force equations. The coefficients of these equations are determined by membrane directions and curvatures, which can be deduced from microscopic images. To derive the forces, we employ the pseudo-inverse matrix to solve this linear problem. As per experimental results, the Mechanical Inverse Method effectively reconstructs the force patterns within epithelial tissues. Nevertheless, it does exhibit some inaccuracies due to the matrix's lack of full rank, which can compromise the robustness of the numerical scheme.

In response to the issues identified in the Mechanical Inverse Method, Noll et al. [**28**] conducted an in-depth analysis of equilibrium geometry, leading to the formulation of the Active Tension Network Model. This model assumes uniform pressure across all cells, with the membrane tensions serving as the primary determinant of cellular network geometry. They discovered that polygons maintaining force balance must adhere to a specific geometric constraint. This requirement positions the cellular lattice geometry within the realm of Weighted Voronoi tessellations. They further identified an isogonal mode in the balanced system, which unveils the underlying biological principles governing cellular shape.

In addition to the Active Tension Network Model, Noll et al. [**29**] introduced an image-based inference method known as the Variational Method of Stress Inference. This approach accounts for differences in pressure between cells, consequently modeling the two-dimensional cellular lattice as a Circular Arc Polygonal tessellation. Upon investigation of geometric constraints under mechanical equilibrium, they elucidated the dualities between balanced geometry and force maps. To conduct the inference, they utilize the restricted geometry to fit the image data and solve analytically for the pressures and membrane tensions. This method demonstrates superior accuracy and robustness compared to the Mechanical Inverse Method when applied to Drosophila epithelial morphogenesis.

1.2.3. Challenges

While models and inference methods have been largely implemented in two dimensions, it is increasingly apparent that embryos modulate cell and tissue morphology in a three-dimensional context [**30, 31, 32, 9**]. In such scenarios, forces are patterned and exerted in a three-dimensional manner. For instance, intracellular pressures counteract volume change across any direction of the three dimensions. Similarly, in most embryonic tissues, active contractile forces are structured along the cellular membrane surfaces and tri-cellular junction lines, imposing varying types of stress on the multicellular system. Furthermore, the independent regulation of active contractile forces along cell contact surfaces and lines adds to the system's complexity. Consideration of the anisotropy of these forces in three-dimensional space qualitatively increases the complexity of mechanical regulation compared to two-dimensional cases. These challenges render the use of two-dimensional models and inference methods inadequate for attaining the research objectives, highlighting the necessity for more advanced three-dimensional approaches.

Given the rapid advances in imaging approaches that allow capturing high-resolution data on cell boundaries in three-dimensional over time in living embryos [**33, 8**], both the empirical and theoretical challenges have raised up concerning the quantification of three-dimensional geometries from the these images. Mathematically, parameterizing a three-dimensional geometry is a formidable task, coupled with the inherent difficulties in visualizing and conceptualizing three-dimensional objects along with their shapes and adjacencies. This necessitates the utilization of sophisticated pure mathematical tools to address these problems. From a physical standpoint, it remains unclear whether the inverse mechanical problem in three dimensions is a well-defined mathematical problem that allows for the inference of mechanical unknowns from geometric knowns. This level of uncertainty presents a significant challenge in our pursuit to understand the mechanical forces at play in embryonic development.

1.3. Overview

1.3.1. Outlines

In this dissertation, we describe the formulation, implementation, and application of a robust approach to three-dimensional force inference that addresses these challenges.

Chapter 2 lays the mathematical groundwork for the multicellular system in question.It quantifies the geometry of closely-packed cellular clusters as three-dimensional tessellations, and models the mechanical forces acting on this tessellation, including cellular pressures, membrane surface tensions, and junctional line tensions. Employing the quasi-static assumption, we construct the map and inverse map between mechanical and the geometry spaces. We also develop a robust and precise numerical scheme to reconstruct geometry from image data.

Chapter 3 applies the aforementioned force inference method and numerical scheme to live images from the early ascidian gastrulation process. We create an atlas depicting the spatio-temporal patterns of all three types of mechanical forces. By analyzing the mechanical data, we reinforce existing understandings of the design principles, encompassing the symmetries and asymmetries within embryo mechanic patterns. Moreover, we uncover novel insights through the simplicity that emerges from the statistical properties of mechanics.

Beyond the basic model, Chapter 4 takes into account the anisotropy of mechanical stresses, while Chapter 5 considers the dynamics. For both instances, we devise corresponding force inference methods and unveil new principles derived from mathematical models and the inference results on Drosophila germ band extension.

1.3.2. Outcomes

We present a novel, general physical theory of 3D multicellular systems along with a powerful tool for measuring forces within developing embryos. For the first time, we reconstruct and visualize how an ascidian embryo operate the mechanics everywhere over time, providing biological insights into the regulatory origins of gastrulation. The universality of our theory and tools lends them the potential to be applied across a broader spectrum of morphologies, thereby aiding in the theoretical comprehension of the emergent simplicity in general multi-component systems. When combined with current RNA-seq techniques, our approach promises to significantly advance the long-term scientific goal of deciphering the highly complex genotype-to-phenotype map, bringing us closer to a breakthrough in the near future.

CHAPTER 2

Model and Inference for Three-dimensional Cellular Aggregate

2.1. Background

As introduced in Chapter 1, there are many studies about mathematical models on two-dimensional cellular lattice. These mathematical models provide the theories of how mechanical forces control the two-dimensional geometry of cellular lattice. Further more, these models provide the methods of solving the inverse problem: infer the values of mechanical forces from the geometry given by the image data. The image of cellular lattice usually shows the marked cell boundaries. After doing segmentation, the image is processed to be a two-dimensional tessellation from which people can extract the geometry information and do the force inference method.

In this Chapter, we focus on the model for three-dimensional close-packed cellular aggregates in general. The goal is to establish the force inference method that can work on any given three-dimensional segmented image. There are three steps to achieve this goal:

- Build the model which includes the mathematical description of mechanics, geometry and the map from mechanical space to geometry space.
- Construct the method of the inverse problem: map the given geometry back to mechanics.
- Set up a numerical scheme that can fit geometry parameters from image data.

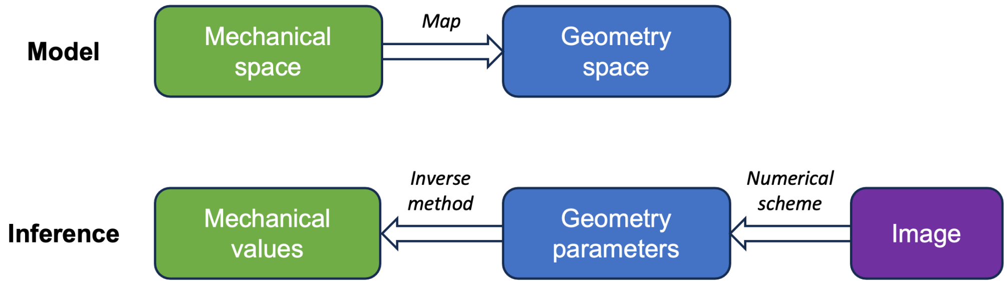
Model
Mechanical space
Map
Geometry space
Inference
Mechanical values
Inverse method
Geometry parameters
Numerical scheme
Image

Figure 2.1. Model and inference of three-dimensional cellular aggregate

2.2. Assumptions and models

To build a mathematical model of this multi-cellular system, we made several assumptions based on the current knowledge in biology. By these assumptions, we simplify cellular aggregates to focus on the main features of geometry (2.2.1) - including cells, membranes, junctions and vertices - and mechanical forces (2.2.2) - pressures, surface tensions and line tensions. We then establish the relations between forces and geometry based on the assumption that the system is in mechanical equilibrium (2.2.3). After building the mathematical model, we illustrate the mechanical inverse problem on the permissible geometry of equilibrium (2.2.4).

2.2.1. Geometry of three-dimensional cellular aggregates

We assume that the main geometry features of three dimensional cellular aggregates controlled by forces in this system are cell shapes. Since the cells are close packed, where the cell shapes depend on the interfaces between neighboring cells, the cell positions and adjacency are also necessary. In order to quantify the topology and geometry of the three dimensional cellular aggregate, we model this system as a tessellation in three-dimensional space.

The components of the three-dimensional tessellation are cells. Each cell occupies a closed region in space, and all the cellular region don't have intersection volume with each other. This is based on the ground fact that cells have boundaries and don't mix their content with each other. We denote the cell indices by Greek letters: α, β, γ, ... We define the cellular region C_α as a set of points $\boldsymbol{r}$ belong to cell α. We use $\boldsymbol{r}$ denoting the position of a general point in space here and in the rest of the manuscript. The volume of cell α is V_α. Specially, we define the background space as a 'cell', denoted as C_0. The background cell is the only cell have infinite volume.

For the interface between two cell regions, we define it as a membrane face. In the biology systems, the interface is composed by to two layer of cell membranes binding together by adhesion proteins. We use $M_{\alpha\beta}$ to denote the membrane face between cell α and cell β. So $M_{\alpha\beta} := C_\alpha \cap C_\beta$, is a set of common points belong to both cells. A membrane face is a two dimensional manifold in 3d space and we ignore the thickness in real biology system. The area of membrane face $M_{\alpha\beta}$ is $A_{\alpha\beta}$.

The boundary of a membrane face is the common boundary among three cell regions, we define it as a junctional edge. In real biology system, the adhesion proteins bind three cell membranes together forming a junction. As shown in Figure 2.2, a junctional edge is also a common edge for three membrane faces. We use $E_{\alpha\beta\gamma}$ to denote the junctional edge of cell α, β and γ. So $E_{\alpha\beta\gamma} := C_\alpha \cap C_\beta \cap C_\gamma = M_{\alpha\beta} \cap F_{\beta\gamma} \cap M_{\gamma\alpha}$. A junctional edge is a one dimensional line in 3d space, with the length $L_{\alpha\beta\gamma}$. We should note that there is

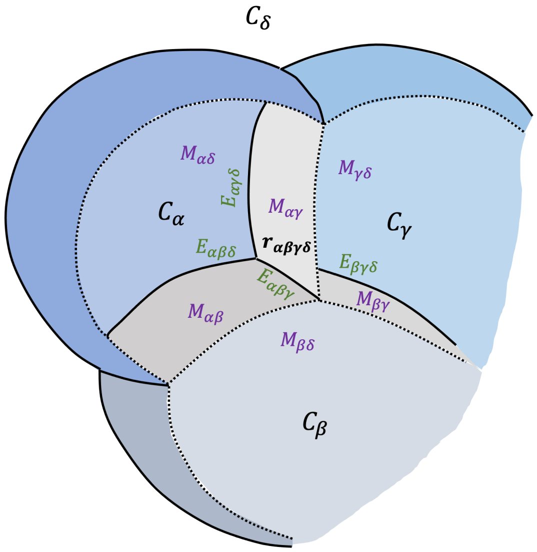
C_δ
$M_{\alpha\delta}$
$E_{\alpha\gamma\delta}$
C_α
$M_{\alpha\gamma}$
$M_{\gamma\delta}$
C_γ
$E_{\alpha\beta\delta}$
$r_{\alpha\beta\gamma\delta}$
$E_{\beta\gamma\delta}$
$E_{\alpha\beta\gamma}$
$M_{\beta\gamma}$
$M_{\alpha\beta}$
$M_{\beta\delta}$
C_β

Figure 2.2. Geometry components of three-dimensional cellular aggregate

a special case that four or more cells have a common edge, like in the cubic tessellation. But we don't take this case include our model, and we treat this edge as two edges very close to each other.

We define the intersections of four cells as a vertex. As shown in Figure 2.2, a vertex is also a common end of four junctional edges, and it is a common point of six membrane faces. We use $\boldsymbol{r}_{\alpha\beta\gamma\delta}$ to denote the position of the vertex of cell α, β, γ and δ. So $\boldsymbol{r}_{\alpha\beta\gamma\delta} := C_\alpha \cap C_\beta \cap C_\gamma \cap C_\delta = M_{\alpha\beta} \cap M_{\alpha\gamma} \cap M_{\alpha\delta} \cap M_{\beta\gamma} \cap M_{\beta\delta} \cap M_{\gamma\delta} = E_{\alpha\beta\gamma} \cap E_{\alpha\beta\delta} \cap E_{\alpha\gamma\delta} \cap E_{\beta\gamma\delta}$. Again we don't take the special case that a vertex corresponds to five or more cells in our model.

The information including the positions, the shapes, and the volumes or areas of cell regions, membrane faces, junctional edges and vertices provide us the topology and geometry of the three-dimensional cellular tessellation. Therefore we have modeled the main geometry features of three-dimensional cellular aggregates.

2.2.2. Mechanical inputs in cellular aggregates

After modeling the geometry of three dimensional cellular aggregates, we need to model the mechanical inputs in this system. Based on the well-understood biological observations, we consider three effective forms of mechanical stress, which correspond to the geometry components - cells, membrane faces and junctional edges - in this system.

First, within each cell region, there exists a field of 3d mechanical stress which is the effective pressure. While the dominant contribution to effective pressure is hydrostatic effects associated with an incompressible fluid-filled cytoplasm, it may also include the isotropic effects of other active cellular processes, such as cytoskeletal assembly and motor activity. Regardless of its manifold and complex molecular origins, or factors that control its magnitude, we consider the effective cellular pressure to be an isotropic stress and to be homogeneous within each single cell volume. Therefore, we can use a single value P_α to represent the effective pressure in cell α. The unit of cell pressure is 'force per area'. As shown in Figure 2.4, for any cellular boundary face element dA of cell α, the effective pressure provides a pushing force with magnitude $P_\alpha dA$ and direction normal to the face pointing outward the cell.

Second, within each membrane face, there is a field of 2d contractile mechanical stress, which is the effective surface tension. A large body of work suggests that the key determinants of surface tension in close packed tissues are contractile forces produced by the

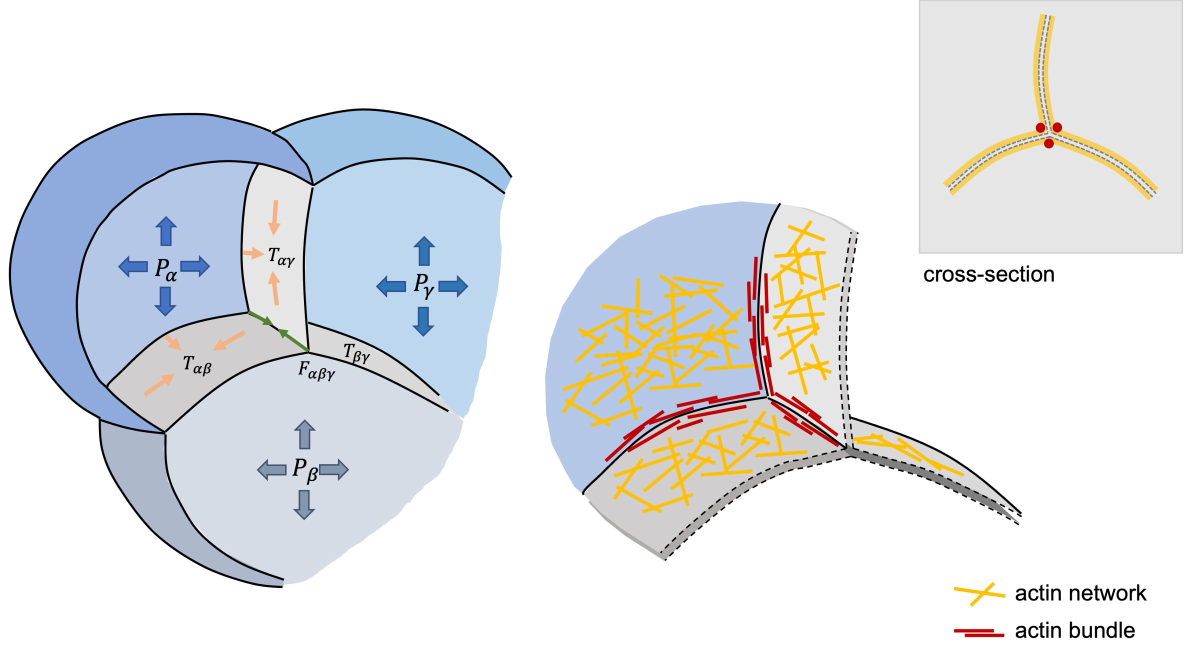
P_α
$T_{\alpha\gamma}$
P_γ
$T_{\alpha\beta}$
$F_{\alpha\beta\gamma}$
$T_{\beta\gamma}$
P_β
cross-section
actin network
actin bundle

Figure 2.3. Mechanical inputs and molecular basis of cellular aggregate

cortical actomyosin cytoskeleton, working against a passive resistance of the cortex to deformation. Again, regardless of the complicated textures of the cytoskeleton, we consider the effective surface tension spreading each membrane face to be an isotropic and homogeneous stress. Therefore, we can use a single value $T_{\alpha\beta}$ denoting the effective surface tension on membrane $M_{\alpha\beta}$. The unit of surface tension is 'force per length'. As shown in Figure 2.4, for any membrane boundary edge element dL of membrane $M_{\alpha\beta}$, the effective surface tension provides a pulling force, which has magnitude of $T_{\alpha\beta}dL$. The direction of the pulling force is normal to the edge and tangent to the membrane face, pointing inward the membrane.

Finally, along each junctional edge, there exist a set of 1d contractile forces, which is the effective line tension. The key determinant of line tensions along cell contacts is

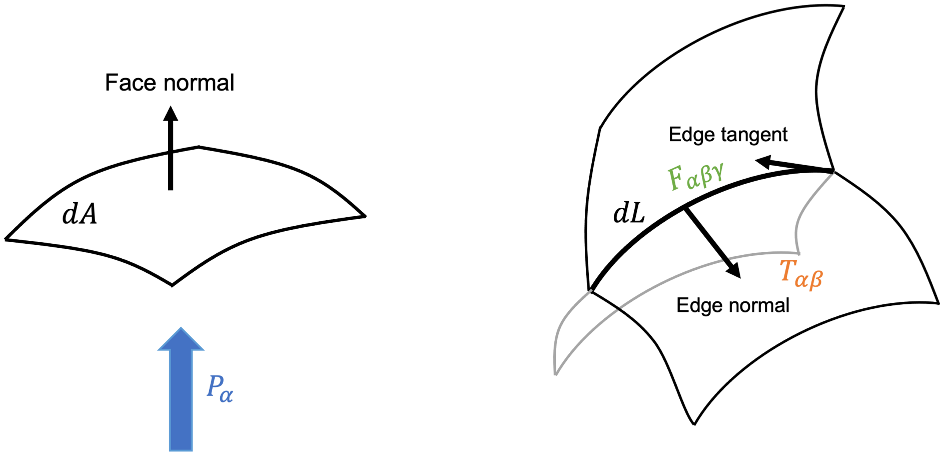

Figure 2.4. Force directions on faces and edges

thought to be contractile forces produced by actomyosin networks that assemble adjacent to cell-cell contact lines. Distinct from the common physical models for soap bubble foams where no line tension exists, there is abundant evidence that a separate mechanism in cellular aggregate controls such 1d contractility independently. We consider the line tension to be homogeneous along each junctional edge $E_{\alpha\beta\gamma}$, which allow us to use a single value $F_{\alpha\beta\gamma}$ for representation. The unit of line tension is just the force unit. As shown in Figure 2.4, at the end vertex of the junctional edge, the force direction is given as the tangential vector toward the line.

In summary, the effective cellular pressures, surface tensions and line tensions consist the mechanical inputs in the system of cellular aggregates. Each of the effective stress within a single geometric component is simplified to be homogeneous and isotropic, represented by a single value of magnitude.

2.2.3. Balance between mechanical forces

In order to model the relations between mechanical forces and geometry, we make an important assumption of force balance based on some experimental facts. First, in a variety of different tissues, the response of shape changing to laser ablation is rapid, which usually takes tens of seconds or less. Comparing to the timescale of morphogenesis, which usually take minutes to hours, it suggests that the mechanical forces are in static equilibrium with each other on these longer timescale. Therefore, the dynamics of morphogenesis can be modeled as a quasi-static process. Second, when the cells probe rapid local active forces to the cytoskeleton, the elastic responses at short timescale are dissipated by cytoskeletal remodeling and turnover at longer timescale. This dissipation results in a fluid-like material properties of cytoskeleton, meaning that there is no strain response in this mechanical system. Taken together, we assume the cellular aggregate is under a mechanical stress field with zero net force everywhere. The mechanical forces in the system are balanced with each other.

With this force balance assumption, we can mathematically express the relations between mechanical inputs and geometry. First, on each membrane face $M_{\alpha\beta}$, we consider the small curved face element square dA with the edge length dL. As shown in Figure 2.5, the cellular pressures P_α and P_β on both sides apply two pushing forces $P_\alpha dA$ and $P_\beta dA$ on the face element with opposite normal direction. On the other hand, the surface tension $T_{\alpha\beta}$ applies on the four edges giving the pulling forces of magnitude $T_{\alpha\beta}dL$. Denoting the curvatures on these two orthogonal directions of the surface as κ_1 and κ_2, the net force of the four tension contractile is $T_{\alpha\beta}dL\kappa_1 dL + T_{\alpha\beta}dL\kappa_2 dL$, which is also in normal direction. Simplifying the balance of pressures and surface tension in normal direction, we get the following equation, which is the well-known Young-Laplace equation:

$$|P_\alpha - P_\beta| = 2T_{\alpha\beta}H_{\alpha\beta}, \tag{2.1}$$

where $H_{\alpha\beta} = (\kappa_1 + \kappa_2)/2$ is the mean curvature of the membrane face. Due to the simplification that pressures and tension are isotropic and homogeneous, the membrane face $M_{\alpha\beta}$ has a constant mean curvature. Therefore, the shape of the membrane face must be a section of sphere or a flat plane.

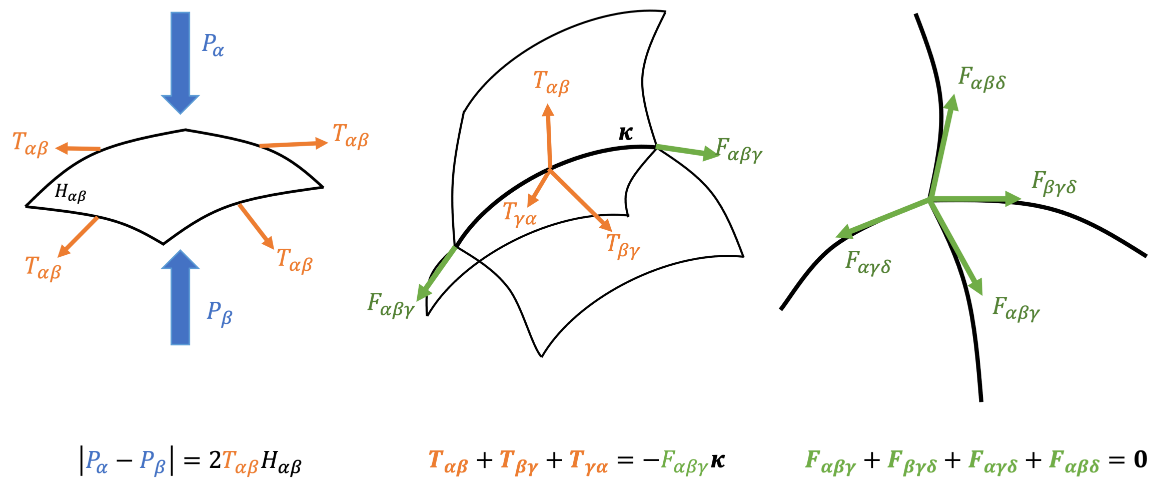
P_α
$T_{\alpha\beta}$
$T_{\alpha\beta}$
$H_{\alpha\beta}$
$T_{\alpha\beta}$
$T_{\alpha\beta}$
P_β
$T_{\alpha\beta}$
$\boldsymbol{\kappa}$
$F_{\alpha\beta\gamma}$
$T_{\gamma\alpha}$
$T_{\beta\gamma}$
$F_{\alpha\beta\gamma}$
$F_{\alpha\beta\delta}$
$F_{\beta\gamma\delta}$
$F_{\alpha\gamma\delta}$
$F_{\alpha\beta\gamma}$
$|P_\alpha - P_\beta| = 2T_{\alpha\beta}H_{\alpha\beta}$
$\boldsymbol{T}_{\alpha\beta} + \boldsymbol{T}_{\beta\gamma} + \boldsymbol{T}_{\gamma\alpha} = -F_{\alpha\beta\gamma}\boldsymbol{\kappa}$
$\boldsymbol{F}_{\alpha\beta\gamma} + \boldsymbol{F}_{\beta\gamma\delta} + \boldsymbol{F}_{\alpha\gamma\delta} + \boldsymbol{F}_{\alpha\beta\delta} = \boldsymbol{0}$

Figure 2.5. Balance between mechanical forces

In a physically and mathematically analogous way, we can mathematicalize the force balance on each junctional edge $E_{\alpha\beta\gamma}$. Consider the line element dL shown in Figure 2.5, the three corresponding membrane surface tensions - $T_{\alpha\beta}$, $T_{\beta\gamma}$ and $T_{\gamma\alpha}$ - give three contractile forces along the curved line: $T_{\alpha\beta}dL\hat{\boldsymbol{n}}_1$, $T_{\beta\gamma}dL\hat{\boldsymbol{n}}_2$ and $T_{\gamma\alpha}dL\hat{\boldsymbol{n}}_3$. Here $\hat{\boldsymbol{n}}_1$, $\hat{\boldsymbol{n}}_2$, $\hat{\boldsymbol{n}}_3$ are unit vectors orthogonal to dL in the tangential plane of membrane $M_{\alpha\beta}$, $M_{\beta\gamma}$,

$M_{\gamma\alpha}$, respectively. At the two ends of dL, the line tension force $F_{\alpha\beta\gamma}$ also applies on the edge along the tangential direction $\hat{\boldsymbol{t}}$. Thus, the junctional balance of force is described by a one-dimensional Young-Laplace equation:

$$T_{\alpha\beta}\hat{\boldsymbol{n}}_1 + T_{\beta\gamma}\hat{\boldsymbol{n}}_2 + T_{\gamma\alpha}\hat{\boldsymbol{n}}_3 = -F_{\alpha\beta\gamma}\boldsymbol{\kappa}_{\alpha\beta\gamma}, \tag{2.2}$$

where $\boldsymbol{\kappa}_{\alpha\beta\gamma} = d\hat{\boldsymbol{t}}/dL$ is the *curvature vector* of the junctional edge. Again, the assumption that line tension is homogeneous along a given junctional edge implies that only edges of constant curvature, i.e. sections of circles (or straight lines), are permissible. With this constraint, the curvature vector $\boldsymbol{\kappa}_{\alpha\beta\gamma}$ is uniquely defined as the vector of constant length pointing towards the center of the circle.

Finally, as shown in Figure 2.5, the four line tensions junctional edge produce forces - $F_{\alpha\beta\gamma}\hat{\boldsymbol{t}}_1$, $F_{\alpha\beta\delta}\hat{\boldsymbol{t}}_2$, $F_{\alpha\gamma\delta}\hat{\boldsymbol{t}}_3$, $F_{\beta\gamma\delta}\hat{\boldsymbol{t}}_4$ - at a vertex $\boldsymbol{r}_{\alpha\beta\gamma\delta}$, along the tangent direction of edges. The assumption that all mechanical forces are in static balance with one another implies that these forces must sum to zero:

$$F_{\alpha\beta\gamma}\hat{\boldsymbol{t}}_1 + F_{\alpha\beta\delta}\hat{\boldsymbol{t}}_2 + F_{\alpha\gamma\delta}\hat{\boldsymbol{t}}_3 + F_{\beta\gamma\delta}\hat{\boldsymbol{t}}_4 = \mathbf{0}. \tag{2.3}$$

Here, $\hat{\boldsymbol{t}}_1$, $\hat{\boldsymbol{t}}_2$, $\hat{\boldsymbol{t}}_3$ and $\hat{\boldsymbol{t}}_4$ are the unit vectors tangent to edge $E_{\alpha\beta\gamma}$, $E_{\alpha\beta\delta}$, $E_{\alpha\gamma\delta}$ and $E_{\beta\gamma\delta}$, respectively.

In summary, equations (2.1)-(2.3) constitute the physical rules for compact 3D cellular aggregates at quasi-static mechanical equilibrium.

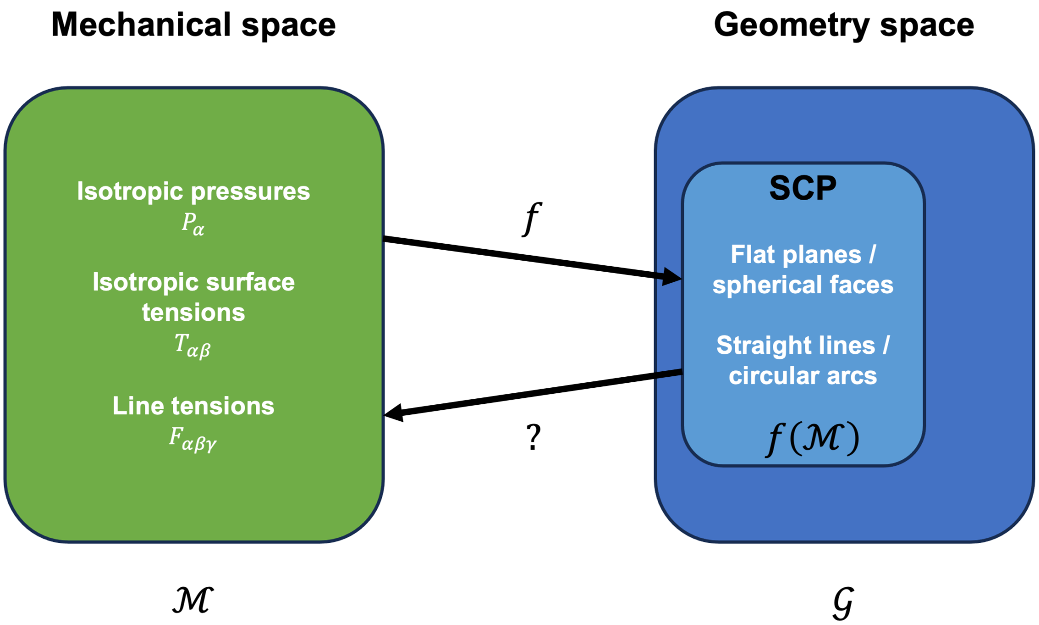
Mechanical space
Geometry space
Isotropic pressures
P_α
Isotropic surface tensions
$T_{\alpha\beta}$
Line tensions
$F_{\alpha\beta\gamma}$
f
?
SCP
Flat planes / spherical faces
Straight lines / circular arcs
$f(\mathcal{M})$
$\mathcal{M}$
$\mathcal{G}$

Figure 2.6. Mechanical inverse problem

2.2.4. The mechanical inverse problem

Based on the simplifications and assumptions, we construct a model that quantifies the mechanical inputs and the multi-cellular geometries. The model also describes how the mechanical forces govern the shapes of cellular aggregates by balancing with each other. Mathematically, we define a map $f : \mathcal{M} \to \mathcal{G}$ from the mechanics space $\mathcal{M}$ to the geometry space $\mathcal{G}$. For the domain $\mathcal{M}$ of isotropic and homogeneous stresses, the range of function $f(\mathcal{M})$ is subset of $\mathcal{G}$. Physically, $f(\mathcal{M})$ is the subspace of permissible geometry under equilibrium, where membrane faces are flat or spherically curved and junctional edges are straight lines or circular arcs. In the most special case, flat surfaces and straight edges imply the shapes of the cells to be polyhedrons, thus the tessellation is polyhedral tessellation. In the general case, the shape of cells are 'polyhedrons' with spherically curved faces, thus are called Spherically-curved polyhedral (SCP) tessellation. Therefore, $f(\mathcal{M})$ is the space of polyhedral or SCP tessellations.

Our goal is the inverse problem of the mechanical map: given the geometric quantities from the microscopic 3d image data, how can we infer the mechanical magnitudes of cellular pressures, membrane tensions and line tensions from the force balance relations? Mathematically, given the geometry parameters in $f(\mathcal{M})$, how to solve the equations (2.1)-(2.3) for solutions of P_α, $T_{\alpha\beta}$ and $F_{\alpha\beta\gamma}$ in mechanical space $\mathcal{M}$? Two more fundamental questions are: a) Does the solution exist or when does it exist? b) Is the solution unique? These require more detailed investigation on this model in the following sections.

2.3. Geometry in equilibrium

We have modeled the map from mechanics to geometry, and noticed that the geometry under equilibrium is restricted to Polyhedral tessellation or Spherically-curved Polyhedral (SCP) tessellation. Before mapping back from geometry to mechanics, we need to first parameterize Polyhedral tessellation and SCP tessellation. However, the ordinary parameters such as vertex positions and surface curvatures are dependent in the two classes of tessellation. There exist intrinsic geometric constraints among the ordinary shape parameters (2.3.2). Finding the independent geometry parameters allows us to: a) fit the image to the permissible tessellations under mechanical equilibrium; b) construct the inverse map to mechanics and investigate the existence and uniqueness of it.

In order to find the independent geometry parameters, we compute how many degrees of freedom under geometric constraints for a Polyhedral tessellation (2.3.2) or a SCP tessellation (2.3.3) with a certain number of cells. Then according to the dimensionality and the geometry constraints, we use Generalize Weighted Voronoi (GWV) tessellation to parameterize Polyhedral and SCP tessellations (2.3.4).

2.3.1. Geometric constraints

We realize that equations (2.1)-(2.3) are linear equations of the unknowns - P_α, $T_{\alpha\beta}$ and $F_{\alpha\beta\gamma}$. The coefficients of the system are geometric quantities - $H_{\alpha\beta}$, $\boldsymbol{\kappa}_{\alpha\beta\gamma}$, $\hat{\boldsymbol{n}}_i$ and $\hat{\boldsymbol{t}}_i$. In Polyhedral or SCP tessellation, these geometric quantities can be determined by ordinary parameters: vertex positions $\boldsymbol{r}_i$, face centroid and radii $\boldsymbol{\rho}_{\alpha\beta}, R_{\alpha\beta}$, or face normals $\hat{\boldsymbol{m}}_{\alpha\beta}$ (if flat). However, these ordinary parameters are not independent with each other. So we first illustrate and quantify the geometric constraints in the system.

In Polygonal tessellation where $H_{\alpha\beta} = 0$ and $\boldsymbol{\kappa}_{\alpha\beta\gamma} = \mathbf{0}$, the ordinary parameters are vertex positions $\boldsymbol{r}_i$ and face normals $\hat{\boldsymbol{m}}_{\alpha\beta}$. Using these parameter, as shown in Figure 2.7, the force directions in equations are given as $\hat{\boldsymbol{t}}_1 = (\boldsymbol{r}_1 - \boldsymbol{r}_0)/|\boldsymbol{r}_1 - \boldsymbol{r}_0|$ and $\hat{\boldsymbol{n}}_1 = \hat{\boldsymbol{m}}_{\alpha\beta} \times \hat{\boldsymbol{t}}_1$. However, we know that three points in space can determine a flat face, but in Polygonal tessellations most faces have more than three vertices, thus they are constrained. We can describe the dependence of ordinary parameters $\boldsymbol{r}_i$ and $\hat{\boldsymbol{m}}_{\alpha\beta}$ as

$$(\boldsymbol{r}_1 - \boldsymbol{r}_0) \cdot \hat{\boldsymbol{m}}_{\alpha\beta} = 0. \tag{2.4}$$

We will count the total number of such constraints in 2.3.2 and find out the independent parameters in 2.3.4.

In SCP tessellation, the ordinary parameters are vertex positions $\boldsymbol{r}_i$ and face centroids and radii $\boldsymbol{\rho}_{\alpha\beta}, R_{\alpha\beta}$. There are two kinds of dependence among these ordinary parameters.

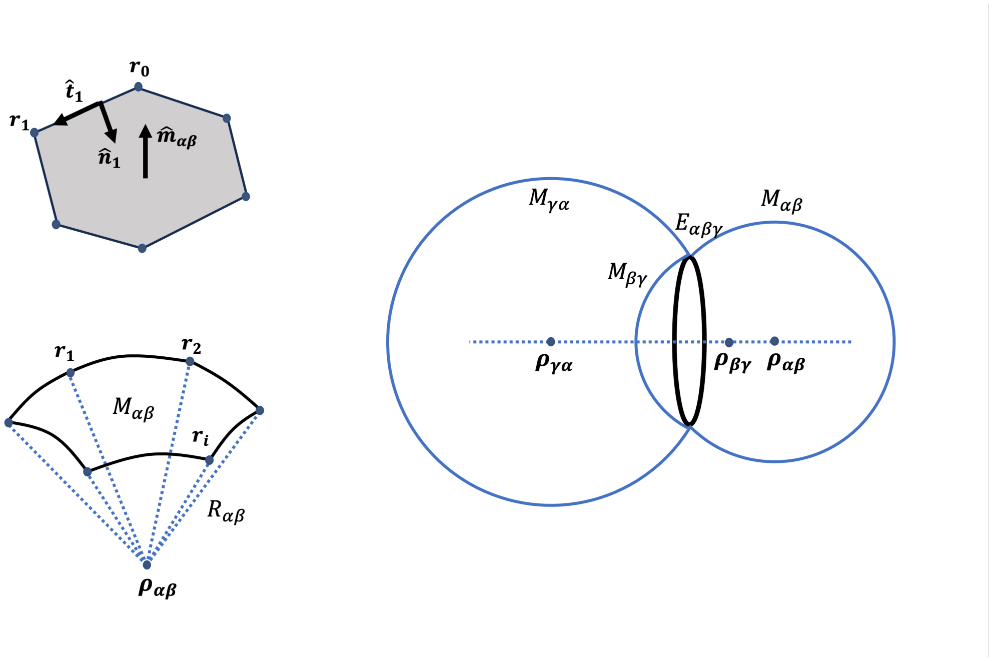
$\boldsymbol{r_0}$
$\hat{\boldsymbol{t}}_1$
$\boldsymbol{r_1}$
$\hat{\boldsymbol{m}}_{\alpha\beta}$
$\hat{\boldsymbol{n}}_1$
$\boldsymbol{r_1}$
$\boldsymbol{r_2}$
$M_{\alpha\beta}$
$\boldsymbol{r_i}$
$R_{\alpha\beta}$
$\boldsymbol{\rho}_{\alpha\beta}$
$M_{\gamma\alpha}$
$E_{\alpha\beta\gamma}$
$M_{\alpha\beta}$
$M_{\beta\gamma}$
$\boldsymbol{\rho}_{\gamma\alpha}$
$\boldsymbol{\rho}_{\beta\gamma}$
$\boldsymbol{\rho}_{\alpha\beta}$

Figure 2.7. Geometric constraints

The trivial geometric constraint is

$$|\boldsymbol{r}_i - \boldsymbol{\rho}_{\alpha\beta}| = R_{\alpha\beta}. \tag{2.5}$$

Consider an edge - a circular arc, it is an intersection of three spheres as shown in Figure 2.7. So the central axis of the circular arc must go through all three corresponding centroids. Thus the three centroid are co-linear. For $\boldsymbol{\rho}_{\alpha\beta}$, $\boldsymbol{\rho}_{\beta\gamma}$ and $\boldsymbol{\rho}_{\gamma\alpha}$, this geometric constraint is given by

$$\boldsymbol{\rho}_{\alpha\beta} - \boldsymbol{\rho}_{\beta\gamma} = \chi_{\alpha\beta\gamma}(\boldsymbol{\rho}_{\alpha\beta} - \boldsymbol{\rho}_{\gamma\alpha}), \tag{2.6}$$

where $\chi_{\alpha\beta\gamma}$ is the ratio. We will count the total number of constraints (2.5) and (2.6) in 2.3.3 and find out the independent parameters in 2.3.4.

2.3.2. Dimensionality of Polyhedral tessellation

Before doing the counting of the number of constraints and the degrees of freedom, let us setup the notations of the numbers and their relations as the following claim.

Claim: We use N_C, N_F, N_E, N_V to denote the number of cells, membrane faces, junctional edges and vertices, respectively. There are two relations among these number in Polyhedral or SCP tessellation:

$$N_E = 2N_V, \tag{2.7}$$

and

$$N_F - N_V = N_C. \tag{2.8}$$

Proof: By the fact that each edge has two vertices and each vertex has four edges, which gives $2N_E = 4N_V$. Then the first relation (2.7) can be directly derived. According to Euler's formula, for each polyhedron cell α we have

$$n_F^{(\alpha)} + n_V^{(\alpha)} - n_E^{(\alpha)} = 2, \tag{2.9}$$

where $n_F^{(\alpha)}$, $n_V^{(\alpha)}$ and $n_E^{(\alpha)}$ denoting the face, edge and vertex numbers for one cell. We then sum the N_C Euler relation across all cells:

$$\sum_\alpha n_F^{(\alpha)} + \sum_\alpha n_V^{(\alpha)} - \sum_\alpha n_E^{(\alpha)} = 2N_C. \tag{2.10}$$

In this summation, each face counts twice, $\sum_\alpha n_F^{(\alpha)} = 2N_F$; each edge counts 3 times, $\sum_\alpha n_E^{(\alpha)} = 3N_E$; each vertex counts 4 times, $\sum_\alpha n_V^{(\alpha)} = 4N_V$. We apply these relations onto (2.10), giving

$$2N_F + 4N_V - 3N_E = 2N_C. \tag{2.11}$$

Using the substitution (2.7) in (2.11), we derive the second relation between the numbers as (2.8). □

Claim: For N_C cells, the dimensionality of Polyhedron tessellation is $4N_C$.

Proof: Consider the ordinary parameters of Polyhedron tessellation, $\boldsymbol{r}_i$ and $\hat{\boldsymbol{m}}_{\alpha\beta}$. The total degrees of them are $3N_V + 2N_F$, because a vertex position is three-dimensional and a face normal is a three-dimensional vector of unit length. Then consider the geometric constraint (2.4) for each edge and face, there are $3N_E$ constraints in total because each edge corresponds to three faces. However, these constraints are not independent. For each face, the last edge that close the face can automatically satisfy the geometric constraint, as shown in Figure 2.8. For each cell, there is one additional dependency among these constraints according to the Lemma in next paragraph. So the number of independent geometric constraints is $3N_E - N_F - N_C$. Therefore, using the relations (2.7) and (2.8), a Polyhedral tessellation has

$$(3N_V + 2N_F) - (3N_E - N_F - N_C) = 3(N_F - N_V) + N_C = 4N_C \tag{2.12}$$

degrees of freedom. □

Lemma: For a polyhedral cell α (that constraints of its faces and edges are already satisfied), the geometric constraints (2.4) between neighbor faces and neighbor edges have one dependency. As shown in Figure 2.8, such constraints are in the form as $\hat{\boldsymbol{t}}_{\beta\gamma\delta} \cdot \hat{\boldsymbol{m}}_{\beta\gamma}$ where $\hat{\boldsymbol{t}}_{\beta\gamma\delta}$ is start from cell α.

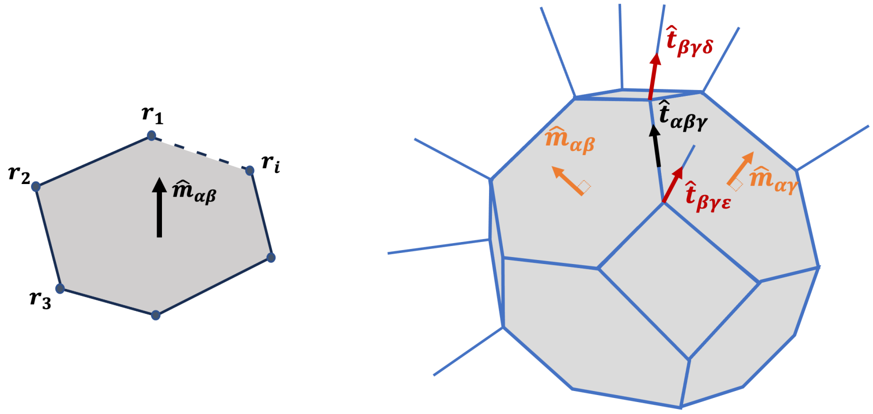
r_1
r_i
r_2
$\hat{m}_{\alpha\beta}$
r_3
$\hat{t}_{\beta\gamma\delta}$
$\hat{t}_{\alpha\beta\gamma}$
$\hat{m}_{\alpha\beta}$
$\hat{m}_{\alpha\gamma}$
$\hat{t}_{\beta\gamma\varepsilon}$

Figure 2.8. Dependency among geometric constraints in Polyhedron tessellation

Proof of Lemma: The constraints of neighbor face normal $\hat{\boldsymbol{m}}_{\beta\gamma}$ and the three neighbor edges can derive the following relation:

$$(\hat{\boldsymbol{t}}_{\beta\gamma\delta} \times \hat{\boldsymbol{t}}_{\beta\gamma\epsilon}) \cdot \hat{\boldsymbol{t}}_{\alpha\beta\gamma} = 0, \tag{2.13}$$

where $\hat{\boldsymbol{t}}_i$ denote the tangent direction of edges. Since $\hat{\boldsymbol{t}}_{\alpha\beta\gamma} = \hat{\boldsymbol{m}}_{\alpha\beta} \times \hat{\boldsymbol{m}}_{\alpha\gamma}$. Allowing us to write the relation as

$$(\hat{\boldsymbol{t}}_{\beta\gamma\delta} \times \hat{\boldsymbol{t}}_{\beta\gamma\epsilon}) \cdot (\hat{\boldsymbol{m}}_{\alpha\beta} \times \hat{\boldsymbol{m}}_{\alpha\gamma}) = 0. \tag{2.14}$$

This can be derived as the following equation:

$$(\hat{\boldsymbol{m}}_{\alpha\beta} \cdot \hat{\boldsymbol{t}}_{\beta\gamma\delta})(\hat{\boldsymbol{m}}_{\alpha\gamma} \cdot \hat{\boldsymbol{t}}_{\beta\gamma\epsilon}) = (\hat{\boldsymbol{m}}_{\alpha\beta} \cdot \hat{\boldsymbol{t}}_{\beta\gamma\epsilon})(\hat{\boldsymbol{m}}_{\alpha\gamma} \cdot \hat{\boldsymbol{t}}_{\beta\gamma\delta}). \tag{2.15}$$

If we multiply all these equations together for neighbor cell pairs $\beta\gamma$, there is

$$\prod_{\beta\gamma} \frac{\hat{\boldsymbol{m}}_{\alpha\beta} \cdot \hat{\boldsymbol{t}}_{\beta\gamma\delta}}{\hat{\boldsymbol{m}}_{\alpha\beta} \cdot \hat{\boldsymbol{t}}_{\beta\gamma\epsilon}} \frac{\hat{\boldsymbol{m}}_{\alpha\gamma} \cdot \hat{\boldsymbol{t}}_{\beta\gamma\epsilon}}{\hat{\boldsymbol{m}}_{\alpha\gamma} \cdot \hat{\boldsymbol{t}}_{\beta\gamma\delta}} = \prod_{\beta} \left(\prod_{\gamma} \frac{\hat{\boldsymbol{m}}_{\alpha\beta} \cdot \hat{\boldsymbol{t}}_{\beta\gamma\delta}}{\hat{\boldsymbol{m}}_{\alpha\beta} \cdot \hat{\boldsymbol{t}}_{\beta\gamma\epsilon}} \right) = 1 \tag{2.16}$$

The product in the brackets forms a loop, giving us

$$\prod_{\beta} (1) = 1 \tag{2.17}$$

an identity. So these equations have one degree of dependency. Therefore, for each cell, the geometric constraints (2.4) between neighbor faces and neighbor edges have one dependency. □

2.3.3. Dimensionality of Spherically-curved polyhedron tessellation

In the similar way, we can compute the degrees of freedom of a SCP tessellation, with three lemmas.

Claim: For N_C cells, the dimensionality of SCP tessellation is $5N_C$.

Proof: Consider the ordinary parameters of SCP tessellation, $\boldsymbol{r}_i$, $\boldsymbol{\rho}_{\alpha\beta}$ and $R_{\alpha\beta}$. The total degrees of them are $3N_V + 4N_F$. Then consider the geometric constraints (2.5) for each vertex and face, there are $6N_V$ constraints in total because each vertex corresponds to six spherical faces. As for the co-linear constraints (2.6) of centroids, there are $2N_E$ constraints in total, because it is three-dimensional but the ratio $\chi_{\alpha\beta\gamma}$ are free to choose. However, both kinds of constraints are not independent. According to Lemma 1, for each edge, there is one dependency between the constraints (2.5) and co-linear constraints (2.6). According to Lemma 2 and Lemma 3, there is one dependency between the ratios of co-linearity $\chi_{\alpha\beta\gamma}$ at each vertex and on additional dependency for each cell. Thus there are $N_E + N_V + N_C$ dependency among $6N_V + 2N_E$ total geometric constraints. So the number of independent geometric constraints is $5N_V + N_E - N_C$. Therefore, a SCP tessellation has

$$(3N_V + 4N_F) - (5N_V + N_E - N_C) = 4N_F - 4N_V + N_C = 5N_C \tag{2.18}$$

degrees of freedom. □

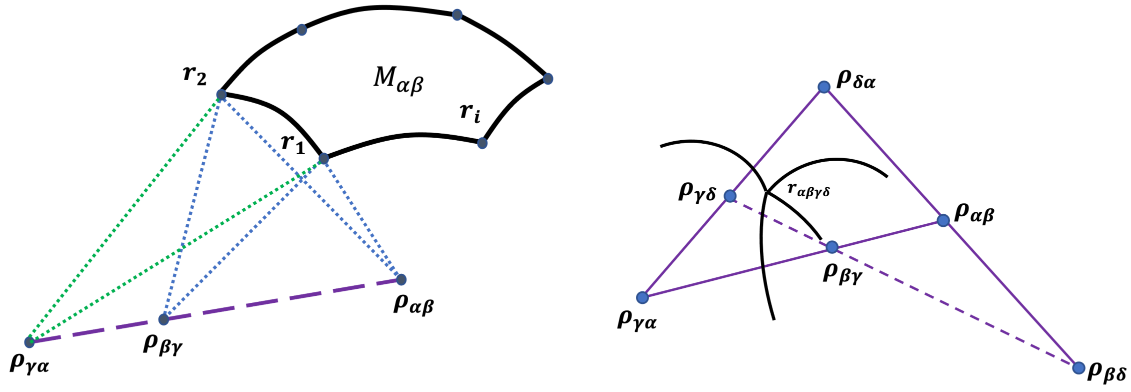
$\boldsymbol{r_2}$
$M_{\alpha\beta}$
$\boldsymbol{r_i}$
$\boldsymbol{r_1}$
$\boldsymbol{\rho_{\alpha\beta}}$
$\boldsymbol{\rho_{\beta\gamma}}$
$\boldsymbol{\rho_{\gamma\alpha}}$
$\boldsymbol{\rho_{\delta\alpha}}$
$\boldsymbol{\rho_{\gamma\delta}}$
$\boldsymbol{r_{\alpha\beta\gamma\delta}}$
$\boldsymbol{\rho_{\alpha\beta}}$
$\boldsymbol{\rho_{\beta\gamma}}$
$\boldsymbol{\rho_{\gamma\alpha}}$
$\boldsymbol{\rho_{\beta\delta}}$

Figure 2.9. Dependency among geometric constraints in SCP tessellation

Lemma 1: For an edge $E_{\alpha\beta\gamma}$, the two ends of it are vertices $\boldsymbol{r}_1$ and $\boldsymbol{r}_2$, as shown in the left panel of Figure 2.9. When $|\boldsymbol{r}_1 - \boldsymbol{\rho}_{\alpha\beta}| = |\boldsymbol{r}_2 - \boldsymbol{\rho}_{\alpha\beta}|$ and $|\boldsymbol{r}_1 - \boldsymbol{\rho}_{\beta\gamma}| = |\boldsymbol{r}_2 - \boldsymbol{\rho}_{\beta\gamma}|$ are satisfied, $|\boldsymbol{r}_1 - \boldsymbol{\rho}_{\gamma\alpha}| = |\boldsymbol{r}_2 - \boldsymbol{\rho}_{\gamma\alpha}|$ is satisfied automatically if $\boldsymbol{\rho}_{\alpha\beta}$, $\boldsymbol{\rho}_{\beta\gamma}$ and $\boldsymbol{\rho}_{\gamma\alpha}$ are co-linear. □

Lemma 2: At each vertex $\boldsymbol{r}_{\alpha\beta\gamma\delta}$, the centroids of six corresponding faces are coplanar if they satisfy the co-linear constraints, as shown in the right panel of Figure 2.9.

Suppose the first three co-linear constraints, corresponding to $\chi_{\beta\gamma\alpha}$, $\chi_{\gamma\delta\alpha}$ and $\chi_{\delta\beta\alpha}$, are satisfied. These three axes determine a plane, so $\boldsymbol{\rho}_{\beta\gamma}$, $\boldsymbol{\rho}_{\gamma\delta}$ and $\boldsymbol{\rho}_{\delta\beta}$ can only move in plane. This suggests that there ought to be one constraint instead of two for the last co-linear constraint. The last constraint can be given by

$$\chi_{\beta\gamma\alpha}\chi_{\gamma\delta\alpha}\chi_{\delta\beta\alpha} = 1, \tag{2.19}$$

according to Menelaus' theorem. □

Lemma 3: For each cell, if we construct a product of all the Menelaus equations of its vertices,

$$\prod_{\boldsymbol{r}_{\alpha\beta\gamma\delta}\in\alpha} \chi_{\beta\gamma\alpha}\chi_{\gamma\delta\alpha}\chi_{\delta\beta\alpha} = \prod_{\boldsymbol{e}_{\alpha\beta\gamma}\in\alpha} \chi_{\beta\gamma\alpha}\chi_{\gamma\beta\alpha} = 1, \tag{2.20}$$

it gives us an identity. That is because $\chi_{\beta\gamma\alpha}\chi_{\gamma\beta\alpha} = 1$, and thus all left-hand-side terms cancel each other. □

2.3.4. Generalized weighted Voronoi diagram

A Voronoi tessellation of N_C cells in three-dimensional space is defined by C sites: $\{\boldsymbol{q}_\alpha\}_{\alpha=1,2,\ldots,N_C}$. A cell region C_α is a set of points which are closer to $\boldsymbol{q}_\alpha$ than to other sites: $C_\alpha = \{\boldsymbol{r} | d_\alpha(\boldsymbol{r}) < d_i(\boldsymbol{r}), \forall i \neq \alpha\}$, and here $d_\alpha(\boldsymbol{r}) = |\boldsymbol{r} - \boldsymbol{q}_\alpha|$ is the Euclidean distance. So the boundary $M_{\alpha\beta}$ between any two neighboring cells is the perpendicular bisector of two corresponding sites, $M_{\alpha\beta} = \{\boldsymbol{r} | d_\alpha(\boldsymbol{r}) = d_\beta(\boldsymbol{r})\}$, which is a flat plane. So the shape of a cell is a polyhedron. Therefore, Voronoi tessellation is a subspace of the Polyhedral tessellation space, whose dimensionality is $3N_C$. The left panel of Figure 2.10 shows the two-dimensional case of Voronoi tessellation.

Now, we can modify the definition of distance by subtracting (or adding) a parameter θ_α^2 to the squared Euclidean distance, $d_\alpha^2(\boldsymbol{r}) = |\boldsymbol{r} - \boldsymbol{q}_\alpha|^2 - \theta_\alpha^2$. A cell region C_α is defined in the same way: $C_\alpha = \{\boldsymbol{r} | d_\alpha(\boldsymbol{r}) < d_i(\boldsymbol{r}), \forall i \neq \alpha\}$. We call this kind of tessellation as Weighted Voronoi tessellation, where θ_α is the weight for each cell α. As we proved below, cell shapes in Weighted Voronoi tessellation are polyhedrons. Since the dimensionality of Weighted Voronoi tessellation space is $4N_C$, it is equivalent to the space of Polyhedral tessellation. Therefore, we can use the independent parameters $\{\boldsymbol{q}_\alpha, \theta_\alpha\}_{\alpha=1,2,\ldots,N_C}$ to parameterize Polyhedral tessellation. The middle panel of Figure 2.10 shows the two-dimensional case of Weighted Voronoi tessellation.

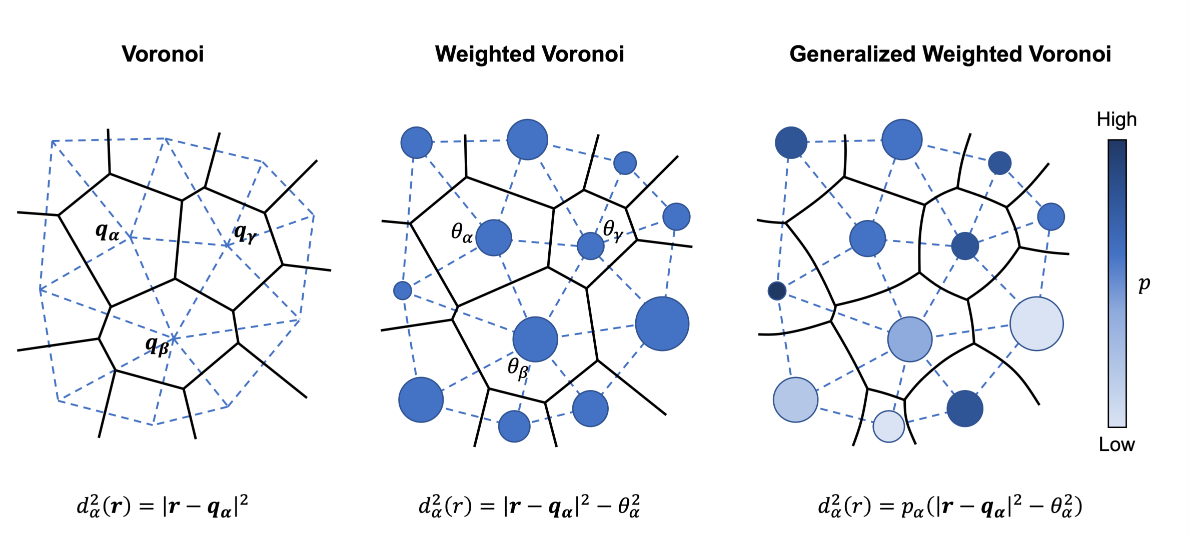
Voronoi
Weighted Voronoi
Generalized Weighted Voronoi
q_α
q_γ
q_β
θ_α
θ_γ
θ_β
High
p
Low
$d_\alpha^2(\boldsymbol{r}) = |\boldsymbol{r} - \boldsymbol{q}_\alpha|^2$
$d_\alpha^2(r) = |\boldsymbol{r} - \boldsymbol{q}_\alpha|^2 - \theta_\alpha^2$
$d_\alpha^2(r) = p_\alpha(|\boldsymbol{r} - \boldsymbol{q}_\alpha|^2 - \theta_\alpha^2)$

Figure 2.10. Generalized Weighted Voronoi tessellation in 2d

Claim: Cell shapes in Weighted Voronoi tessellation are polyhedrons.

Proof: For any two points $\boldsymbol{r}_1$ and $\boldsymbol{r}_2$ at the two-cell boundary $M_{\alpha\beta}$ satisfy

$$|\boldsymbol{r}_1 - \boldsymbol{q}_\alpha|^2 - |\boldsymbol{r}_1 - \boldsymbol{q}_\beta|^2 = \theta_\alpha^2 - \theta_\beta^2 = |\boldsymbol{r}_2 - \boldsymbol{q}_\alpha|^2 - |\boldsymbol{r}_2 - \boldsymbol{q}_\beta|^2. \tag{2.21}$$

Algebraic simplification yields

$$(\boldsymbol{r}_1 - \boldsymbol{r}_2) \cdot (\boldsymbol{q}_\alpha - \boldsymbol{q}_\beta) = 0. \tag{2.22}$$

Thus $\boldsymbol{r}_1 - \boldsymbol{r}_2$ is perpendicular to $\boldsymbol{q}_\alpha - \boldsymbol{q}_\beta$. Since the two points are randomly chosen on the boundary, we can derive that the boundary face is an orthogonal plane to the line $q_{\alpha\beta}$. Therefore, the shape of cells are polyhedral. □

Now, we can further modify the definition of distance by a multiplicative factor p_α to obtain $d_\alpha^2(\boldsymbol{r}) = p_\alpha(|\boldsymbol{r} - \boldsymbol{q}_\alpha|^2 - \theta_\alpha^2)$ and construct the tessellation in the same way. We call such tessellation as Generalized Weighted Voronoi (GWV) tessellation, and we call p_α as the power of cell α. The dimensionality of GWV tessellation space is $5N_C$, determined by independent parameters $\Psi = \{\boldsymbol{q}_\alpha, \theta_\alpha, p_\alpha\}_{\alpha=1,2,\ldots,N_C}$. As proved below, the shapes of cell boundaries are spherical, thus a GWV tessellation is a SCP tessellation. Since the dimensionalities of GWV and SCP are equal, there exists a one-on-one map between the two space. Therefore, SCP tessellation can be parameterized by Ψ. The right panel of Figure 2.10 shows the two-dimensional case of GWV tessellation.

Claim: The shape of any two-cell boundary is spherical.

Proof: Any point $\boldsymbol{r}$ at boundary $M_{\alpha\beta}$ satisfies $p_\alpha(|\boldsymbol{r} - \boldsymbol{q}_\alpha|^2 - \theta_\alpha^2) = p_\beta(|\boldsymbol{r} - \boldsymbol{q}_\beta|^2 - \theta_\beta^2)$. Multiplying this equation by $(p_\alpha - p_\beta)$ and simplifying yields

$$\begin{aligned} &p_\alpha^2(\boldsymbol{r} - \boldsymbol{q}_\alpha)^2 + p_\beta^2(\boldsymbol{r} - \boldsymbol{q}_\beta)^2 - 2p_\alpha p_\beta(\boldsymbol{r} - \boldsymbol{q}_\alpha) \cdot (\boldsymbol{r} - \boldsymbol{q}_\beta) \\ &\qquad = p_\alpha p_\beta(\boldsymbol{q}_\alpha - \boldsymbol{q}_\beta)^2 + (p_\alpha - p_\beta)(p_\alpha\theta_\alpha^2 - p_\beta\theta_\beta^2). \end{aligned} \tag{2.23}$$

The left hand side of the above equations is a square, while the right hand side is a constant independent of $\boldsymbol{r}$. So this equation can be further simplified as

$$(p_\alpha - p_\beta)^2(\boldsymbol{r} - \frac{p_\alpha \boldsymbol{q}_\alpha - p_\beta \boldsymbol{q}_\beta}{p_\alpha - p_\beta})^2 = const. \tag{2.24}$$

Defining

$$\boldsymbol{\rho}_{\alpha\beta} = \frac{p_\alpha \boldsymbol{q}_\alpha - p_\beta \boldsymbol{q}_\beta}{p_\alpha - p_\beta} \tag{2.25}$$

and

$$R^2_{\alpha\beta} = \frac{p_\alpha p_\beta (\boldsymbol{q}_\alpha - \boldsymbol{q}_\beta)^2 + (p_\alpha - p_\beta)(p_\alpha \theta^2_\alpha - p_\beta \theta^2_\beta)}{(p_\alpha - p_\beta)^2}. \tag{2.26}$$

the equation for $\boldsymbol{r}$ becomes $|\boldsymbol{r} - \boldsymbol{\rho}_{\alpha\beta}|^2 = R_{\alpha\beta}$, which describes a sphere with centroid $\boldsymbol{\rho}_{\alpha\beta}$ and radius $R_{\alpha\beta}$. So the shape of the boundary $M_{\alpha\beta}$ is a spherical section. □

In summary, consider the intrinsic geometric constraints in Polyhedron tessellation or SCP tessellation, the two types of tessellation have $4N_C$ and $5N_C$ degrees of freedom, respectively. Polyhedron tessellations can be constructed by independent parameters of Weighted Voronoi tessellation, and SCP tessellations can be constructed by independent parameters of GWV tessellation.

2.4. Analytical solutions of mechanics

We are now parameterize the permissible geometry in equilibrium by Generalized Weighted Voronoi tessellation. The inverse problem is to infer the values of mechanical inputs from the given geometry parameters. Instead of solving the linear equations (2.1)-(2.3) directly, we introduce an inference method by constructing the mechanical dual graph to get the analytical solution of mechanics in this section.

In order to understand the ideas of the inverse method, we first introduce the dual graph in two-dimensional analogue (2.4.1). Then we generalized the idea to three dimensional scenario (2.4.2). By this method, we solve out the analytical solutions of the force balance equations. However, the solutions are not unique. There exist three mechanical zero modes that can produce the same geometry (2.4.3).

2.4.1. Two-dimensional mechanical dual graph

For the two-dimensional analogue of inverse problem, this inference method was first raised by Noll et al. [**28, 29**]. But here we state it in a different logic. This logic is based on a mathematical fact of closed shapes, which can be derived from divergence theorem in calculus.

Claim: For any closed three-dimensional shape V, the integral of the vector area $\hat{\boldsymbol{n}}dS$ over the closed shape surface ∂V is zero:

$$\oint_{\partial V} \hat{\boldsymbol{n}} dS = \boldsymbol{0}. \tag{2.27}$$

Proof: According to the three-dimensional divergence theorem, for any vector of matrix field $\boldsymbol{F}$, there is $\oint_{\partial V}(\boldsymbol{F}\cdot\hat{\boldsymbol{n}})dS = \int_V(\nabla\cdot\boldsymbol{F})dV$. Taking $\boldsymbol{F}$ as the identical matrix $\boldsymbol{I}$,

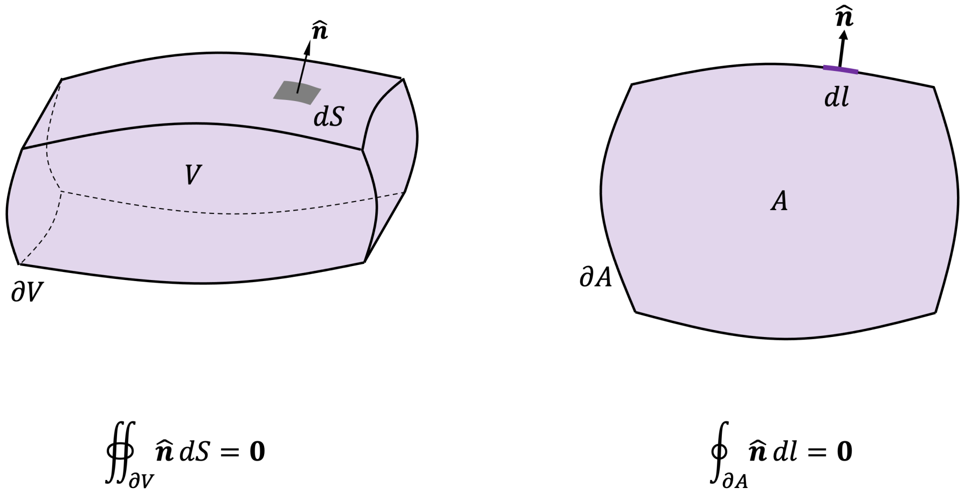
$\hat{\boldsymbol{n}}$
dS
V
∂V
$\oiint_{\partial V} \hat{\boldsymbol{n}}\, dS = \mathbf{0}$
$\hat{\boldsymbol{n}}$
dl
A
∂A
$\oint_{\partial A} \hat{\boldsymbol{n}}\, dl = \mathbf{0}$

Figure 2.11. Divergence theorem in 3d and 2d

we will get $\oint_{\partial V} \hat{\boldsymbol{n}} dS = \int_V (\nabla \cdot \boldsymbol{I}) dV$. Since $\nabla \cdot \boldsymbol{I} = \mathbf{0}$, the right-hand-side of the equation is zero. □

Corollary: For any closed two-dimensional shape A, the integral of the edge normal vector $\hat{\boldsymbol{n}} dl$ over the closed shape boundary ∂A is zero:

$$\oint_{\partial A} \hat{\boldsymbol{n}} dl = \mathbf{0}. \square \tag{2.28}$$

According to Noll [**28**], the polygon tessellation of cells under tension balance is Weighted Voronoi tessellation. For any membrane $M_{\alpha\beta}$, the line connecting two corresponding Voronoi sites $\boldsymbol{q}_\alpha$ and $\boldsymbol{q}_\beta$ is perpendicular to the membrane. Therefore, we call the triangular lattice formed by Voronoi sites is 'dual' to the polygon tessellation. As shown in Figure 2.12, consider the dual triangle of the vertex $\boldsymbol{r}_{\alpha\beta\gamma}$ and apply the

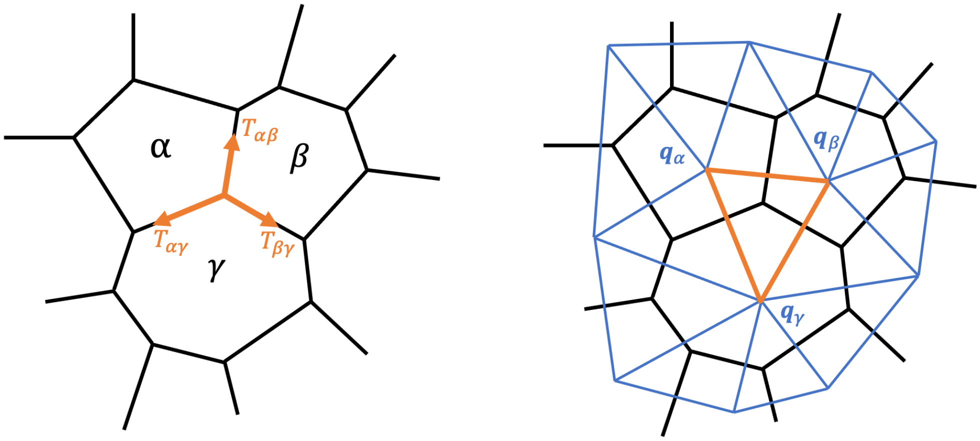

Figure 2.12. Mechanical duality in polygonal tessellation

divergence theorem, we have

$$q_{\alpha\beta}\hat{\boldsymbol{t}}_1 + q_{\beta\gamma}\hat{\boldsymbol{t}}_2 + q_{\gamma\alpha}\hat{\boldsymbol{t}}_3 = \mathbf{0}. \tag{2.29}$$

Here, $\hat{\boldsymbol{t}}_i$s are the tangent direction of edges, and equivalently they are normal directions of dual lines. This equation have the same form and coefficients - the $\hat{\boldsymbol{t}}_i$s - as the tension balance equation:

$$T_{\alpha\beta}\hat{\boldsymbol{t}}_1 + T_{\beta\gamma}\hat{\boldsymbol{t}}_2 + T_{\gamma\alpha}\hat{\boldsymbol{t}}_3 = \mathbf{0}. \tag{2.30}$$

Therefore, the value of membrane tension is proportional to the dual lattice length. Thus we get the analytical solution of tensions:

$$T_{\alpha\beta} = b * q_{\alpha\beta}. \tag{2.31}$$

Here the undefined constant b represents the scale of tensions, and it will not affect the tension balance.

Now let us consider the Circular Arc Polygon (CAP) tessellation of cells under tension balance and pressure difference. According to Noll [**29**], the geometry under equilibrium can be parameterized by two-dimensional Generalized Weighted Voronoi tessellation. However, in this case, the lattice formed by Voronoi sites are not perpendicular to the membranes since they are curved. So we construct the dual graph in another way. Consider any point $\boldsymbol{r}$ on membrane $M_{\alpha\beta}$, the two corresponding dual points are defined as:

$$\boldsymbol{q}_\alpha^*(\boldsymbol{r}) = \boldsymbol{r} + p_\alpha(\boldsymbol{q}_\alpha - \boldsymbol{r}), \tag{2.32}$$

and the same form for $\boldsymbol{q}_\beta^*(\boldsymbol{r})$.

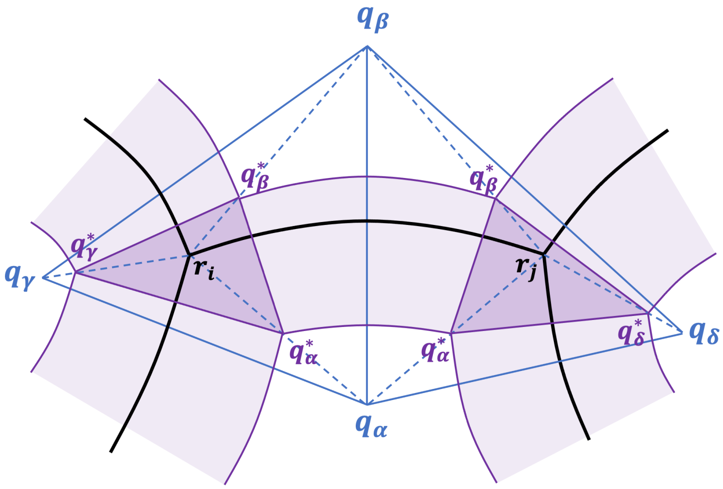

Figure 2.13. Dual graph construction in CAP tessellation

Claim: The dual line $q^*_{\alpha\beta}(\boldsymbol{r})$ with respect to the point $\boldsymbol{r}$ at membrane $M_{\alpha\beta}$ is perpendicular to the membrane at $\boldsymbol{r}$, and the length is a constant along the membrane.

Proof: The center of the membrane circular arc is $\boldsymbol{\rho}_{\alpha\beta} = (p_\alpha \boldsymbol{q}_\alpha - p_\beta \boldsymbol{q}_\beta)/(p_\alpha - p_\beta)$. Consider the vector $\boldsymbol{q}^*_\alpha - \boldsymbol{q}^*_\beta = p_\alpha(\boldsymbol{q}_\alpha - \boldsymbol{r}) - p_\beta(\boldsymbol{q}_\beta - \boldsymbol{r}) = (p_\alpha - p_\beta)(\boldsymbol{\rho}_{\alpha\beta} - \boldsymbol{r})$, it is parallel to $\boldsymbol{r} - \boldsymbol{\rho}_\alpha$. This parallel is equivalent to the perpendicularity between dual line and membrane. On the other hand, from the equation we have $q^*_{\alpha\beta} = |p_\alpha - p_\beta| R_{\alpha\beta}$. So the length of dual line is a constant along the membrane. $\square$

Therefore, the dual graph is as shown in Figure 2.13: At a vertex, three dual lines which are perpendicular to the three membrane tangents form a dual triangle; along a membrane, the dual line swipe a curved quadrilateral shape. Similar as the tension-only case, applying divergence theorem to the dual triangle, we have

$$q^*_{\alpha\beta}\hat{\boldsymbol{t}}_1 + q^*_{\beta\gamma}\hat{\boldsymbol{t}}_2 + q^*_{\gamma\alpha}\hat{\boldsymbol{t}}_3 = \boldsymbol{0}, \tag{2.33}$$

which corresponds to the tension balance equation. Thus we have the solution of tensions:

$$T_{\alpha\beta} = b * q^*_{\alpha\beta}. \tag{2.34}$$

As for membranes, we apply the divergence theorem on the dual quadrilateral corresponding to a membrane element dr and get:

$$dq^*_\alpha \hat{\boldsymbol{n}}_1 + dq^*_\beta \hat{\boldsymbol{n}}_2 + q^*_{\alpha\beta}\hat{\boldsymbol{t}}_1 + q^*_{\alpha\beta}\hat{\boldsymbol{t}}_2 = \boldsymbol{0}. \tag{2.35}$$

Here, dq^*_α and dq^*_β are the length which is swiped by $\boldsymbol{r}$ along dr; $\hat{\boldsymbol{t}}_1$ and $\hat{\boldsymbol{t}}_2$ are tangent directions of the edge; $\hat{\boldsymbol{n}}_1$ and $\hat{\boldsymbol{n}}_2$ are normal directions of the edge. This has the same

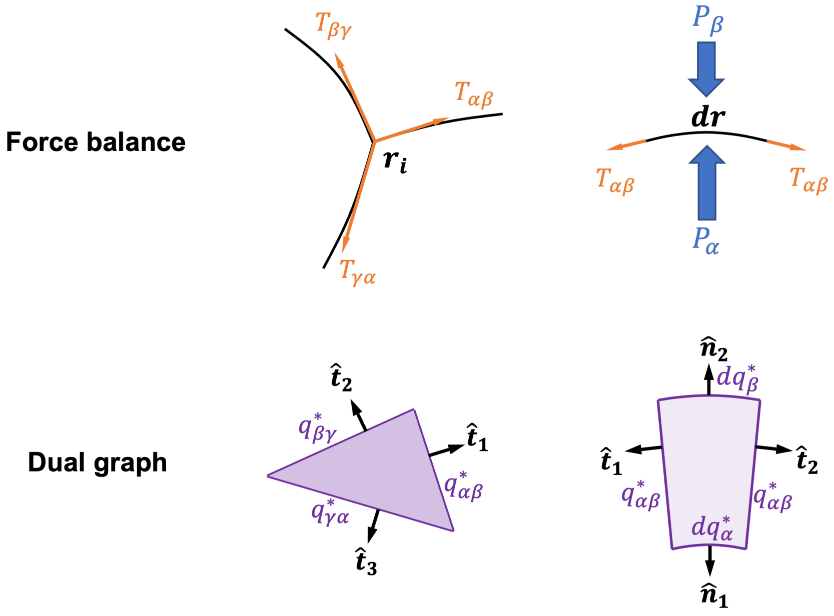
Force balance
$T_{\beta\gamma}$
$T_{\alpha\beta}$
$\boldsymbol{r_i}$
$T_{\gamma\alpha}$
P_β
$\boldsymbol{dr}$
$T_{\alpha\beta}$
$T_{\alpha\beta}$
P_α
Dual graph
$\hat{\boldsymbol{t}}_2$
$q^*_{\beta\gamma}$
$\hat{\boldsymbol{t}}_1$
$q^*_{\alpha\beta}$
$q^*_{\gamma\alpha}$
$\hat{\boldsymbol{t}}_3$
$\hat{\boldsymbol{n}}_2$
dq^*_β
$\hat{\boldsymbol{t}}_1$
$\hat{\boldsymbol{t}}_2$
$q^*_{\alpha\beta}$
$q^*_{\alpha\beta}$
dq^*_α
$\hat{\boldsymbol{n}}_1$

Figure 2.14. Mechanical duality in CAP tessellation

form and coefficients as the elemental pressure tension balance equation:

$$-P_\alpha dr\hat{\boldsymbol{n}}_1 - P_\beta dr\hat{\boldsymbol{n}}_2 + T_{\alpha\beta}\hat{\boldsymbol{t}}_1 + T_{\alpha\beta}\hat{\boldsymbol{t}}_2 = \mathbf{0}. \tag{2.36}$$

Therefore, the solution of pressure is

$$P_\alpha = -b\frac{dq^*_\alpha}{dr} = b(p_\alpha - 1). \tag{2.37}$$

However, we notice that the dual graph is not the unique choice. If we set the rescaled dual points of $\boldsymbol{r}$ as $\boldsymbol{q}^{**}_\alpha(r) = \boldsymbol{r} + \lambda p_\alpha(\boldsymbol{q}_\alpha - \boldsymbol{r})$, by the free parameter λ, then the dual graph is as shown in the right panel of Figure 2.15. Comparing to the previous dual graph, the edge lengths of the quadrilateral have changed. Thus the solution of tensions and pressures are

$$
\begin{aligned}
T_{\alpha\beta} &= bq^{**}_{\alpha\beta} = b\lambda q^{*}_{\alpha\beta}, \\
P_{\alpha} &= b(\lambda p_{\alpha} - 1) = b\lambda p_{\alpha} - b.
\end{aligned}
\tag{2.38}
$$

Reset the constants (b, λ), we have the general form of analytical solution of mechanics:

$$
\begin{aligned}
T_{\alpha\beta} &= b * q^{*}_{\alpha\beta} \\
P_{\alpha} &= a + b * p_{\alpha}.
\end{aligned}
\tag{2.39}
$$

The undefined constants (a, b) can be set as any value and will not affect the equilibrium. The physical meaning of a is the background pressure and of b is the mechanical scale.

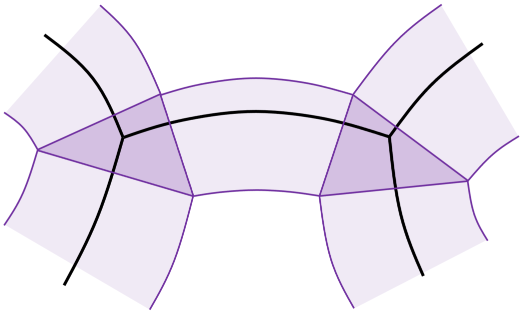

Figure 2.15. Rescaled dual graph construction

Consequently, by constructing the dual graph using the Voronoi parameters, we get the analytical solutions of mechanics with undefined constants. And more importantly, the dual graph present a way to visualize how mechanical inputs are balanced in the two-dimensional multi-cellular system.

2.4.2. Three-dimensional mechanical dual graph

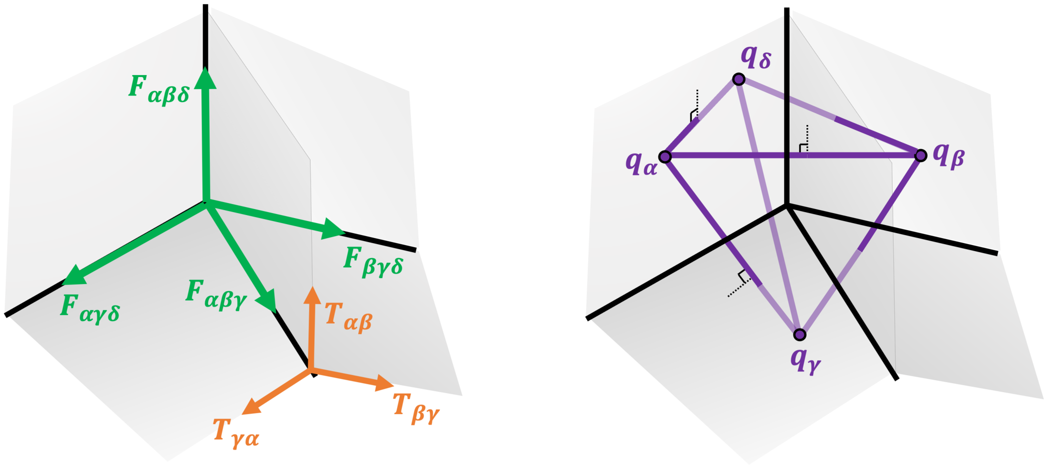
$F_{\alpha\beta\delta}$
$F_{\beta\gamma\delta}$
$F_{\alpha\beta\gamma}$
$F_{\alpha\gamma\delta}$
$T_{\alpha\beta}$
$T_{\beta\gamma}$
$T_{\gamma\alpha}$
q_δ
q_α
q_β
q_γ

Figure 2.16. Mechanical duality in Polyhedral tessellation

In three-dimensional case, we can construct the dual graph in the similar way. For the polyhedral tessellation, the dual lattice is formed by directly connect the Voronoi sites. For any membrane face $M_{\alpha\beta}$, the corresponding dual line $q_{\alpha\beta}$ is perpendicular to the face. Thus at an edge $E_{\alpha\beta\gamma}$, the three dual lines form a dual triangle, which is orthogonal to the edge. Equivalently, the tangent direction of the junctional edge $\hat{\boldsymbol{t}}_1$ is the normal direction of the dual triangle. As shown in Figure 2.16, applying the two-dimensional divergence theorem to this triangle, we get the equation $q_{\alpha\beta}\hat{\boldsymbol{n}}_1 + q_{\beta\gamma}\hat{\boldsymbol{n}}_2 + q_{\gamma\alpha}\hat{\boldsymbol{n}}_3 = \mathbf{0}$. Comparing to the surface tension balance equation $T_{\alpha\beta}\hat{\boldsymbol{n}}_1 + T_{\beta\gamma}\hat{\boldsymbol{n}}_2 + T_{\gamma\alpha}\hat{\boldsymbol{n}}_3 = \mathbf{0}$., the values of membrane surface tensions are proportional to the length of dual lines:

$$T_{\alpha\beta} = b * q_{\alpha\beta}. \tag{2.40}$$

Here b is an undefined global constant, representing the scale of surface tensions. For a vertex $\boldsymbol{r}_{\alpha\beta\gamma\delta}$, the four dual triangles form a dual tetrahedron. Applying the three-dimensional divergence theorem to the dual tetrahedron, we get

$$S_{\alpha\beta\gamma}\hat{\boldsymbol{t}}_1 + S_{\alpha\beta\delta}\hat{\boldsymbol{t}}_2 + S_{\alpha\gamma\delta}\hat{\boldsymbol{t}}_3 + S_{\beta\gamma\delta}\hat{\boldsymbol{t}}_4 = \mathbf{0}. \tag{2.41}$$

Here the $\hat{\boldsymbol{t}}_i$ and S_i are normal directions and areas of dual triangle.This equation have the same form and coefficients - the $\hat{\boldsymbol{t}}_i$s - as line tension balance equation 2.3. Therefore, the values of line tensions are proportional to the corresponding dual triangle ares:

$$F_{\alpha\beta\gamma} = c * S_{\alpha\beta\gamma}. \tag{2.42}$$

Here c is another global constant that represents the scale of line tensions. In summary, (2.40) and (2.42) provide the analytical solutions of membrane and surface tensions given by Voronoi parameters. We notice that line tension balance and surface tension balance are decoupled with each other, thus the two scales (b, c) are decoupled in the solution.

Now, let us consider the SCP tessellation and construct its dual graph. As in two-dimensional analogue, for any point $\boldsymbol{r}$ at a membrane $M_{\alpha\beta}$, the two corresponding dual points $\boldsymbol{q}^*_\alpha$ and $\boldsymbol{q}^*_\beta$ are given by equation (2.32). We have the same claim that the line $q^*_{\alpha\beta}$ is perpendicular to the membrane face at $\boldsymbol{r}$ and the line is a constant along it, by the same proof. Further more, for a junctional edge $E_{\alpha\beta\gamma}$, the three dual lines form a

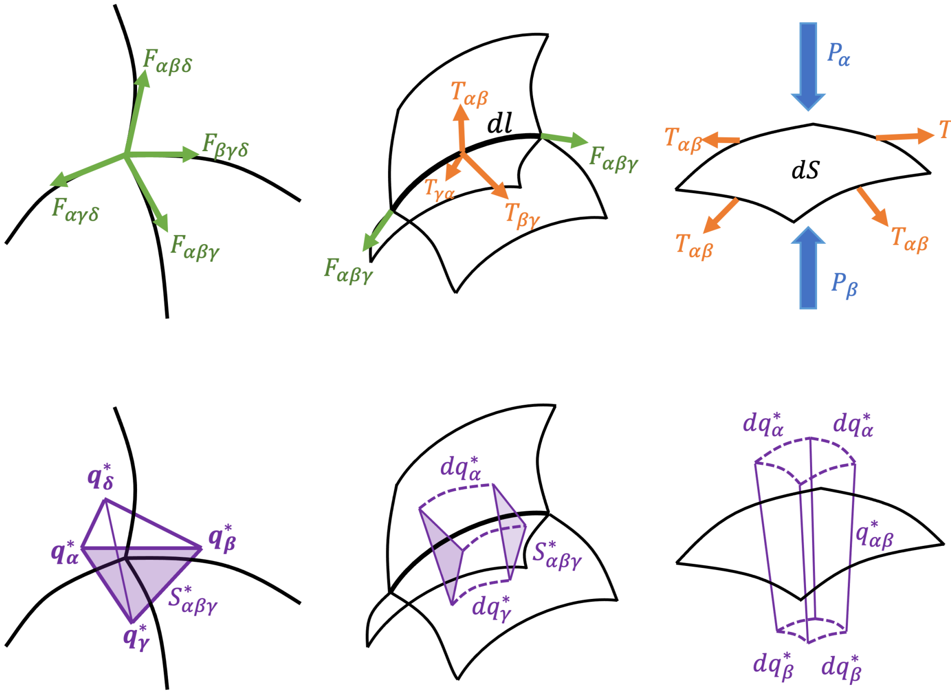
$F_{\alpha\beta\delta}$
$F_{\beta\gamma\delta}$
$F_{\alpha\gamma\delta}$
$F_{\alpha\beta\gamma}$
$T_{\alpha\beta}$
dl
$F_{\alpha\beta\gamma}$
$T_{\gamma\alpha}$
$T_{\beta\gamma}$
$F_{\alpha\beta\gamma}$
P_α
$T_{\alpha\beta}$
$T_{\alpha\beta}$
dS
$T_{\alpha\beta}$
$T_{\alpha\beta}$
P_β
q^*_δ
q^*_α
q^*_β
$S^*_{\alpha\beta\gamma}$
q^*_γ
dq^*_α
$S^*_{\alpha\beta\gamma}$
dq^*_γ
dq^*_α
dq^*_α
$q^*_{\alpha\beta}$
dq^*_β
dq^*_β

Figure 2.17. Mechanical duality in SCP tessellation

dual triangle of area $S^*_{\alpha\beta\gamma}$. Following the claim before, it is trivial to have the corollary that the dual triangle is orthogonal to the junctional edge at $\boldsymbol{r}$ and the area is constant along the junctional edge. The dual triangle swipe along the junctional edge forming a triangular tube, and four of them meet at a vertex forming a tetrahedron. Applying the three-dimensional divergence theorem to the tetrahedron, we get a similar equation as (2.41):

$$S^*_{\alpha\beta\gamma}\hat{\boldsymbol{t}}_1 + S^*_{\alpha\beta\delta}\hat{\boldsymbol{t}}_2 + S^*_{\alpha\gamma\delta}\hat{\boldsymbol{t}}_3 + S^*_{\beta\gamma\delta}\hat{\boldsymbol{t}}_4 = \mathbf{0}. \tag{2.43}$$

Comparing to the line tension balance equation (2.3), the solution of line tensions in this case is:

$$F_{\alpha\beta\gamma} = c * S^*_{\alpha\beta\gamma}. \tag{2.44}$$

On the other hand, consider the force balance at a junctional edge element dr, as shown in the middle column of Figure 2.17, there is

$$F_{\alpha\beta\gamma}\hat{\boldsymbol{t}}_1 + F_{\alpha\beta\gamma}\hat{\boldsymbol{t}}_2 + T_{\alpha\beta}dr\hat{\boldsymbol{n}}_1 + T_{\beta\gamma}dr\hat{\boldsymbol{n}}_2 + T_{\gamma\alpha}dr\hat{\boldsymbol{n}}_3 = \mathbf{0}. \tag{2.45}$$

Here $\hat{\boldsymbol{t}}_1$ and $\hat{\boldsymbol{t}}_2$ are tangent directions of the edge at two ends. Applying the divergence theorem to the corresponding elemental triangular tube, we have an equation with the same form:

$$S^*_{\alpha\beta\gamma}\hat{\boldsymbol{t}}_1 + S^*_{\alpha\beta\gamma}\hat{\boldsymbol{t}}_2 + q^*_{\alpha\beta}\frac{dq^*_\alpha + dq^*_\beta}{2}\hat{\boldsymbol{n}}_1 + q^*_{\beta\gamma}\frac{dq^*_\beta + dq^*_\gamma}{2}\hat{\boldsymbol{n}}_2 + q^*_{\gamma\alpha}\frac{dq^*_\gamma + dq^*_\alpha}{2}\hat{\boldsymbol{n}}_3 = \mathbf{0}. \tag{2.46}$$

Note that the lateral faces of the triangle tube are trapezoids because of the curved edge. Comparing to (2.45), we have the expression of surface tension:

$$T_{\alpha\beta} = \frac{c}{2}q^*_{\alpha\beta}(\frac{dq^*_\alpha}{dr} + \frac{dq^*_\beta}{dr}) = \frac{c}{2}q^*_{\alpha\beta}(2 - p_\alpha - p_\beta). \tag{2.47}$$

Additionally, on a membrane face element $dr_1 \times dr_1$ as shown in the right column of Figure 2.17, the elemental version of Young-Laplace equation (2.1) is given by:

$$T_{\alpha\beta}dr_1\hat{\boldsymbol{n}}_1 + T_{\alpha\beta}dr_1\hat{\boldsymbol{n}}_2 + T_{\alpha\beta}dr_1\hat{\boldsymbol{n}}_3 + T_{\alpha\beta}dr_1\hat{\boldsymbol{n}}_4 - P_\alpha dr_1^2\hat{\boldsymbol{m}}_1 - P_\beta dr_1^2\hat{\boldsymbol{m}}_2 = \mathbf{0}. \tag{2.48}$$

As shown in the bottom right panel of Figure 2.17, the dual line $q^*_{\alpha\beta}$ swipe a shell with a certain thickness along the membrane. Applying divergence theorem on the shell element, we have

$$\frac{1}{2}q^*_{\alpha\beta}(dq^*_\alpha + dq^*_\beta)(\hat{\boldsymbol{n}}_1 + \hat{\boldsymbol{n}}_2 + \hat{\boldsymbol{n}}_3 + \hat{\boldsymbol{n}}_4) + dq^*_\alpha dq^*_\alpha \hat{\boldsymbol{m}}_1 + dq^*_\beta dq^*_\beta \hat{\boldsymbol{m}}_2 = \boldsymbol{0}. \tag{2.49}$$

Comparing these two equations and applying (2.47), we could solve for the magnitude of pressures:

$$P_\alpha = -c(p_\alpha - 1)^2. \tag{2.50}$$

Using the similar trick as in two-dimension to rescale the dual graph, we can derive the general form of analytical solutions of mechanics:

$$\begin{aligned} F_{\alpha\beta\gamma} &= cS^*_{\alpha\beta\gamma}, \\ T_{\alpha\beta} &= \frac{1}{2}(b - c(p_\alpha + p_\beta))q^*_{\alpha\beta}, \\ P_\alpha &= a + bp_\alpha - cp^2_\alpha. \end{aligned} \tag{2.51}$$

In the equation, the global constants (a, b, c) are undefined free parameters that have no effect to the force balance of the system.

Here, we emphasize that the mechanical solution (2.51) is the central theoretical result of our study. This result provides the inverse mapping from the geometry space to the mechanical space analytically.

2.4.3. Mechanical zero-modes

In the construction of dual graphs of three-dimensional SCP tessellation, we find out the answer to the inverse problem of force inference. The analytical solutions (2.51) assure the existence of the solutions of mechanical balance equations. However, the undefined constants (a, b, c) imply that the mechanical solution for a given SCP geometry is not unique. In another word, there exists three zero modes of mechanical inputs that can form the same three-dimensional geometry of cellular aggregate.

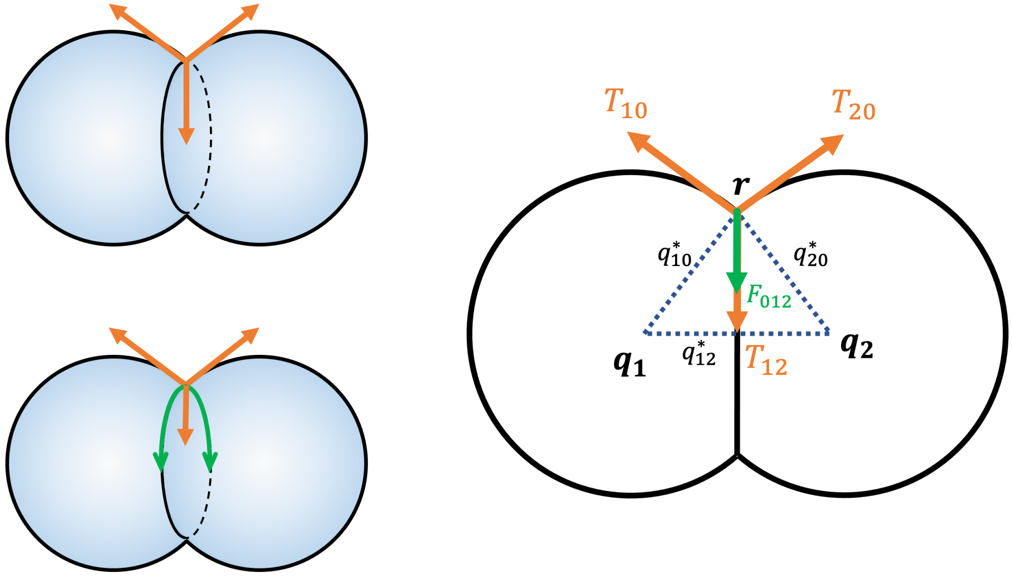

Figure 2.18. Two-cell example of mechanical zero-modes

What are the physical meanings of these zero modes? As in two-dimensional scenario, the constant a only appears in the pressure solution, which represents the background pressure of cells. By changing the value of a, the mechanical zero mode is that the absolute value of pressures are changing, but the pressure differences are not affected, thus the Young-Laplace equation will remain. It will not lose generality by setting $a = 0$. In order to understand the physical meanings of b and c, let us consider a scenario that there is no line tension in this system, which means $c = 0$. In this non-line-tension scenario, the three surface tensions are balanced at any junctional edge, and the constant b is the multiplier in the pressure and surface tension solutions. Thus the constant b can be treated as the scale of surface tensions and pressures, which is the same case as in two-dimensional CAP tessellation. It will not lose generality by setting $b = 1$. Then if we set $c > 0$, the line tensions are added into the non-line-tension system. Because the junctional edge are curved, the line tension produce an additional normal force which requires the three membrane faces to subtract different amount of surface tensions to keep this balance. As in Figure 2.17, since the junctional edge is curved to the direction of high pressure, thus the membrane with high two-sides pressures is subtracting more. Subsequently, to keep the balance between surface tensions and pressure difference, the value of pressures are decreased by a certain value. Similarly, since the membrane is curved to high pressure cells, higher pressure cells are subtracting more.

In order to visualize the effect of line tensions and to understand the meaning of the constant c, let us consider a two-cell example as shown in Figure 2.18. To set the scene, the two-cell system is defined by the following geometry parameters as: $\boldsymbol{q}_1 = [1, 0, 0]$, $\boldsymbol{q}_2 = [-1, 0, 0]$, $p_1 = p_2 = 1$, $\theta_1 = \theta_2 = 2$. And also the background parameters: $\boldsymbol{q}_0 = [0, 0, 0]$, $p_0 = 0$, $\theta_0 = 0$. This results in two spherical membranes and a flat membrane in the middle. The centroids and radius are: $\boldsymbol{\rho}_{10} = \boldsymbol{q}_1$, $\boldsymbol{\rho}_{20} = \boldsymbol{q}_2$, $R_{10} = R_{20} = 2$; $\boldsymbol{\rho}_{12} = \infty$,

$R_{12} = \infty$. Now the forces can be inferred from these parameters. With the general setting of parameters $(a, b, c) = (0, 1, c)$, the force solution is:

$$\begin{aligned} P_0 &= 0, \\ P_1 = P_2 &= 1 - c, \\ T_{12} &= 1 - 2c, \\ T_{10} = T_{20} &= 1 - c, \\ F_{012} &= \sqrt{3}c. \end{aligned} \tag{2.52}$$

In this example, take $c = 0$ (non-line-tension scenario), then the three membrane tension are equal $T_{10} = T_{20} = T_{12} = 1$. When considering a small amount of line tension (e.g $c = 0.1$), we see the middle tension is lower than the other two membranes $T_{10} = T_{20} > T_{12}$ so that the forces are balanced at edge.

In the example, we notice that the magnitude of the constant c cannot be too large, so as to keep all mechanical values non-negative. In fact, in the model assumptions, non-negative line tensions and surface tensions are both contractile stresses, while non-negative pressures are expansive stresses. According to (2.51), if we have set $(a, b) = (0, 1)$, non-negative solution of line tension requires $c \geq 0$. On the other hand, non-negative solution of surface tension requires $c < 1/(p_\alpha + p_\beta)$ for all membrane faces $M_{\alpha\beta}$. If so, the pressure solution is assured to be non-negative, because $c < 1/(p_\alpha + p_\beta) < 1/p_\alpha$. Taking together, the allowed range of c magnitude that can hold the assumptions is:

$$0 \leq c \leq \frac{1}{\max_{\alpha\beta}(p_\alpha + p_\beta)}. \tag{2.53}$$

In summary, two of the three zero modes are scaling factors of mechanics as in two-dimensional scenario, the other zero mode provides an additional tuning by line tensions to the non-line-tension scenario. This is an emergent flexibility of mechanics in three-dimensional multi-cellular system, by which the relative mechanical values can be different. However, this flexibility must be within a certain range.

2.5. Numerical scheme

We have constructed the inverse map from geometry parameters to the analytical solutions of mechanics. But how can we get the geometry parameters from a three-dimensional image of a cellular aggregate? To establish the numerical scheme, we first introduce the segmentation of cellular aggregates in a three-dimensional image (2.5.1). We use the membrane pixels in the image to do the least-square fitting (2.5.2), in order to get the geometry parameters and reconstruct the closest SCP tessellation. We accomplish this method by MATLAB code (2.5.3). By doing sensitivity analysis on synthetic image data, we confirm the precision and robustness of our fitting scheme (2.5.4).

2.5.1. Three-dimensional image

Numerically, a three-dimensional image is a three-dimensional matrix in which each element represents a pixel. In the segmented image of a cellular aggregate, the value of the pixel is the index of the cell that the pixel belongs to. Usually the index 1 represents the background. Sometimes the image includes the membranes, in which the membrane pixels have the value 0, as shown in the left panel of Figure 2.19. We could label a membrane pixel $\boldsymbol{r}^{(i)} = (x_i, y_i, z_i)$ as of membrane face $M_{\alpha\beta}$ if the neighbor pixels have indices α and

β. A pixel can be labeled as more than on membrane faces if it is a boundary of more than two cells. If the image does not include the membrane pixels, we could take the intermediate pixel whose neighbor pixels have different indices as the membrane pixel, as shown in the right panel of Figure 2.19 by purple nodes. Therefore, for each membrane face $M_{\alpha\beta}$, there is a set of membrane pixel locations $\{\boldsymbol{r}_{\alpha\beta}^{(i)} = (x_i, y_i, z_i)\}$. We will use these membrane pixels to fit the geometry parameters.

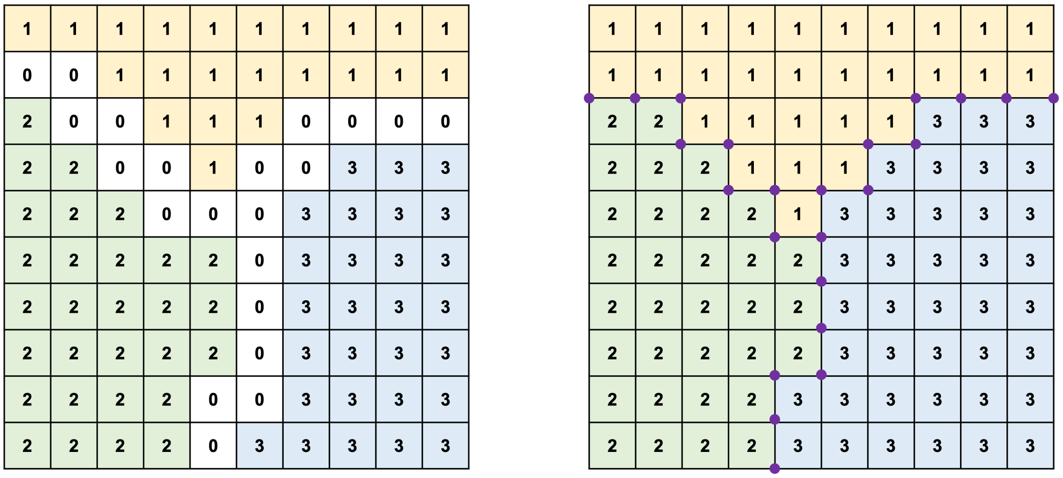

1	1	1	1	1	1	1	1	1	1
0	0	1	1	1	1	1	1	1	1
2	0	0	1	1	1	0	0	0	0
2	2	0	0	1	0	0	3	3	3
2	2	2	0	0	0	3	3	3	3
2	2	2	2	2	0	3	3	3	3
2	2	2	2	2	0	3	3	3	3
2	2	2	2	2	0	3	3	3	3
2	2	2	2	0	0	3	3	3	3
2	2	2	2	0	3	3	3	3	3

1	1	1	1	1	1	1	1	1	1
1	1	1	1	1	1	1	1	1	1
2	2	1	1	1	1	1	3	3	3
2	2	2	1	1	1	3	3	3	3
2	2	2	2	1	3	3	3	3	3
2	2	2	2	2	3	3	3	3	3
2	2	2	2	2	3	3	3	3	3
2	2	2	2	2	3	3	3	3	3
2	2	2	2	3	3	3	3	3	3
2	2	2	2	3	3	3	3	3	3

Figure 2.19. Images of segmentation

2.5.2. Least-square fitting

Given the geometry parameters of GWV tessellation $\Psi = \{\boldsymbol{q}_\alpha, \theta_\alpha, p_\alpha\}_{\alpha=1,2,\ldots,N_C}$, we could reconstruct the SCP geometry of the cellular aggregate. (Polyhedral tessellation is a special case of SCP tessellation.) For a membrane $M_{\alpha\beta}$, the centroid $\boldsymbol{\rho}_{\alpha\beta}(\Psi)$ and the radius $R_{\alpha\beta}(\Psi)$ is reconstructed as (2.25) and (2.26). We then define the deviation of a membrane pixel $\boldsymbol{r}_{\alpha\beta}^{(i)}$ from the reconstructed membrane sphere as

$$\epsilon_{\alpha\beta}^{(i)} = |\boldsymbol{r}_{\alpha\beta}^{(i)} - \boldsymbol{\rho}_{\alpha\beta}(\Psi)| - R_{\alpha\beta}(\Psi) \tag{2.54}$$

as shown if the left panel of Figure 2.20. In order to find the closest SCP tessellation which has the smallest global deviations of all membrane pixels, we can recover the best-fit geometric parameters Ψ by least-squares fitting. Specifically, we minimize the mean-squared-deviation (MSD) function,

$$E(\Psi) = \frac{1}{N} \sum_{M_{\alpha\beta}} \sum_{i=1}^{n_{\alpha\beta}} \left[|\boldsymbol{r}_{\alpha\beta}^{(i)} - \boldsymbol{\rho}_{\alpha\beta}(\Psi)| - R_{\alpha\beta}(\Psi) \right]^2, \tag{2.55}$$

where $n_{\alpha\beta}$ denotes the number of pixels belong to $M_{\alpha\beta}$ and N denotes the total number of pixels.

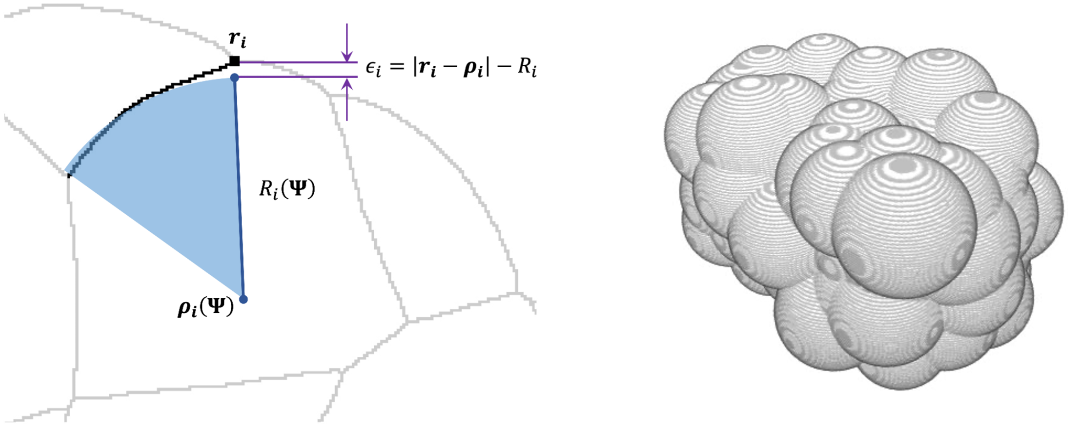
$\boldsymbol{r_i}$
$\epsilon_i = |\boldsymbol{r_i} - \boldsymbol{\rho_i}| - R_i$
$R_i(\boldsymbol{\Psi})$
$\boldsymbol{\rho_i}(\boldsymbol{\Psi})$

Figure 2.20. Least-square fitting and synthetic 3d image

Our minimization statement falls into the class of nonlinear optimization problems, requiring an educated initial guess for the desired parameters that takes advantage of the properties of SCP tessellations. First, approximately, the Voronoi site $\boldsymbol{q}_\alpha$ provide the information of cell's location in SCP tessellation. So we take the cell centers - the mean coordinate $(\bar{x}_\alpha, \bar{y}_\alpha, \bar{z}_\alpha)$ of all pixels with value α - in the image as the initial guess of $\boldsymbol{q}_\alpha$. Second, the Voronoi weight θ_α approximately provide the information of cell size. So we take the cells' length scales - the cubic root of the number of pixels with value α - in the image as the initial guess of θ_α. Third, the Voronoi power p_α is approximately the cell's pressure, which induces the membrane curvatures. According to the curvature directions in the image, we can order the pressures from high to low, and set the initial values of p_α with this order. When applying the minimization, we should also constraint the mean value of powers $\bar{p} = 1$, because the SCP tessellation is invariant to the scale of power. In summary, these are the three ways of setting the initial guess in order for the fast converging. Additional to these, specially, we set all the parameters for background $(\boldsymbol{q}_1, \theta_1, p_1)$ as zeros, and fix them in minimization. The optimization algorithm we use in code is interior-point algorithm.

2.5.3. Algorithm and codes

We accomplish the image processing and least-square fitting by the MATLAB code in Appendix A.1. This code can also output the inferred mechanical values for any given zero-mode (a, b, c). We illustrate the entire algorithm here:

- Read a three-dimensional image into a three-dimensional matrix.
- Extract the topological information by the cell adjacency in the matrix.

- Sort out the coordinates of membrane pixels.
- Set up the MSD function with given membrane pixels and Ψ.
- Compute cell centers, cell volumes, and membrane curvatures and set the initial values of Ψ.
- Use interior-point algorithm of minimizing MSD function to fit Ψ.
- Use inferred Ψ and input (a, b, c) to compute the analytical solutions of cellular pressures, surface tensions and line tensions.

2.5.4. Precision and robustness

The minimized value of $E(\Psi)$ is a global measure of the average deviation of the empirically observed geometry and the best-fit SCP tessellation. We do not know how well this fitting scheme can recover the geometry from the noisy real image data. However, as we will demonstrate below, our approach provides a finer-grained spatial information pertaining to the errors in our approximation.

Before applying our approach to a specific biological case, we first sought to assess the robustness and precision of the data-fitting scheme when applied to a synthetic image, where we have direct access to the underlying ground-truth. In order to generate the synthetic image, we first setup the image size as $300 \times 300 \times 300$. For $N_C \approx 100$ cells, we set the random GWV parameters Ψ_0 as the ground truth. The scale of weight and the distance between sites are around 50. To give the value of each pixel in the three-dimensional matrix, we compute the GWV distances $d_\alpha(\boldsymbol{r})$ from a pixel $\boldsymbol{r}$ to all sites $\boldsymbol{q}_\alpha$ and pick the shortest to assign the pixel with the cell index. Thus we construct the synthetic segmented image as shown in the right panel of Figure 2.20. In stead of adding arbitrary noise to the segmentation, we sort out the membrane pixels and inject the Gaussian noise in to the coordinates of these pixels.

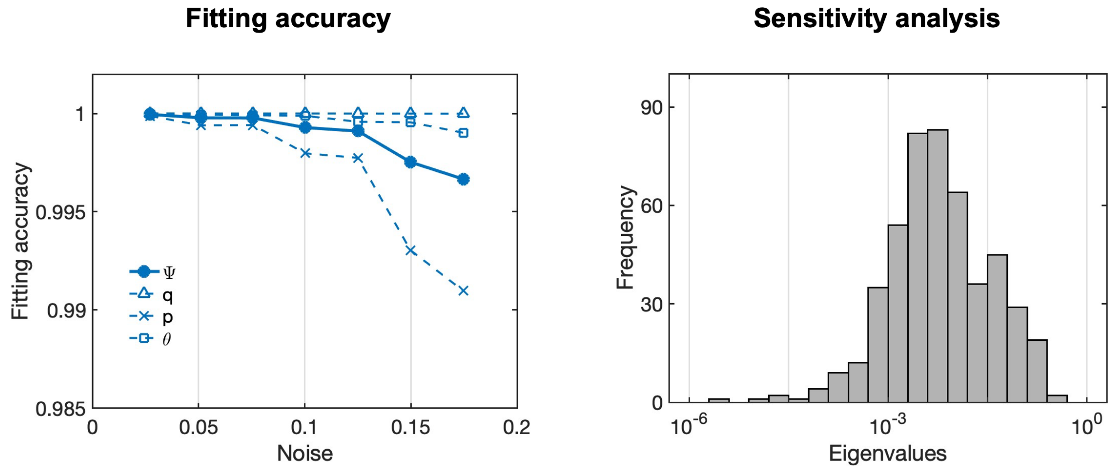

Figure 2.21. Precision and robustness

We then use the noisy membrane pixel coordinates to apply the fitting scheme, to assess the precision of the method. Our fitting scheme recovers a best-fit guess Ψ that we can compare with Ψ^*, the ground truth. The results of this comparison report the degree of mismatch, or error, between the parameters of the SCP tessellation inferred by our scheme, relative to ground truth, as a function of the degree of noise injected into the pixel coordinates. We quantify the injected noise as the square-root of the Gaussian variance normalized by cell length scale, $\sigma/\sqrt[3]{\bar{V}}$. As for the accuracy of the geometry reconstruction, we measure the correlation coefficient $\rho(\Psi^*, \Psi)$ between ground truth Ψ^* and inferred Ψ as the quantity. As shown in the left panel of Figure 2.21, although the inferred parameters of the SCP tessellation display varying degrees of susceptibility to noise, the fitting scheme recovers parameters with up to 99% accuracy with as much as 20% noise. We realize that the inference of powers p_α has the worst accuracy.

To further assess the robustness of our numerical fitting scheme, we perform a sensitivity analysis, asking to what extent do the inferred parameters of a SCP tessellation vary when we impose small perturbations of the data around some reference configuration. To assess this mathematically, we analyse the eigenvalue distribution of the system's linear response. An inference scheme is robust when all its eigenvalues are smaller in magnitude than 1, ensuring that no perturbations to the system can generate disproportionately large deviations in the values of inferred parameters. In particular, at the minimum of the MSD function, $\delta E(\Psi, \boldsymbol{r}) = 0$, thus, for any $\boldsymbol{r}_i$, there must be $\delta\epsilon_i = \delta\left[|\boldsymbol{r}_i - \boldsymbol{\rho}_i(\Psi)| - R_i(\Psi)\right] = 0$. This permits us to derive a local linear approximation, $K\delta\boldsymbol{r} + M\delta\Psi = 0$, where $K = \partial\boldsymbol{\epsilon}/\partial\boldsymbol{r}$ and $M = \partial\boldsymbol{\epsilon}/\partial\Psi$ are two matrices. As such, the relation between observed pixels perturbation $\delta\boldsymbol{r}$ and geometric parameter deviation $\delta\Psi$ is given by $\delta\Psi = L\delta\boldsymbol{r} = (-\tilde{M}^{-1}K)\delta\boldsymbol{r}$, where $\tilde{M}^{-1}$ is the pseudoinverse matrix of M. For synthetic data, we compute the eigenvalues λ_i of L and find they are all less than 1 in magnitude. The result in the right panel of Figure 2.21 indicates that the fitting scheme is robust to noise.

2.6. Conclusion

In summary, in order to do force inference to the live-images of three-dimensional cellular aggregates, we have done the following tasks in this chapter:

- In the model, we quantify the geometry of cellular aggregate as a tessellation in 3d space. On this tessellation, we model the extensive stress in cell volume as pressure, and model the 2d and 1d contractile stress on cell boundaries and edges as surface tension and line tension. All the three kinds of forces are isotropic and homogeneous within each cell, each membrane and each junctions, respectively. By assuming the system under mechanical equilibrium, we map the forces to the geometry through Young-Laplace equations and tension balance equations.

- The mapping confined the permissible geometry of tessellation to the class of SCP tessellation. We count the dimensionality of such tessellation is $5N_C$ for N_C cells, which can be parameterized by GWV parameters. Using these independent parameters, we construct the inverse mapping from SCP tessellation space to the solution space of mechanics. This inverse mapping is analytical but not unique, because three undetermined parameters provide the zero modes of forces that give out the same geometry.
- For any given segmented images, we set the numerical scheme of least-square fitting to the membrane pixels with respect to GWV parameters. Verified by synthetic images, the numerical scheme is accurate and robust to the noise in segmentation. Combined with the analytical inverse mapping, this method enable the force inference on the 3d image of cellular aggregates.

Empirically, these works provide a lot of utilization for physicist and biologist investigating the multi-cellular system:

- It provides a useful tool that people can infer the forces of developing embryos without invasion. Studies that need force data to understand biophysical mechanisms can benefit from it.
- The force equations provide the ability of simulating three-dimensional geometry evolution. It can be used to check hypothesis and provide quantified evidence.

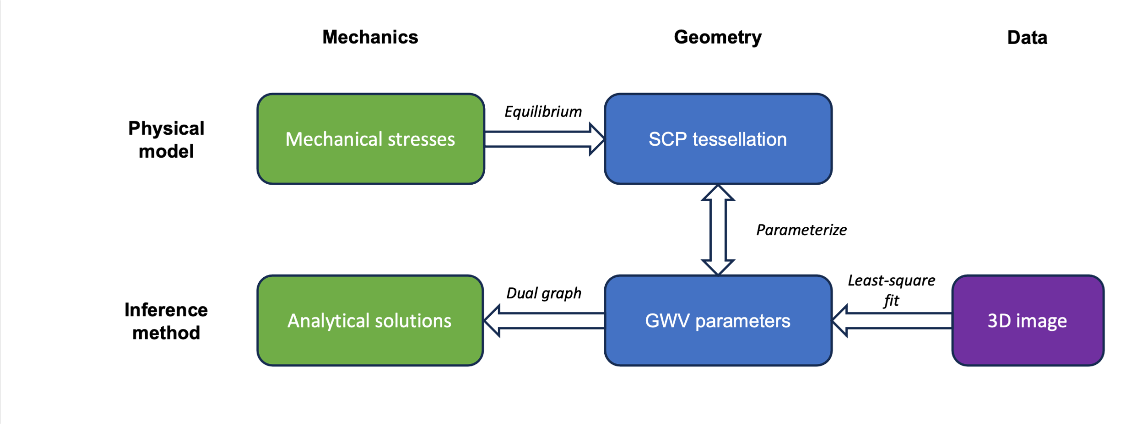
Mechanics
Geometry
Data
Physical model
Inference method
Mechanical stresses
Equilibrium
SCP tessellation
Parameterize
Analytical solutions
Dual graph
GWV parameters
Least-square fit
3D image

Figure 2.22. Summary of physical model and inference method

- It also offers a simple tool of quantifying the three-dimensional geometries of tessellations beyond the field of biology. Such tessellations are also shown in many engineering problems and material science.

Theoretically, in the model that has been constructed, there are several non-trivial consequences emerge from the mathematical structure of the multi-component system:

- In three-dimensional tessellations, the simple geometry - constant curvatures of interfaces and edges - can induce the complex constrains between components. This results in the low-dimensionality of the multi-cellular geometry space.
- The duality between geometry and mechanics implies the deep relations of these two spaces. The subsequent zero modes of the equilibrium system imply the increasing flexibility of mechanics when turning from 2d to 3d.

CHAPTER 3

A mechanical atlas of ascidian gastrulation

3.1. Background

In Chapter 2, we introduced a force inference method for three dimensional cellular aggregates and a numerical scheme of fitting geometric parameters from three-dimensional image data. In this chapter, we apply the force inference method and numerical scheme on a developmental process of ascidian embryo called gastrulation. We get the results of geometry reconstruction, mechanical atlas and lineage maps. We also analyze the mechanical flexibility in this process and discover the biological principles of embryogenesis.

Before talking about results and analysis, let us introduce the biology system of ascidian gastrulation (3.1.1 & 3.1.2) and the techniques of 3d living image (3.1.3).

3.1.1. Ascidian embryo

Ascidian is a model organism of studying developmental process. In the first 3-4 hours after fertilization, the zygote undergoes a series of rapid and highly synchronized cell divisions called cleavages. Cleavage in ascidians is known for its highly predictable, invariant pattern of cell divisions. By the 64-cell stage, each blastomere, or cell resulting from division, has a predictable fate in terms of the tissues it will generate. During this stage, embryo also establish the primary body axes (anterior-posterior and animal-vegetal). Cell names are given according to their lineages and positions relative to the body axes.

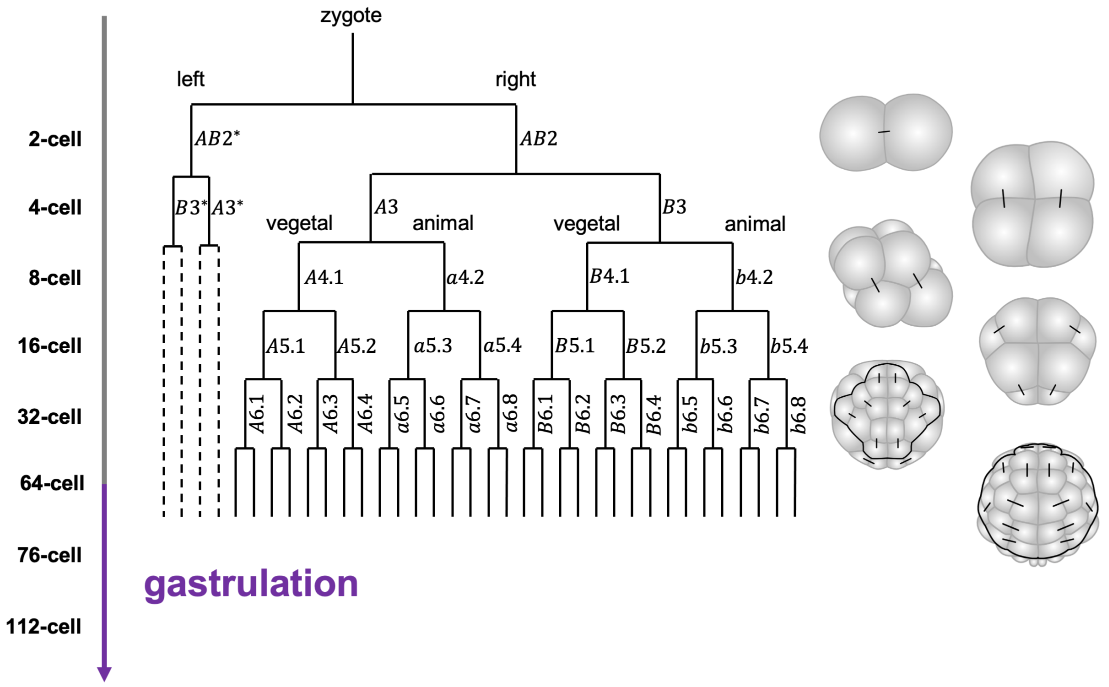
zygote
left
right
2-cell
4-cell
8-cell
16-cell
32-cell
64-cell
76-cell
112-cell
gastrulation
AB2*
AB2
B3*
A3*
A3
B3
vegetal
animal
vegetal
animal
A4.1
a4.2
B4.1
b4.2
A5.1
A5.2
a5.3
a5.4
B5.1
B5.2
b5.3
b5.4
A6.1
A6.2
A6.3
A6.4
a6.5
a6.6
a6.7
a6.8
B6.1
B6.2
B6.3
B6.4
b6.5
b6.6
b6.7
b6.8

Figure 3.1. Developmental stages of ascidian embryo

More specifically, as shown in Figure 3.1, the first cell division gives the left half and right half of the future body. The body plan is left-right symmetric until very later stages of embryo development, thus the names of the pair cells are the same with the left half labeled by $*$. Then the following two rounds of cells divisions decide two more axes: cell names with letter A and B give embryo's vegetal half of anterior and posterior respectively; cell names with letter a and b give embryo's animal half of anterior and posterior respectively.

Following cleavage, the ascidian embryo will undergo gastrulation, a process that dramatically reshapes the embryo. The cells move and rearrange to form three germ layers:

the ectoderm, mesoderm, and endoderm. This process forms a structure called the gastrula. Each cell has more specific cell fate during this stage. Specifically, the ectodermal cells are all animal cells, will become future skin and nerve system; the endodermal cells are $A7.1-2, A7.5$ and $B7.1-2$ in the vegetal half, will become future digest system and other in-body organs; the other vegetal cells belong to mesoderm, will become future muscle and blood.

3.1.2. Early gastrulation process

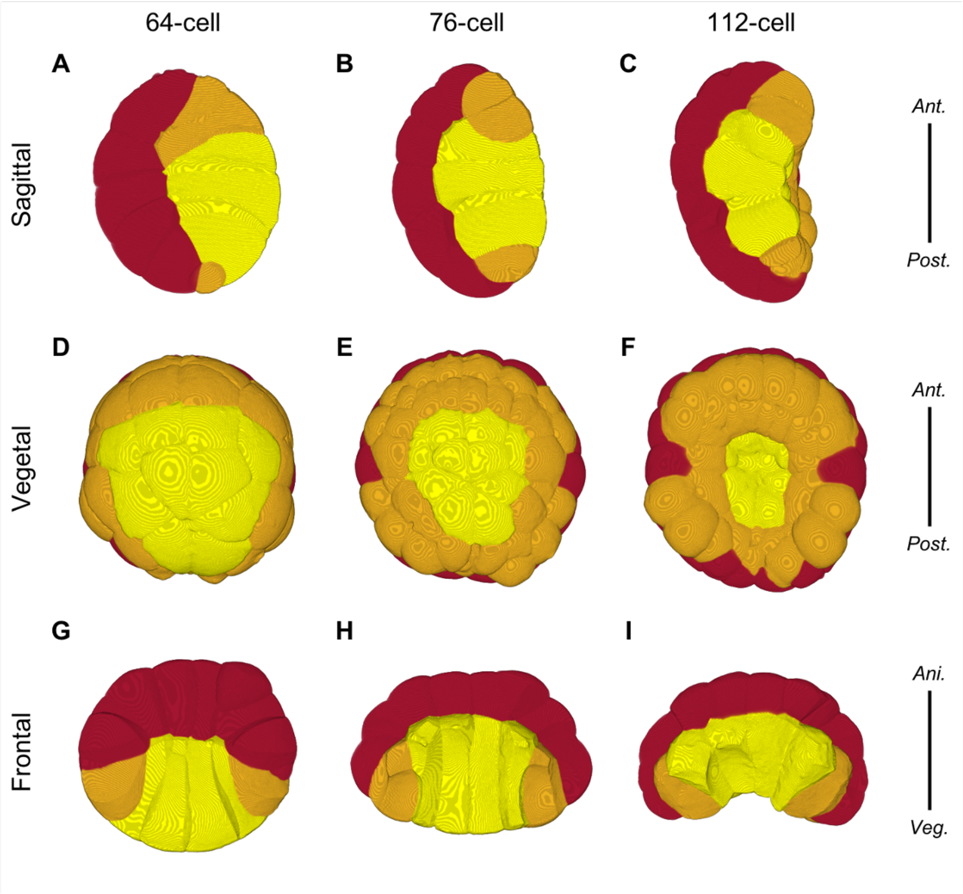
64-cell
76-cell
112-cell
A
B
C
Sagittal
Ant.
Post.
D
E
F
Vegetal
Ant.
Post.
G
H
I
Frontal
Ani.
Veg.

Figure 3.2. Early gastrulation of ascidian embryo

Here we focus on the the early stages of gastrulation in which the ten endodermal precursor cells (yellow in Figure 3.2) invaginate to form a large indentation on the vegetal side of the embryo. Previous studies identified two distinct phases of endoderm invagination. The first phase is from 64-cell stage to 76-cell stage, while the mesodermal cells are dividing. During this phase, the apices of endodermal cells constrict while the cells remain columnar in shape. The second phase is from 76-cell stage to 112-cell stage, while the ectodermal cells are divising. During this phase, the apices remain constricted, while the cells shorten apico-basally, accompanied by bending of the endodermal cell sheet, a process referred to as "collared rounding".

Accumulation of mono-phoshorylated (1P) myosin II on the apical surfaces of endoderm cells accompanies their apical constriction during phase 1, while collared rounding is accompanied by the circumapical accumulation of di-phosphorylated (2P) myosin II, and basolateral accumulation of 1P myosin II. 2D vertex models asserting patterns of surface and line tensions consistent with the observed patterns of myosin II could recapitulate the two phase kinematics of endoderm invagination, supporting the idea that lineage specific deployment of myosin II plays a central role in orchestrating these morphogenetic dynamics. Although limited by its 2D perspective, this prior work provides a frame of reference for evaluating the results of 3D force inference.

3.1.3. Live-image data

Recently, Guignard et al [**8**] combined confocal multiview light-sheet imaging and an algorithm of image segmentation - called ASTEC - to reconstruct the boundaries of all cells within the ascidian embryo at 2 minute intervals during early ascidian development

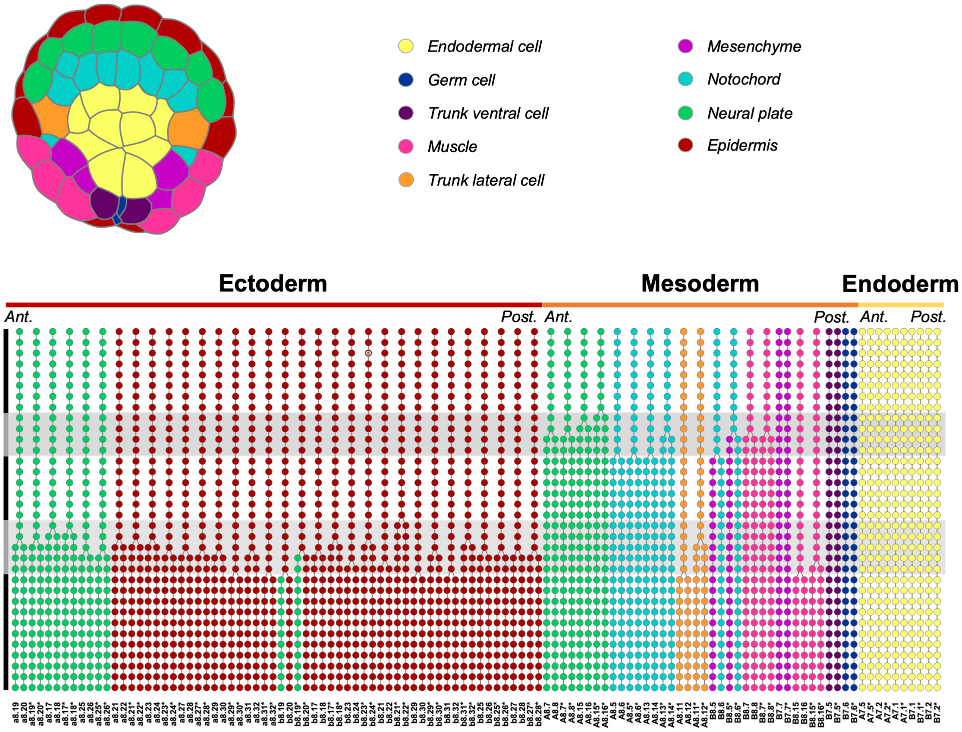
Endodermal cell
Germ cell
Trunk ventral cell
Muscle
Trunk lateral cell
Mesenchyme
Notochord
Neural plate
Epidermis
Ectoderm
Mesoderm
Endoderm
Ant.
Post.
Ant.
Post.
Ant.
Post.
64-cell
76-cell
112-cell

Figure 3.3. Cell fates of ascidian gastrulation

with isotropic resolution. The digitized P.mammillate embryos constitute a quantitative and dynamic atlas of cell positions, geometries, and ancestry over a large fraction of a metazoan developmental program, which can be interactively explored through the MorphoNet online morphological browser. These tools provide us the 3d live-image dataset to the ascidian gastrulation process.

We work on three embryos from the dataset, taking out the timepoints from 64-cell stage to 112-cell stage. One typical embryo with the highest quality have 34 timepoints for early gastrulation: timepoints $1-8$ are 64-cell stage; $13-18$ belong to 76-cell stage; $24-34$ belong to 112-cell stage; the timepoints $9-12$ and $19-23$ are two rounds of cell division. See the lineage maps of cell-fate in Figure 3.3.

3.2. Geometry reconstruction of ascidian embryo

Using the numerical scheme, we are able to fit the geometry parameters of GWV from three-dimensional live-image data of ascidian gastrulation. We then reconstruct the geometry of SCP tessellation and infer the mechanical parameters across all time points during gastrulation stage. We first assess the geometry reconstruction by analyzing the fitting errors (3.2.1). We find large fitting errors during cell division and improve the fitting results by re-segmenting the image (3.2.2). Despite these time points, we see small fitting errors and make two consequent statements in 3.2.3: 1) It is possible to use low-dimensional geometries describing the morphogenesis; 2) Ascidian gastrulation can be simplified as a quasi-static process.

3.2.1. Assessment of geometry reconstruction

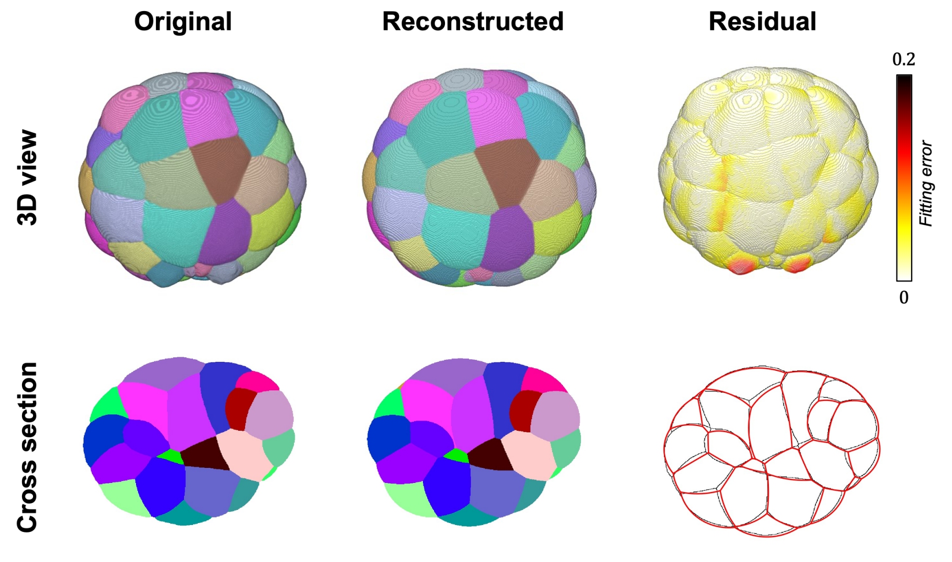

Figure 3.4. Geometry reconstruction of ascidian embryo

In the left column of Figure 3.4, we show an original segmentation of ascidian embryo at 64-cell stage in 3d view by the software *ImageJ*. The cross-sectional view of the same embryo is shown as well. We then fit the GWV parameters Ψ from the image data, and reconstruct the SCP geometry that best-fits the original image. To reconstruct the SCP tessellation based on these parameters, we create a new 3d image with the same size and resolution as the original image. We labeled every pixel $\boldsymbol{r}$ by the cell index α, which has the shortest Voronoi distance $d_\alpha^2(\boldsymbol{r})$ among all cells. The reconstructed embryo is presented in 3d view, and is presented in cross-sectional view in the middle column of Figure 3.4. Qualitatively, upon visual inspection the geometries are well reconstructed. To assess quantitatively the quality of geometry reconstruction, we visualize the local spatial errors $|\epsilon_i|$ of every membrane pixels in the top right panel of Figure 3.4. After normalized by the cell size (≈ 40 of pixel units), globally, the errors are observed to be small on the order of a few percent. The largest systematic error in Figure 3.4, on the order of $10\% - 15\%$, is observed in the mirror-symmetric cells within the mesoderm lineage, whose apical surface shapes clearly deviate from uniform curvature. Overlaying the outlines of original cross-sectional image and the reconstruction provides further insights into the nature of small errors within the bulk of the embryo (bottom right panel of Figure 3.4).

Taking together the fitting errors of all pixels, we make a histogram of error degrees to visualize the distribution in Figure 3.5. As shown in the figure, it is close to Gaussian distribution whose standard deviation is 4.3%. According to the results of synthetic image, in which the membrane pixels are given Gaussian pixels, this deviation mean we recovered the geometry with more than 99% accuracy.

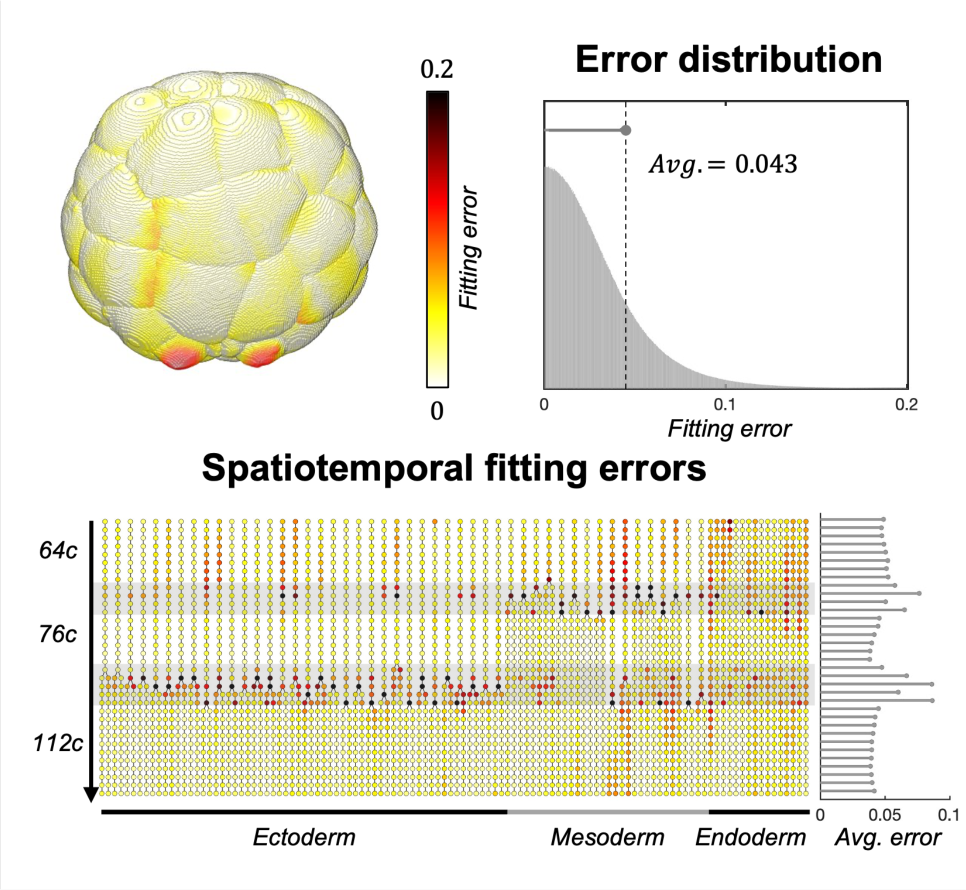

Figure 3.5. Error distributions of geometry fitting

These results highlight the precision within which an SCP tessellation approximates the ascidian embryo at a single time point. To provide a more global assessment, we mapped per-cell approximation errors onto the lineage of the ascidian embryo during early gastrulation, organized by the degree of temporal progress (from 64 to 112 cells) and germ layer, where the color displayed upon the lineage corresponds to the degree of error, per cell (Figure 3.5). We realize that the large fitting errors appear at the cells when they are about to divide. The time series data of standard deviation in Figure 3.5 also shows a wave of high average error degrees appear at cell division time points. The fail of the SCP approximation is because the dumbbell-like shapes of the cells just prior to the computational identification of a new membrane in the segmentation protocol.

3.2.2. Improvement of fitting by re-segmentation

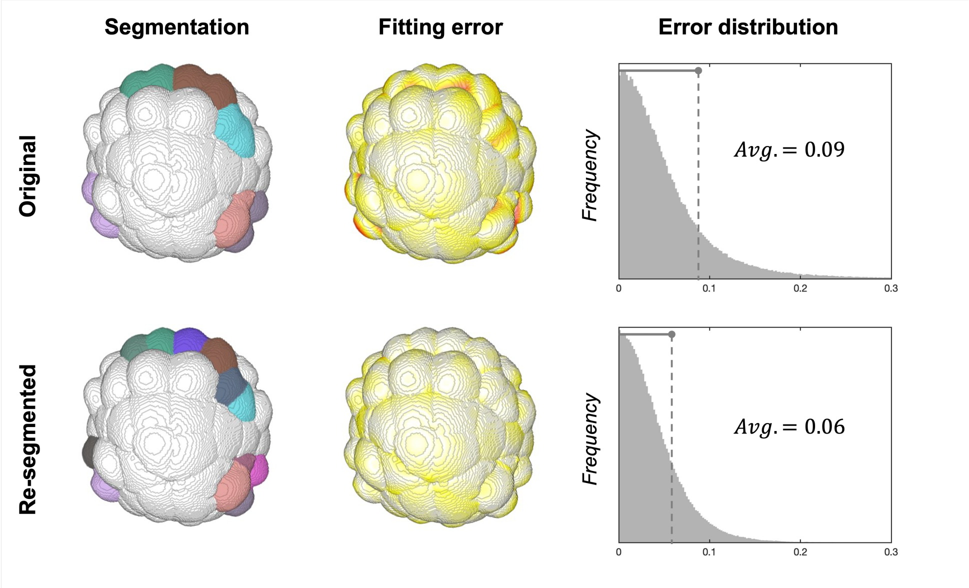

Figure 3.6. Improvement of fitting by re-segmentation

The failure of the fittings for the cells about to divide can be improved by re-segmentation on the original image. In the top left panel of Figure 3.6, we highlight the cells of dumbbell-like shapes at the time point of cell-division stage from 64-cell to 76-cell. In the top middle panel of Figure 3.6, we present the fitting errors of apical membrane pixels. We notice that the large errors are not only appears at the dumbbell-like cells, but also at their neighbor cells, because our numerical scheme is global fitting. By comparing this image with the image of subsequent time point, where these cells are segmented into two daughter cells, we relabel the cell pixels by two new cell indices. The method is to compute the distances from the pixel to both cells in next time point, then choose the shorter distance and label the pixel with corresponding new index. In the bottom left panel of Figure 3.6 we present the re-segmented cells. Apply the numerical scheme onto the image of re-segmentation, we observe much smaller fitting errors as shown in the bottom middle panel of Figure 3.6. Comparing the error distribution in the right column of Figure 3.6, the standard deviation is largely reduced from 9% to 6%. This result is another evidence supporting the accuracy of the model fit's to the data.

3.2.3. Consequences of fitting results

These numerical data strongly support the argument that SCP tessellations accurately approximate the time-evolving geometry of the ascidian embryo. We emphasize the dramatic reduction in the dimensionality of the geometric parameterization proposed here. The original image of segmentation requires thousands of pixels to delineate the membranes of each cell, and the 3D computational meshes employed to render the shape of each cells employs hundreds of triangular meshes. In contrast, we have demonstrated that with only five parameters per cell an SCP tessellation can provide a highly accurate rendition of an entire embryo. This physically and biologically motivated geometric description not only facilitates the inference of it's mechanical configurations, but also provides a low-dimensional parameter space that can quantitatively describe morphogenetic trajectories.

Recounting, the biological ingredients to the theory were that 1) isotropic and homogeneous cell pressures, and membrane and line tensions, are in 2) balance with each other according to effective Young-Laplace relations at membranes and lines, and 3) that the line tensions themselves are in a static balance with each other at each vertex. The unreasonable quality with which an observed embryonic geometry can be approximated by an SCP tessellation provides strong support for the quality of biological and physical ingredients into the theory. In particular, the quality of the fit to real data suggests the emergence of mechanical simplicity from the manifest chemical and mechanical complexities at shorter lengthscales and timescales.

Time-dependent scalar quantities of cell pressures, and membrane and line tensions, which abide by effectively fluid-like balances of normal stresses at membranes and lines are sufficient to represent the mechanical state. In addition to the support for material simplifications, the quality of the data fits suggests that cells within the ascidian embryo are close to a static equilibrium of forces. Deviations from this would introduce strong velocity-dependent dissipative components to the stresses, resulting in geometries that would be poorly approximated by SCP tessellations. The observed dynamics can thus be considered the result of "adiabatic" changes in the configuration of the mechanical state, the morphogenetic timescale being much larger than the mechanical relaxational timescales of the system. From a biological perspective, the observation that the entirety of the embryo dynamically maintains such proximity to a static equilibrium makes a theoretical prediction of feedback mechanisms that globally coordinate the generation and regulation of forces to maintain this condition.

3.3. Patterns of mechanical atlas

After reconstructing the geometry of ascidian embryo during early gastrulation accurately, we infer the mechanics from the geometric parameters by the method of dual graph. Given a choice of the zero mode, this inference allows us to construct the first mechanical atlas of all three kinds of mechanical inputs at any time point (3.1.1). Does the spatio-temporal patterns of mechanics recover previous understanding of ascidian gastrulation? What are the new findings that disagree with or neglected by previous theory? In order to answer these questions, we first visualize and quantitatively describe the overall spatial patterns of symmetries and asymmetries (3.3.2). Then we visualize and quantitatively describe the spatial patterns of pressures (3.3.3) and tensions (3.3.4) in detail, and analyze the correlations between them. We finally analyze the spatio-temporal patterns via lineage maps (3.3.5), find out the cell-cycle dependent and independent features of mechanical atlas.

3.3.1. Constructing and visualizing mechanical atlas and lineage maps

We have recovered the geometric parameters from 3d live-image of ascidian embryos from 64-cell stage to 112-cell stage. Base on these parameters, we find out the zero mode parameters are restricted in the range of $0 \leq c/b \leq 0.1$ to keep the stress positive. We set $a = 0$ and $b = 1$ without loss of generality in spatial pattern, and we choose a median value of $c = 0.05 = c_{max}/2$ to compute the values of pressures, surface tensions and line tensions. The ambiguity associated with this specification of zero-mode c is discussed in great detail later in this chapter. By coloring the cells, membrane faces and junctional edges with corresponding magnitude of forces, we visualize the embryo in 3d using *ImageJ*. In Figure 3.7, we pick up one time point from each stage (64-cell, 76-cell and 112-cell) to present the three types of the mechanical atlas, because the patterns remain largely constant in between rounds of cell divisions. Because the more heterogeneous patterns emerge on the vegetal side than on the animal side, we present vegetal views in Figure 3.7. Besides the visualization of apical mechanics, we also present the cross-sectional view of pressures and surface tensions in the right column of Figure 3.7 with distinct color scheme, in order to show the in-bulk patterns of embryos.

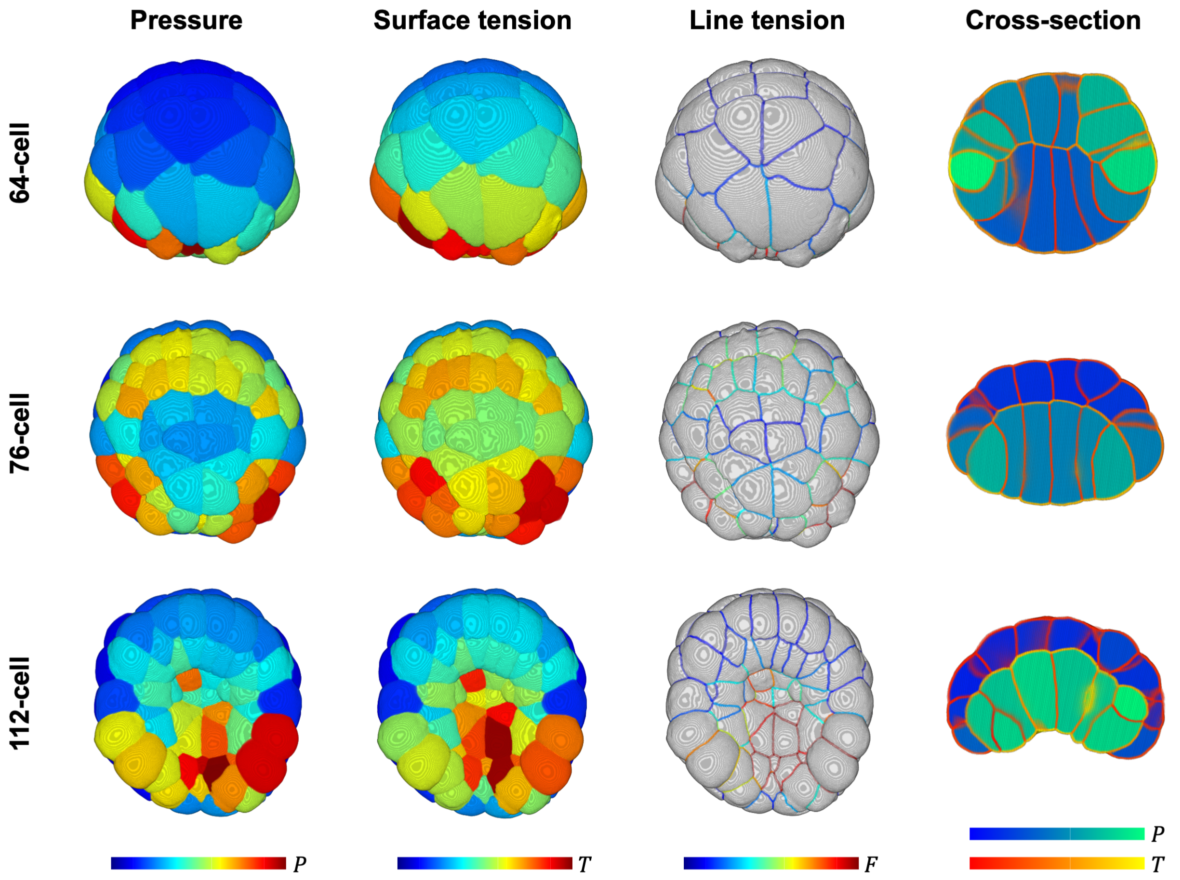
Pressure
Surface tension
Line tension
Cross-section
64-cell
76-cell
112-cell
P
T
F
P
T

Figure 3.7. Mechanical atlas of ascidian gastrulation

To further present the detailed in-bulk patterns and overcome the limitations of three-dimensional visualization, we separate the membranes into five groups based on the double-layer structure of embryos. As shown in Figure 3.8, the embryo have a layer of animal cells and a layer of vegetal cells, thus there are two apical membrane groups. The membranes between two animal cells belong to animal lateral group, while the membranes between two vegetal cells belong to vegetal lateral group. In the middle, the membranes between an animal cell and a vegetal cell belong to basal group. The junctions are separated in a similar way. Therefore, from the same view angle as in Figure 3.7, we visualize the in-bulk force patterns of these five groups in Figure 3.11 and Figure 3.13.

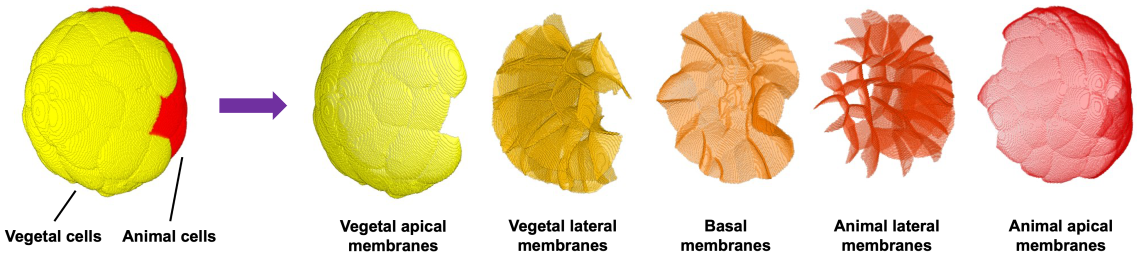

Figure 3.8. Five groups of ascidian membranes

In order to show the detailed temporal patterns, we construct the lineage maps of mechanical forces in Figure 3.15. From top to bottom, each row of the lineage maps represent a timepoint; and each node in the maps represent a cell with the color showing the force value. The cells have been sorted according to germ layers, and by the relative locations of cells along the anterior-posterior axis, within each germ layer. When investigating temporal patterns, we should determine the mechanical scale for each timepoint. In another word, we need to set the zero mode parameter b of each timepoint to normalized mechanical values. In Figure 3.15, the total volume energy $E_V = \sum_\alpha P_\alpha V_\alpha$ is set to be fixed over time, and the values of b are set accordingly. The ambiguity associated with this specification of zero-mode b is discussed in great detail later in this chapter as well.

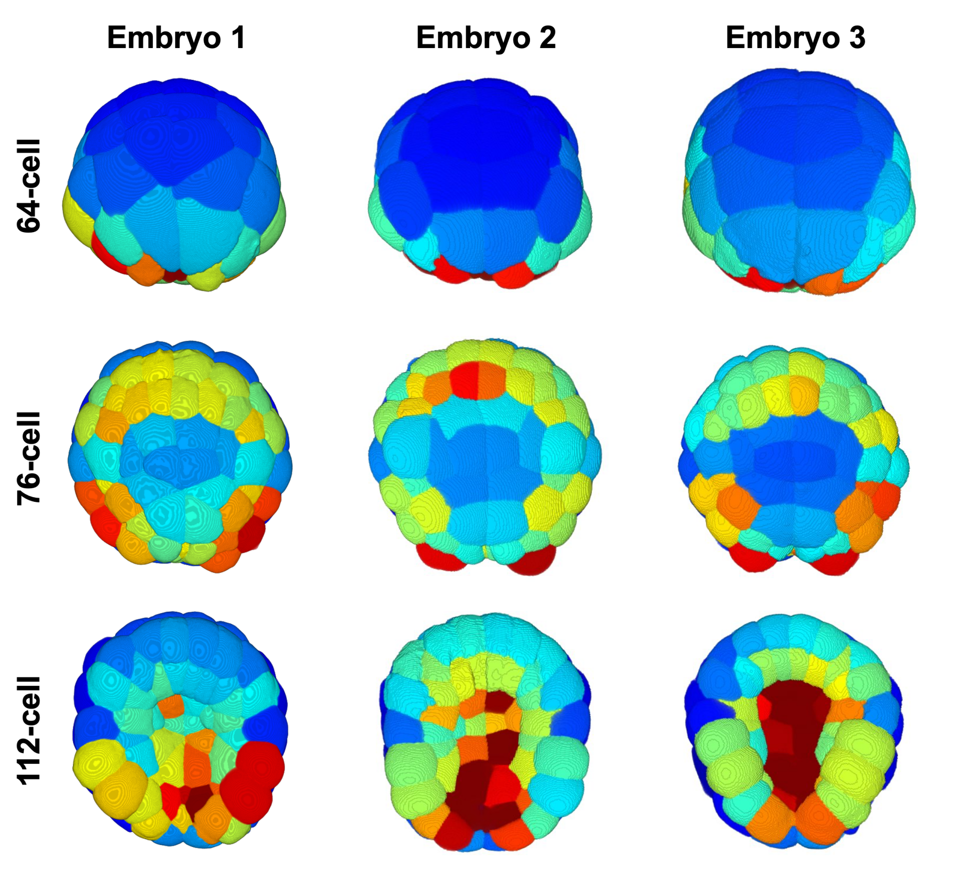

Figure 3.9. Reproducible pressure patterns in three embryos

Although we choose the certain values of zero-modes, the spatio-temporal patterns of mechanics are highly producible across three different embryos. This qualitative results provide another evidence for the robustness of our force inference method. Additionally, the continuity of mechanical states with respect to subsequent timepoints also give us the confidence in the biological relevance, accuracy and robustness of our mechanical atlas of ascidian gastrulation.

3.3.2. Symmetries and asymmetries of ascidian mechanical patterns

At this stage of ascidian development the embryo is expected to display symmetry about its left-right axis. The mechanical atlas makes manifest the mechanical symmetries in both cellular pressures and membrane/line tensions. While there may be slight variations in magnitude between the left and right halves - for example at 112-cell stage, where the right B7.1-2 and B8.7-8 cells demonstrate higher pressures and apical membrane tensions than the left counterparts - the regions with relatively high force value are approximately identical. The panel A in Figure 3.10 quantifies the degree of mechanical symmetry the atlas predicts.

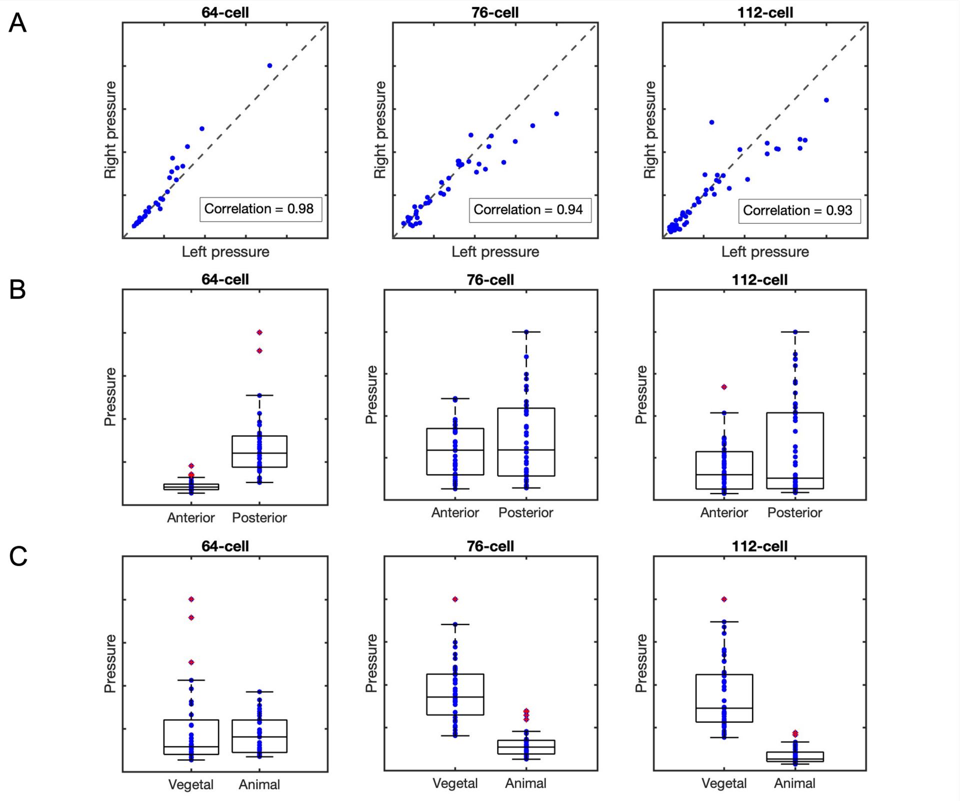

Figure 3.10. Symmetries and asymmetries of ascidian mechanical patterns

The transcriptomic asymmetry in the ascidian embryo, with respect to the anterior-posterior and animal-vegetal axes, is established very early in development, specifically during the 4-cell to 16-cell stage. This initial establishment of asymmetry is attributed to the graded distribution of maternal proteins, as well as the localization of maternal mRNAs, like macho-1, in the posterior animal regions. These asymmetric influences continue to be prominent throughout the later stages of development, extending into gastrulation, thereby resulting in varied cell fates across different regions of the embryo. Our mechanical atlas reflects these asymmetries: at the 64-cell stage, a distinct gradient of mechanical forces from posterior to anterior is evident, as illustrated in the first row of Figure 3.7 and quantified in the panel B of Figure 3.10. As development progresses from the 76-cell to the 112-cell stage, the posterior portion of the embryo continues to exhibit elevated pressures and apical tensions, as presented in the second and third rows of Figure 3.7. Furthermore, the asymmetry between the animal and vegetal layers of cells becomes increasingly manifest when we observe the changes in pressures and membrane tensions in the cross-sectional views presented in the last column of Figure 3.7. At the 64-cell stage, vegetal cells exhibit relatively lower pressures and tensions, but this changes as development progresses to the 76 and 112-cell stages. At these later stages, the vegetal cells display noticeably higher pressures and membrane tensions when compared to their animal counterparts, as quantified in the panel C of Figure 3.10.

Consequently, we observed the symmetry in left-right mechanical pattern, and the asymmetries in anterior-posterior and vegetal-animal axis. These align with and reinforce prior findings in the field of ascidian development, reflect the symmetric and asymmetric natures of the embryo. Taken together with the quality of the model's fit to the data, its temporal robustness, reproducibility across embryos, these observations give us confidence in the biological relevance, accuracy and robustness of our mechanical atlas of ascidian gastrulation.

3.3.3. Pressure heterogeneity

As the vegetal-animal asymmetry of mechanics arise from 76-cell stage to 112-cell stage, more complex patterns beyond a/symmetries are shown in vegetal cells. These patterns are related to germ layers and cell fates in Figure 3.3. In reference to the left column of Figure 3.7, during 76-cell stage, endoderm cells ($A7.1-2$, $A7.5$, $B7.1-2$) exhibit comparatively lower pressures than mesoderm cells. In the anterior region, the mesoderm cells ($A8.5-8$, $A8.13-16$) - notochord and neural plate cell fates - begin to generate elevated pressures. In conjunction with the consistently high mechanical values in the posterior mesoderm cells, these cells collectively form a ring of heightened pressure encompassing the lower-pressure endoderm. This pattern relates to the flat side of the hemisphere shape of the embryo at 76-cell stage. As the development progresses to the 112-cell stage, endoderm cells start to increase their pressure generation, a mechanical transformation aligning with the invaginating morphological configuration of the embryo.

3.3.4. Surface and line tension pattern

The heterogeneities in cellular pressures are found to have a direct relationship with the configurations of surface tension and line tension. To depict this relationship, we present the full mechanical atlas of surface tensions in Figure 3.11 and line tensions in Figure 3.13. Our investigation elucidates three key ways in which surface tensions are associated

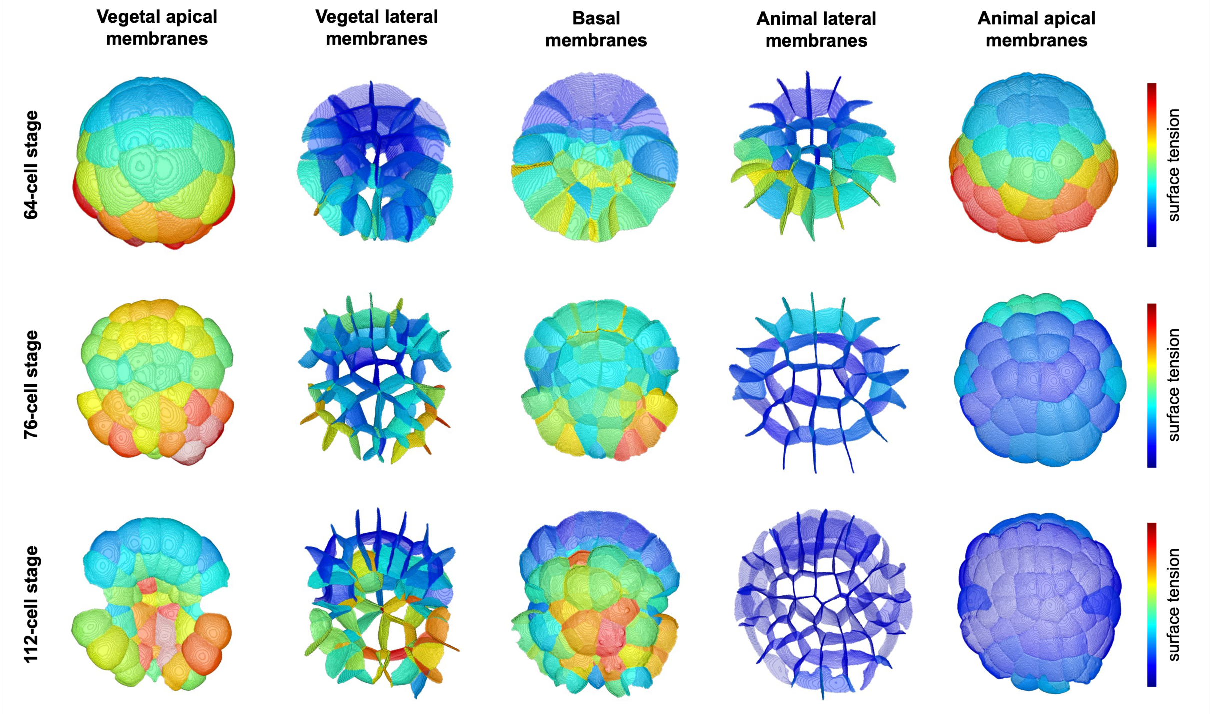
Vegetal apical membranes
Vegetal lateral membranes
Basal membranes
Animal lateral membranes
Animal apical membranes
64-cell stage
76-cell stage
112-cell stage
surface tension
surface tension
surface tension

Figure 3.11. Mechanical atlas of surface tensions in ascidian gastrulation

with cellular pressures. First, apical membrane tensions display a direct correlation with cellular pressures, an association derived from the similar curvatures across all apical membranes, as quantified in the panel A of Figure 3.12. Second, the surface tensions of lateral membranes are correlated with the mean cellular pressures on both sides, as quantified in the panel B of Figure 3.12. Third, The surface tensions of basal membranes are correlated with the corresponding cellular pressures on the vegetal side - see panel C of Figure 3.12. Beyond these correlations, it is noteworthy that for most of the vegetal cells, the lateral membranes generally exhibit lower surface tensions than those of apical and basal membranes. This observation contrasts with the measurement of myosin motor activities, especially for the endodermal cells at 112-cell stage.

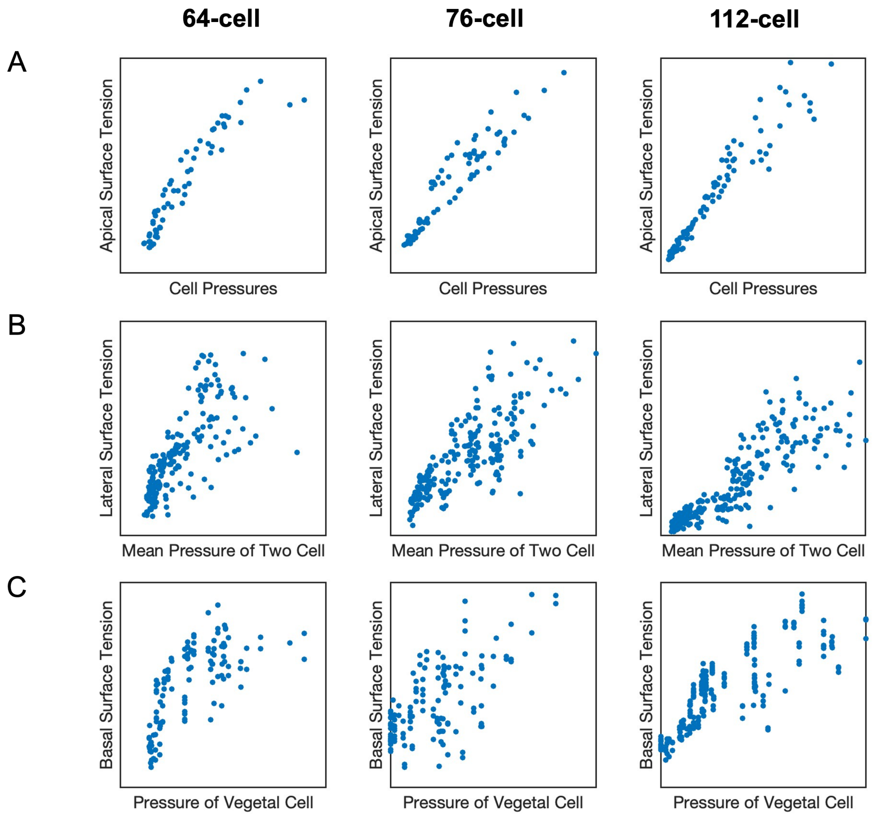

Figure 3.12. Correlations between pressures and membrane tensions

The relationship between pressures and line tensions follows similar rules as those for surface tensions. For apical junctions, which are formed by two cells, it is observed that high line tensions manifest at the boundaries of two high-pressure cells. The panel A of Figure 3.14 quantify the correlation between apical line tension and the mean pressure of the corresponding two cells. As for lateral and basal junctions, which are formed by three cells, high line tensions emerge when at least two of the corresponding three cells exhibit high pressures - see panel B of Figure 3.14. For instance, at 112-cell stage as shown in the panel C in Figure 3.14, basal junctions can be separate into to subgroups: the junctions formed by two vegetal cells and one animal cell, and the junctions formed by one vegetal cell and two animal cells. Notebly, the line tensions in the first subgroup is higher than the second subgroup. In summary, the junctions formed by two or three high-pressure cells generally exhibit high line tensions, while the junctions formed by only one or zero high-pressure cell typically exhibit low line tensions.

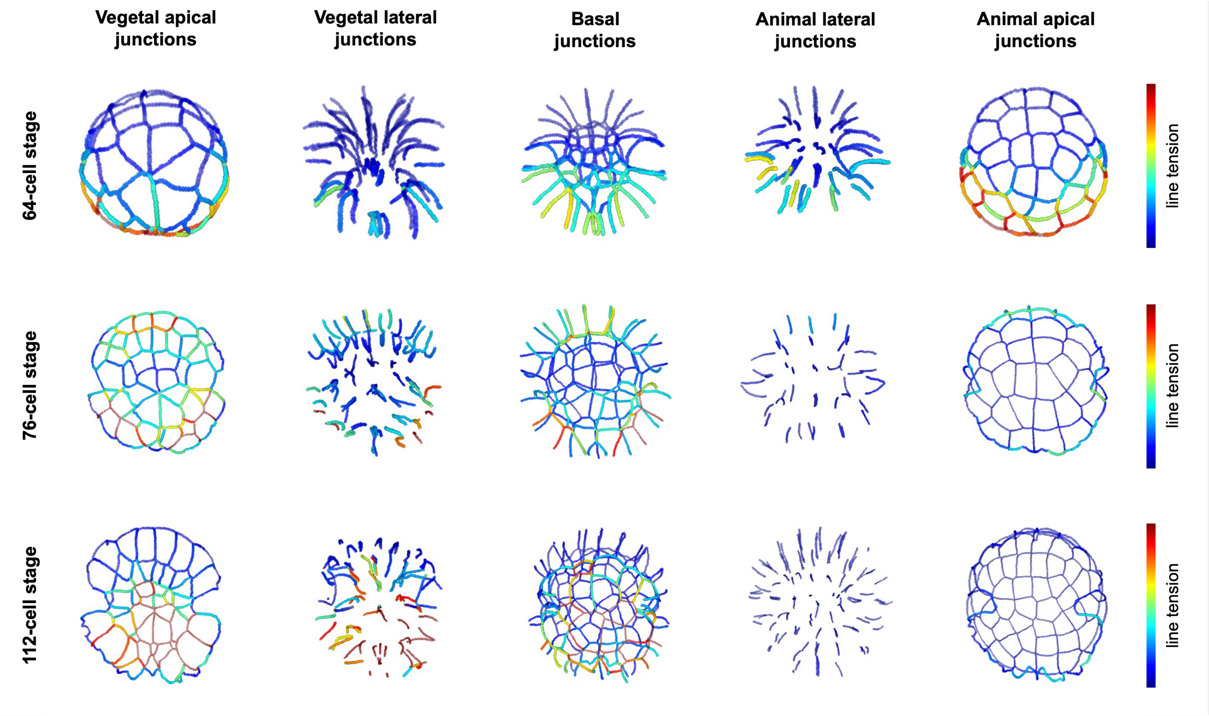
Vegetal apical junctions
Vegetal lateral junctions
Basal junctions
Animal lateral junctions
Animal apical junctions
64-cell stage
76-cell stage
112-cell stage
line tension
line tension
line tension

Figure 3.13. Mechanical atlas of line tensions in ascidian gastrulation

Consequently, our mechanical atlas reveals that you must account for significant patterned heterogeneities in cell pressures to explain the observed geometries through the process of gastrulation. The configurations of surface tensions and line tensions are highly correlated with the pressure heterogeneities. These observations highlight the importance of developing new approaches to measuring the mechanical stress state of an embryo that go beyond a focus on the forces generated by the actomyosin cytoskeleton.

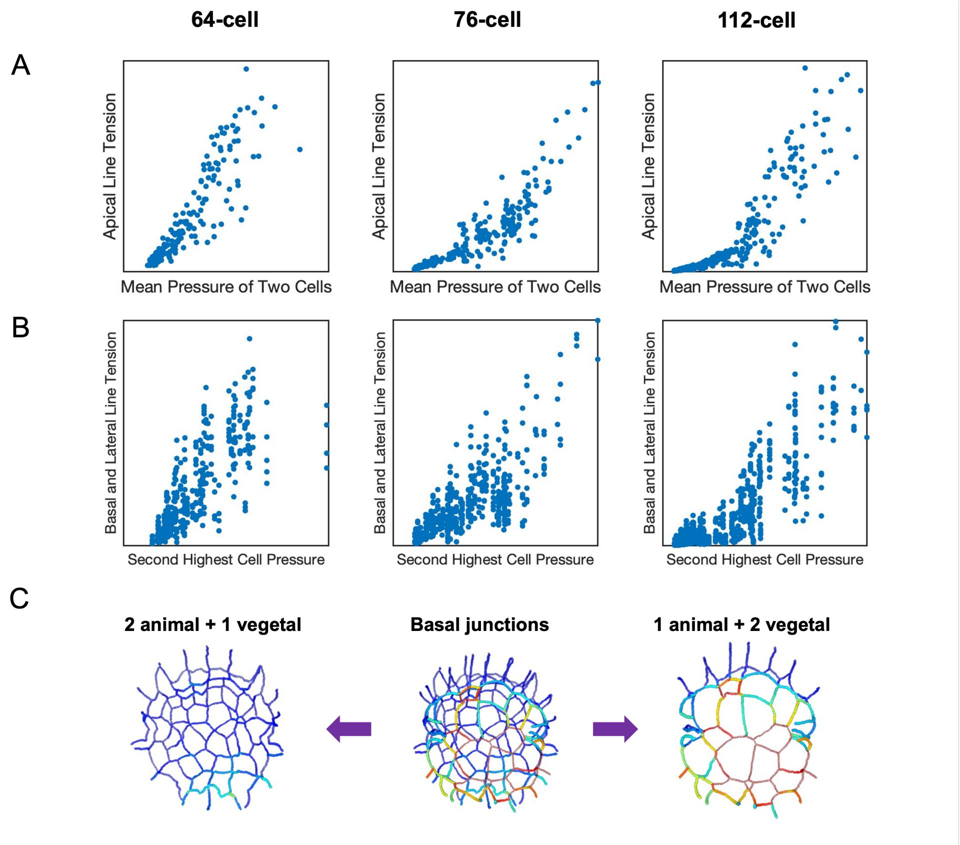

Figure 3.14. Correlations between pressures and line tensions

3.3.5. Lineage map

A virtue of the stereotyped lineage of ascidian embryos is that we can display the mechanical data on the invariant lineage maps. In Figure 3.15 we can see the time-dependent trajectories of pressures in cells. The lineage view of the mechanical data makes apparent the very strong lineage-dependent patterns, with only the mesoderm displaying an increase in pressures prior to the 112-cell stage, and the ectoderm never showing a significant change in its pressure distributions. Furthermore, at the 112-cell stage when the embryo begins to invaginate, there is a clear anterior-posterior gradient in cell pressures within the mesodermal layer of cells.

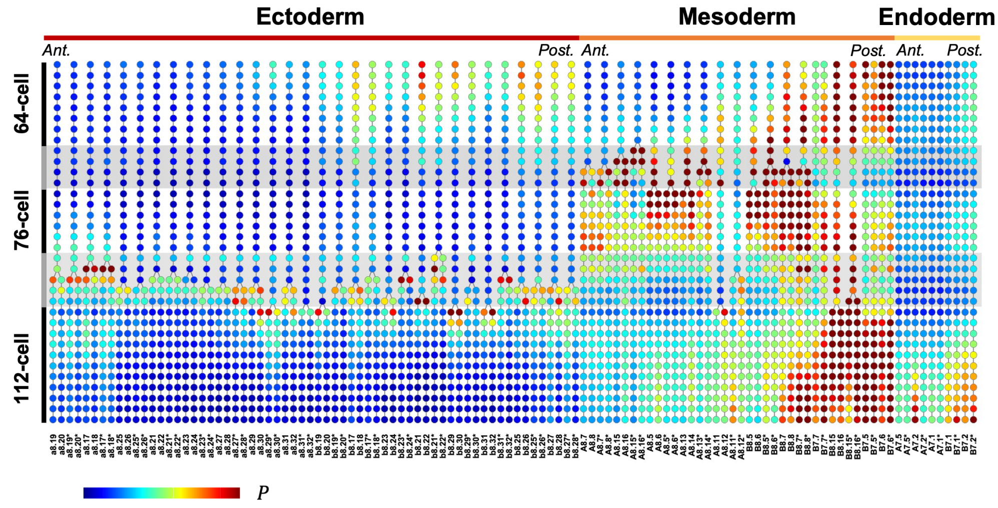

Figure 3.15. Lineage map of pressures in ascidian gastrulation

The lineage view of the mechanical data does also make manifest both cell-cycle dependent and independent patterns. Both the pressure and apical stress data reveals two phases of mechanical activity. A first, coupled to the wave of divisions in the mesoderm that transforms the embryo from the 64- to 76-cell stage, and a second wave within the 112-cell stage that appears decoupled from the cell cycle. The first phase of mechanical activity is initiated by the division of a mother cell, transiently retaining high pressures in the daughters, eventually dissipating just before the division of ectodermal cells. Both single-cell and tissue-based studies of cell divisions suggest a transient alteration in the local mechanical environment, and it is reassuring that our mechanical atlas makes manifest this anticipated feature.

The second phase of mechanical activity appears independent of any wave of cell divisions in the embryo, and is when the embryo begins to significantly alter its morphology. It is at this phase that clear anterior-posterior and animal-vegetal asymmetries in the mechanical atlas are manifest. Integrating all this data and distilling a mechanical logic is made challenging by the empirical observation that since the system is arguably close to a static equilibrium at all times the outward pushing cell pressures and contracting membrane and line elements must be in balance. Thus, the correlations apparent within the lineage maps between, say, cell pressures and apical stresses are both anticipated and confounding. Fortunately, our present theory of mechanics suggests a principled approach to integrating this complex data so as to reveal the independent mechanical features at a cell-by-cell basis.

3.4. Mechanical flexibility in ascidian embryogenesis

Although we have shown many known and novel patterns in mechanical atlas and lineage maps, it is still not clear whether those patterns is conserved with respect to the mechanical zero-modes. In order to investigate the mechanical flexibility, we introduce the concept of cellular stress tensor that represents regional average stress (3.4.1). In this point of view, the spatial patterns of contractile stresses are invariant with respect to the third zero-mode (3.4.2). The cellular stress tensor also allows us to investigate the patterns of shear forces and figure out the flexibility (3.4.3). We also discussed the temporal flexibility with respect to the second zero-modes that corresponds to the mechanical scales (3.4.4).

3.4.1. Cellular stress tensor

Elementally, different values of mechanical inputs can balance at the same geometry; globally, the total expansive stresses and contractile stresses must sum to zero in spite of the choice of zero mode. Here we introduce the concept of cellular stress tensor to show the invariance of stress under zero-modes. Inside cells, the cell volume is under an isotropic 3D pushing stress tensor $\boldsymbol{\sigma}_V = P_\alpha \boldsymbol{I}_3$ (where $\boldsymbol{I}_3$ denotes the identical matrix), which is sourced by the pressure we measure. Over a membrane, surface tension cause an in-plane isotropic pulling stress tensor $\boldsymbol{\sigma}_S = -T_{\alpha\beta}\boldsymbol{I}_2$ (where $\boldsymbol{I}_2$ is in-plane projection of identical matrix). Along each edge, line tension generate a tangential pulling stress tensor $\boldsymbol{\sigma}_L = -F_{\alpha\beta\gamma}\boldsymbol{I}_1$ (where $\boldsymbol{I}_1$ is one-dimensional projection of identical matrix). Accounting for all of these, the average stress over a region of volume V is

$$\bar{\boldsymbol{\sigma}} = \left[\sum_{\alpha}\int P_\alpha \boldsymbol{I}_3 dV - \sum_{\alpha\beta}\int T_{\alpha\beta}\boldsymbol{I}_2 dA - \sum_{\alpha\beta\gamma}\int F_{\alpha\beta\gamma}\boldsymbol{I}_1 dL\right]/V. \tag{3.1}$$

For convenience, we pick the animal-vegetal (AV), left-right (LR) and anterior-posterior (AP) axes as our orthogonal 3D coordinate system. One of the principle consequences is that the average stress over the entire embryo must be zero according to Newton's third law. This result can be verified by the numerical computations.

For any single cell, we can integrate all the data within it, and on its membrane surfaces and junctional edges into a single 3 × 3 cell-based tensor, which is denoted as cellular stress tensor:

$$\boldsymbol{\sigma}_\alpha = \left[P_\alpha V_\alpha - \sum_{\alpha\beta}\frac{1}{2}\int T_{\alpha\beta}\boldsymbol{I}_2 dA - \sum_{\alpha\beta\gamma}\frac{1}{3}\int F_{\alpha\beta\gamma}\boldsymbol{I}_1 dL\right]/V_\alpha. \tag{3.2}$$

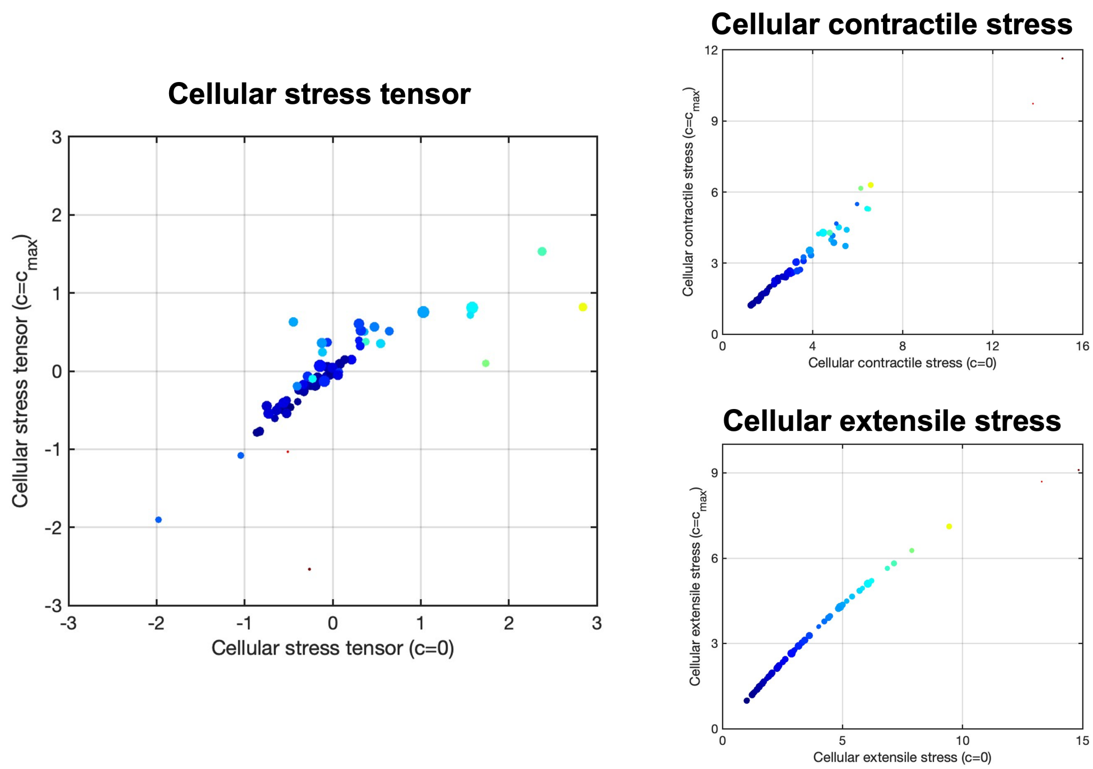

Figure 3.16. Cellular stress tensor

Note that one membrane stress is shared by two cells and one line stress is shared by three cells. This tensor is symmetric by construction, and the scaling by the volume of the cell ensures that the tensor itself is an intensive quantity, whose magnitude is independent of the size of the system.

We then investigate how the pattern of cellular stress tensors is affected by zero-mode parameter c. In Figure 3.16, the numerical comparison shows that for high and low values of c, the trace of cellular stress tensors are highly correlate. This invariance implies that the flexibility of cells generating overall stresses.

3.4.2. Flexibility in contractile stress

We then consider the contractile stresses with respect to membranes. Since the surface tensions and line tensions provide contractile forces to the multicellular system, we could compute the total contractile stress over a membrane:

$$\boldsymbol{\sigma}_{\alpha\beta} = \left[\int T_{\alpha\beta}\boldsymbol{I}_2 dA + \sum_{\gamma}\frac{1}{3}\int F_{\alpha\beta\gamma}\boldsymbol{I}_1 dL\right]/A_{\alpha}. \tag{3.3}$$

Note that the line stress is sheared by three membranes. In Figure 3.17, it shows the different patterns of surface tensions and line tensions with respect to the zero-mode parameter c at 76-cell stage of ascidian embyro. However, computing the contractile stress tensors, as shown in Figure 3.17, the spatial patterns are invariant with respect to the mechanical zero mode.

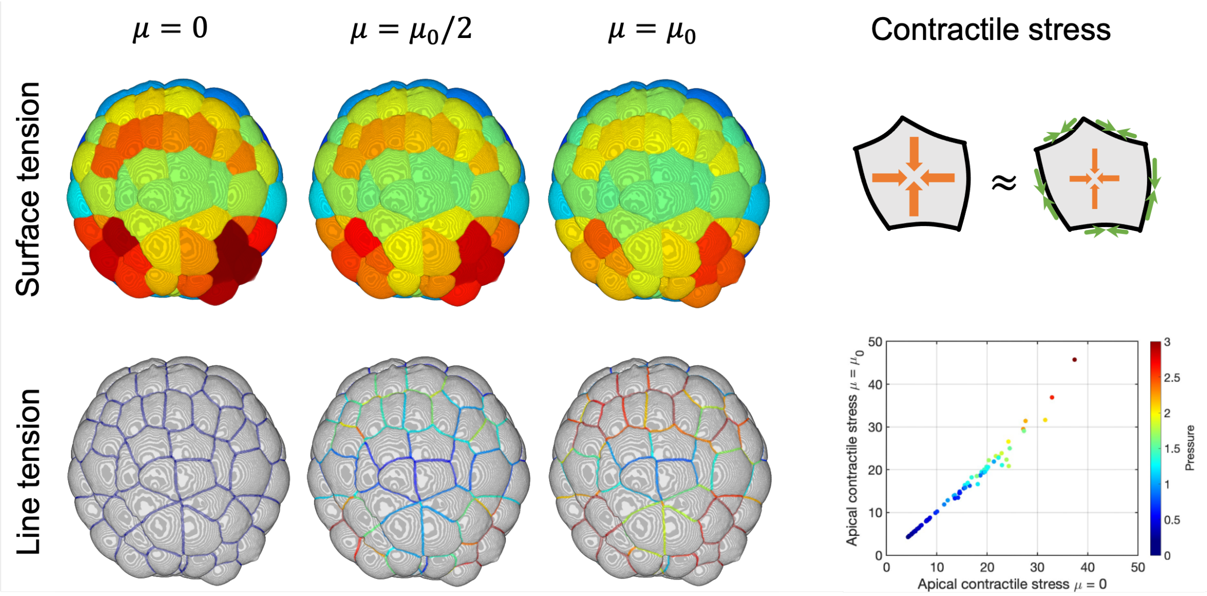
$\mu = 0$
$\mu = \mu_0/2$
$\mu = \mu_0$
Contractile stress
Surface tension
Line tension
≈
Apical contractile stress $\mu = \mu_0$
0
10
20
30
40
50
Apical contractile stress $\mu = 0$
0
10
20
30
40
50
Pressure
0
0.5
1
1.5
2
2.5
3

Figure 3.17. Flexibility in contractile stress

The invariance of the contractile stresses provide another mechanical flexibility to the multicellular system. The ascidian cells are able to allocate the force generation on edges and membranes, without affecting the regional contractile and global balance. In fact, this flexibility is observed in the molecular measurements of ascidian gastrulation. According to Sherrard et al. [**32**], at the early 112-cell stage, myosin motors are reallocated from membrane cortices to the junctions, for the purpose of maintaining the apical contractility.

3.4.3. Flexibility in shear stress

Cellular and membrane stress tensor give us the quantitative tools of understanding mechanical flexibility. Perhaps more importantly, constructing a principled quantity such as the cell-based stress tensor allows for the correct conglomeration of the, geometry-dependent, membrane and junctional tensions that can produce shear stresses on the cell. A simple way to see these patterns is to decompose the stress tensor, per cell, into its hydrostatic and deviatoric (its traceless part, which causes shape change) components. The second characteristic of the deviatoric matrix, J_2, is related to a scalar quantity termed the von Mises Stress, $\sigma_{VM} = \sqrt{3J_2}$, which is a cell-based scalar measure of the extent of shear stresses in the system. Computationally, for a stress tensor $\boldsymbol{\sigma}$,

$$J_2 = \frac{1}{2}tr(\boldsymbol{\sigma}^2) - \frac{1}{6}tr(\boldsymbol{\sigma})^2. \tag{3.4}$$

We heatmap the variation of σ_{VM} on the lineage diagram of the embryo, and present its spatial patterns from an animal and vegetal view at the 112-cell stage stage in Figure 3.18. The pattern of the von Mises stress in Figure 3.18 are manifestly distinct from either of the patterns seen in Figure 3.15. This is naturally expected since the pressure

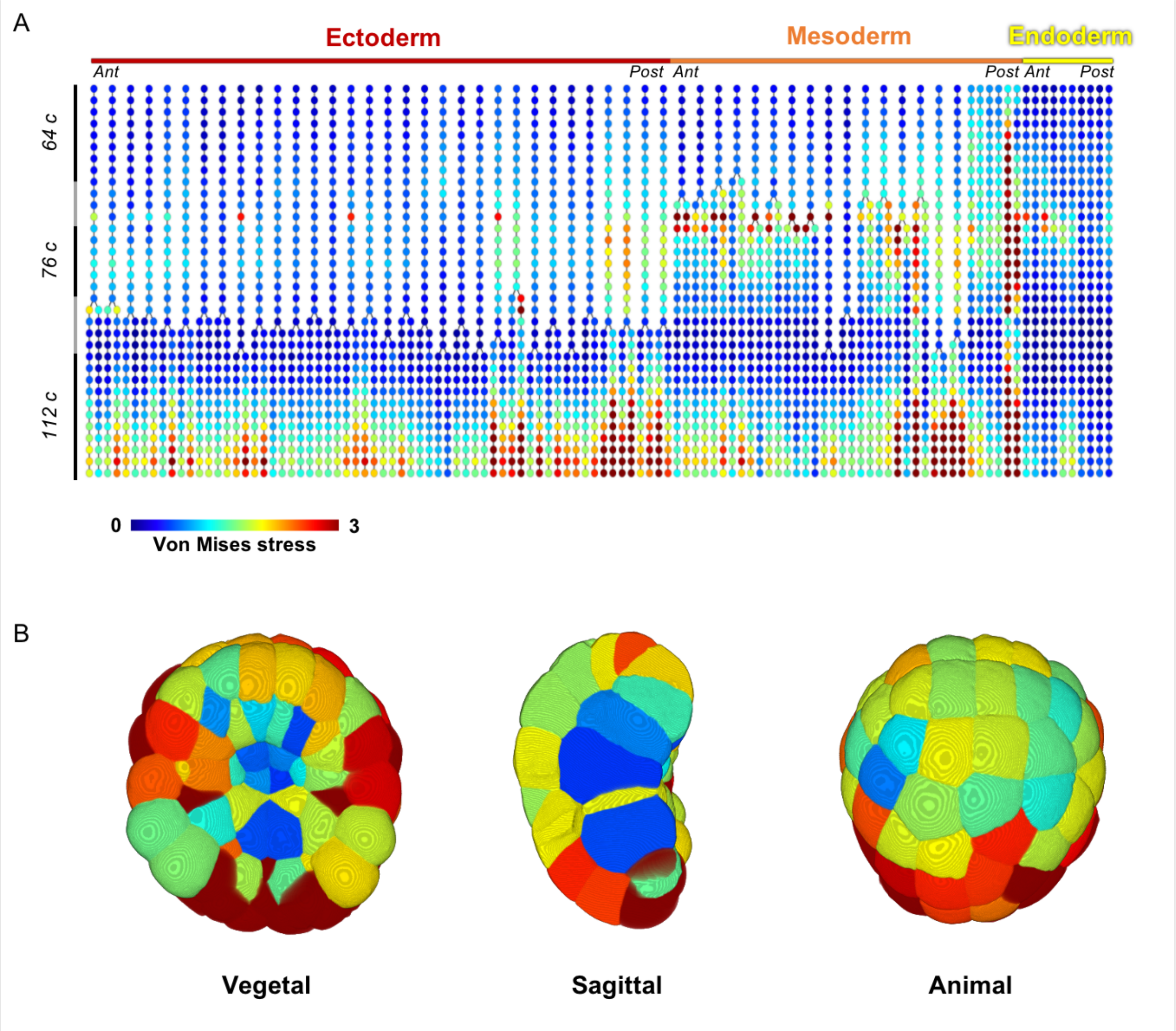

Figure 3.18. Von Mises shear stress

(hydrostatic) and deviatoric contributions to overall stress are independent. Contrasting previously observed patterns, ectodermal cells experience shear stress. To gain a more physical sense of the pattern we visualize the von Mises stress on the embryo in Figure 3.18. One can clearly observe patterns, including the high levels of von Mises stress in the posterior mesodermal lineage.

3.4.4. Flexibility in temporal patterns

The adiabatic nature of ascidian embryogenesis physically provides the flexibility of temporal regulations with respect to mechanical scale. For example, the curvature of a membrane can be produced by either increasing the cellular pressure in one side or decreasing the cellular pressure in the other side. Such phenomenon is presented in the lineage maps by the choice of the zero-mode parameter b. In order to determine this scale factor, we have to add another assumption of conservation in the system. In the current lineage maps shown in Figure 3.15, we suppose the total hydrostatic energy of cell volume to be conserved:

$$E = \sum_{\alpha} P_\alpha V_\alpha = const. \tag{3.5}$$

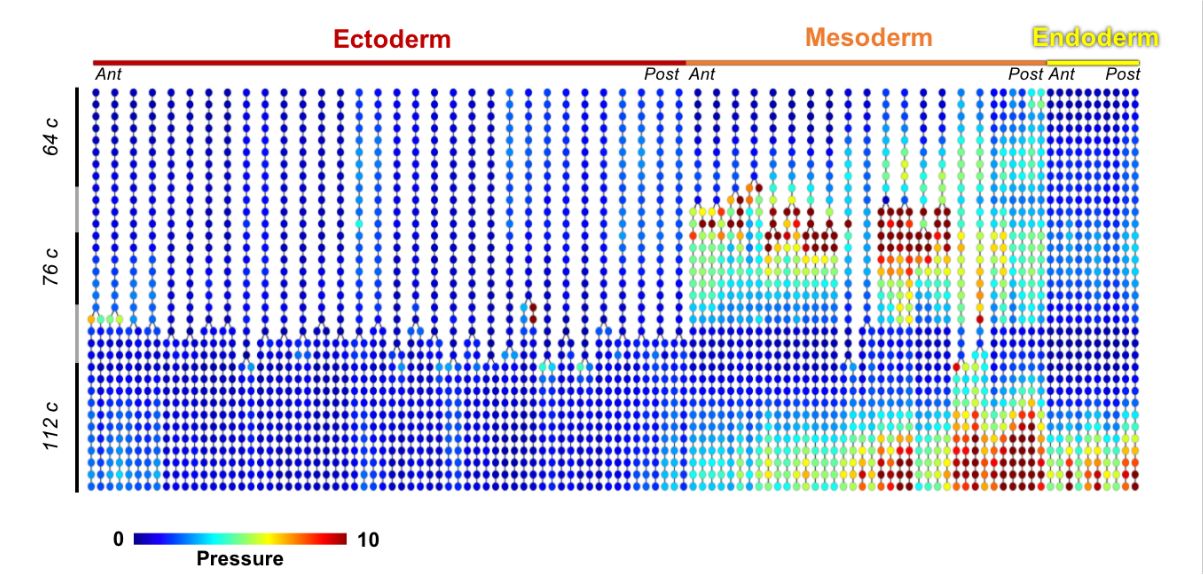

Figure 3.19. Lineage map of pressures relative to ectoderm

In the similar way, we can assume the conservation of total elastic energy, or the conservation of total contractile energy. The another types of scale determination based on the biological assumptions. For example, in Figure 3.19, we assume the inactivity of the ectodermal cells over time and the mechanical values of the active cells is relative to the average pressure of ectoderm. Consequently, additional physical measurement needs to be implemented to determine the scale factors, in order for the mechanical inference of a dynamical system.

3.5. Conclusion

In this chapter, we apply the force inference method on the gastrulation process of ascidian embryo, and then analyze the fitting results and the mechanical patterns. For the first time in this field, we construct the three dimensional mechanical atlas that will broad the view angles for embryogenesis. The consequences provide the important perspectives to both the physics of the shape regulation and the biological design principles of embryo.

- The precision of the geometry fittings, the reproducibility across embryos and the reconstruction of symmetric and asymmetric mechanical patterns give the confidence for the accuracy of the force inference scheme. We could apply this force inference scheme to other model organisms, in order to understand more general mechanical principles.
- The fitting error distributions in both space and time further confirm the low-dimensionality representation of embryo geometry. It will benefit the studies that investigate the developmental trajectories in three dimensions by the simplification of the geometric description.

- The symmetries and asymmetries patterns of mechanics offers another evidence for the axis establishment in the ascidian body plan. Collaborating with the genetic evidence and chemical evidence, deeper understanding of this fundamental regulatory will be possible.
- The pressure heterogeneities corresponding to the germ layers implies the different genetic regulations for force generation by zygotic genes. This biological insight will inspire ascidian geneticists to hypothesize and experiment on mutant embryos. It will further inspire the biomedical scientists who work on genetic engineering.
- The mechanical activity in the ring of mesodermal cells during gastrulation provides a novel physical insight on invagination. For some morphological or physiological process, the tissue around the invaginating region is likely to be stiff, so that the cell movements are able to happen on a rigid framework.
- The correlations between tensions and pressures imply the underlying biophysical principles that the co-regulation of cortical dynamics and hydrostatic states.
- The mechanical flexibility in both spatial and temporal aspects resolves the questions from previous observations of molecular reallocation.

CHAPTER 4

Anisotropic Model for Three-dimensional Cellular Aggregate

4.1. Background

In previous chapters, we construct the force inference method and apply it onto ascidian image data. However, in the models, we only consider the isotropic stresses, especially we assume the membrane surface tension to be isotropic. However, there is increasingly more experiment evidences that the cytoskelekon forms anisotropic cortical networks along the membrane faces. Some of the studies shows the importance of such anisotropy in certain developmental progresses [**34**]. Therefore, we are motivated to generalize the model, considering the anisotropic effect in the three-dimensional cellular aggregates.

Although the anisotropic effects of mechanical stress are discovered in many morphological processes, few mathematical models are established to quantitatively investigate how embryo operate the effects collectively. Even in the physics points of view, it is not fully comprehended how the anisotropic surface tension could balance with pressure difference. In our model, the simplicity in geometry partly comes from the isotropic assumption, so the anisotropic effects is apparently cause complexity in the geometric representation of the cellular aggregates.

Here in this chapter, we incorporate the anisotropic surface tensions into the mechanical model. To be simple, we focus on the scenario that only surface tensions and pressures equipped in the system, but no line tensions on the junctional edges. We get some primary consequences from this model, and discuss the idea of force inference for simple biology examples.

4.2. Anisotropic tension balance on Polyhedral tessellation

In order to investigate anisotropic force balance in a cellular aggregate, we start from the special case that there is no pressure difference but only anisotropic surface tensions. In this multi-cellular system under equilibrium, the geometry is Polyhedral tessellation which we have already parameterized and understood the intrinsic constraints.

We first take a look at the effects of anisotropic surface tension on membranes and edges (4.2.1). Then we take use of the dual graph and introduce the membrane anisotropy to simplify the force parameters (4.2.2). We analyze the relations among these membrane anisotropies within a single cell (4.2.3) and in cellular aggregate (4.2.4). Consequently, we discover the simplicity of anisotropic tension solutions in this complex mechanical system of equilibrium (4.2.5).

4.2.1. Anisotropic surface tension

An anisotropic surface tension is an in-plane symmetric stress tensor. For a flat polygonal membrane face $M_{\alpha\beta}$, suppose $(\hat{\boldsymbol{\imath}}, \hat{\boldsymbol{\jmath}}, \hat{\boldsymbol{k}})$ are three orthogonal unit vectors, where $\hat{\boldsymbol{\imath}}$ and $\hat{\boldsymbol{\jmath}}$ are in-plane vectors and $\hat{\boldsymbol{k}}$ is the face normal. The anisotropic tension $\boldsymbol{T}_{\alpha\beta}$ can be expressed as

$$\boldsymbol{T}_{\alpha\beta} = \sigma_1 \hat{\boldsymbol{\imath}} \otimes \hat{\boldsymbol{\imath}} + \tau \hat{\boldsymbol{\imath}} \otimes \hat{\boldsymbol{\jmath}} + \tau \hat{\boldsymbol{\jmath}} \otimes \hat{\boldsymbol{\imath}} + \sigma_2 \hat{\boldsymbol{\jmath}} \otimes \hat{\boldsymbol{\jmath}}. \tag{4.1}$$

Or we can use the eigenvalues $\sigma^{(1)}, \sigma^{(2)}$ and eigenvectors $\hat{\boldsymbol{e}}_1, \hat{\boldsymbol{e}}_2$ to write as

$$\boldsymbol{T}_{\alpha\beta} = \sigma^{(1)}\hat{\boldsymbol{e}}_1 \otimes \hat{\boldsymbol{e}}_1 + \sigma^{(2)}\hat{\boldsymbol{e}}_2 \otimes \hat{\boldsymbol{e}}_2. \tag{4.2}$$

On an edge of the polygonal membrane, suppose the tangent is $\hat{\boldsymbol{t}}$ and the in-plane normal is $\hat{\boldsymbol{n}}$, as shown in Figure 4.1. Then the traction force applied on this edge by surface tension is

$$\boldsymbol{F} = \boldsymbol{T}_{\alpha\beta} \cdot \hat{\boldsymbol{n}}. \tag{4.3}$$

Since the surface tension is anisotropic, this traction force is not guaranteed to be perpendicular to the edge as in previous chapters. Specifically, the traction forces in normal direction and tangential direction are

$$\begin{aligned} F^{(n)} &= \boldsymbol{F} \cdot \hat{\boldsymbol{n}} = \boldsymbol{T}_{\alpha\beta} : (\hat{\boldsymbol{n}} \otimes \hat{\boldsymbol{n}}), \\ F^{(t)} &= \boldsymbol{F} \cdot \hat{\boldsymbol{t}} = \boldsymbol{T}_{\alpha\beta} : (\hat{\boldsymbol{n}} \otimes \hat{\boldsymbol{t}}). \end{aligned} \tag{4.4}$$

As shown in Figure 4.1, a surface tension applies different normal traction forces on different edges, which is between the eigenvalues of $\boldsymbol{T}_{\alpha\beta}$. And the shear force $F^{(t)}$ is not zero on the edge.

Consider the anisotropic tension balance at the edge $E_{\alpha\beta\gamma}$, now it is more complex than isotropic scenario. As shown in Figure 4.1, let us denote the three in-plane normal directions as $\hat{\boldsymbol{n}}_{\alpha\beta,\gamma}$, $\hat{\boldsymbol{n}}_{\beta\gamma,\alpha}$ and $\hat{\boldsymbol{n}}_{\gamma\alpha,\beta}$. So the balance relation between three traction forces is

$$\boldsymbol{T}_{\alpha\beta} \cdot \hat{\boldsymbol{n}}_{\alpha\beta,\gamma} + \boldsymbol{T}_{\beta\gamma} \cdot \hat{\boldsymbol{n}}_{\beta\gamma,\alpha} + \boldsymbol{T}_{\gamma\alpha} \cdot \hat{\boldsymbol{n}}_{\gamma\alpha,\beta} = \boldsymbol{0}. \tag{4.5}$$

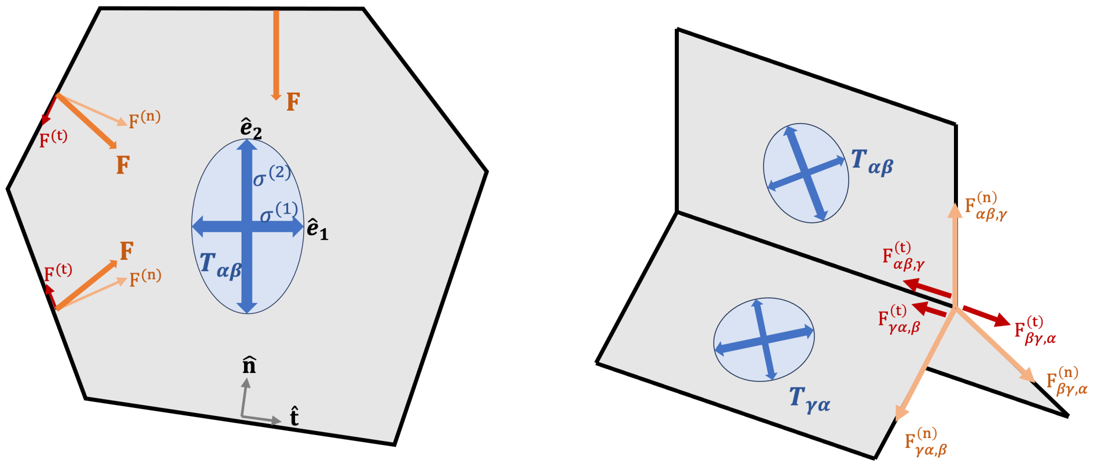
F
$F^{(n)}$
$F^{(t)}$
F
$\hat{e}_2$
$\sigma^{(2)}$
$\sigma^{(1)}$
$\hat{e}_1$
$T_{\alpha\beta}$
F
$F^{(t)}$
$F^{(n)}$
$\hat{n}$
$\hat{t}$
$T_{\alpha\beta}$
$F^{(n)}_{\alpha\beta,\gamma}$
$F^{(t)}_{\alpha\beta,\gamma}$
$F^{(t)}_{\gamma\alpha,\beta}$
$F^{(t)}_{\beta\gamma,\alpha}$
$F^{(n)}_{\beta\gamma,\alpha}$
$T_{\gamma\alpha}$
$F^{(n)}_{\gamma\alpha,\beta}$

Figure 4.1. Anisotropic surface tension

It can be decomposed into the normal force balance

$$F^{(n)}_{\alpha\beta,\gamma}\hat{\boldsymbol{n}}_{\alpha\beta,\gamma} + F^{(n)}_{\beta\gamma,\alpha}\hat{\boldsymbol{n}}_{\beta\gamma,\alpha} + F^{(n)}_{\gamma\alpha,\beta}\hat{\boldsymbol{n}}_{\gamma\alpha,\beta} = \mathbf{0} \tag{4.6}$$

and shear force balance

$$F^{(t)}_{\alpha\beta,\gamma} + F^{(t)}_{\beta\gamma,\alpha} + F^{(t)}_{\gamma\alpha,\beta} = 0. \tag{4.7}$$

The balance is illustrate in Figure 4.1.

For a cellular aggregate in equilibrium, the force inference problem is: can we infer the anisotropic surface tensions from given the geometric parameters of Polyhedral tessellation? In this problem, the total number of unknowns are $3N_F$ because each surface tension $\boldsymbol{T}_{\alpha\beta}$ need three values σ_1, σ_2, τ to be defined. The total number of balance equations is $3N_E$. Fortunately, the dual graph of Polyhedral tessellation is still useful for this scenario.

We will demonstrate in the following sections that there exist analytical solutions to this inverse problem.

4.2.2. Membrane anisotropy tensor

We know that the dimensionality of Polyhedral tessellation is $4N_C$, which can be parameterized by Weighted Voronoi $\{\boldsymbol{q}_\alpha, \theta_\alpha\}_{\alpha=1,2,\ldots,N_C}$. For isotropic surface tension balance on an edge $E_{\alpha\beta\gamma}$, using the divergence theorem on the dual triangle, we get the solutions of tension $T_{\alpha\beta}$ are proportional to $q_{\alpha\beta}$. In the solution $T_{\alpha\beta} = b * q_{\alpha\beta}$, the free parameter b is a global constant.

Although in anisotropic scenario the dual triangle cannot directly relate to the traction force balance (4.5), it relates to the composition of normal force balance (4.6). Therefore, the solution to this normal equation is

$$\begin{aligned} F^{(n)}_{\alpha\beta,\gamma} &= b_{\alpha\beta\gamma} * q_{\alpha\beta}, \\ F^{(n)}_{\beta\gamma,\alpha} &= b_{\alpha\beta\gamma} * q_{\beta\gamma}, \\ F^{(n)}_{\gamma\alpha,\beta} &= b_{\alpha\beta\gamma} * q_{\gamma\alpha}. \end{aligned} \tag{4.8}$$

Here $b_{\alpha\beta\gamma}$ is the coefficient for edge $E_{\alpha\beta\gamma}$. Because an anisotropic surface tension applies different normal traction force on different edges, the coefficient is also different for different edges. However, these coefficients $b_{\alpha\beta\gamma}$ of edges for one membrane $M_{\alpha\beta}$ is related. Given an in-plane tensor $\boldsymbol{B}_{\alpha\beta}$, the coefficient can be given as

$$b_{\alpha\beta\gamma} = \boldsymbol{B}_{\alpha\beta} : (\hat{\boldsymbol{n}}_{\alpha\beta,\gamma} \otimes \hat{\boldsymbol{n}}_{\alpha\beta,\gamma}). \tag{4.9}$$

We call this tensor $\boldsymbol{B}_{\alpha\beta}$ as membrane anisotropy tensor (MAT). The relation of surface tension and MAT is given as

$$\boldsymbol{T}_{\alpha\beta} = q_{\alpha\beta}\boldsymbol{B}_{\alpha\beta}. \tag{4.10}$$

Therefore, the mechanical inverse problem becomes solving MAT $\boldsymbol{B}_{\alpha\beta}$ for each membrane under the equations

$$\boldsymbol{B}_{\alpha\beta} : (\hat{\boldsymbol{n}}_{\alpha\beta,\gamma} \otimes \hat{\boldsymbol{n}}_{\alpha\beta,\gamma}) = \boldsymbol{B}_{\beta\gamma} : (\hat{\boldsymbol{n}}_{\beta\gamma,\alpha} \otimes \hat{\boldsymbol{n}}_{\beta\gamma,\alpha}) = \boldsymbol{B}_{\gamma\alpha} : (\hat{\boldsymbol{n}}_{\gamma\alpha,\beta} \otimes \hat{\boldsymbol{n}}_{\gamma\alpha,\beta}) \tag{4.11}$$

for each edge $E_{\alpha\beta\gamma}$. Actually, the coefficient equivalence (4.11) is another version of normal force balance (4.6). As for the shear force balance (4.7), it can be given as

$$q_{\alpha\beta}\boldsymbol{B}_{\alpha\beta} : (\hat{\boldsymbol{n}}_{\alpha\beta,\gamma} \otimes \hat{\boldsymbol{t}}_{\alpha\beta,\gamma}) + q_{\beta\gamma}\boldsymbol{B}_{\beta\gamma} : (\hat{\boldsymbol{n}}_{\beta\gamma,\alpha} \otimes \hat{\boldsymbol{t}}_{\beta\gamma,\alpha}) + q_{\gamma\alpha}\boldsymbol{B}_{\gamma\alpha} : (\hat{\boldsymbol{n}}_{\gamma\alpha,\beta} \otimes \hat{\boldsymbol{t}}_{\gamma\alpha,\beta}) = 0 \tag{4.12}$$

4.2.3. Cellular anisotropy tensor

Now let us consider the MATs $\boldsymbol{B}_{\alpha\beta}$ on a single polyhedral cell α as shown in figure. We can count the degrees of freedom of these MATs under the coefficient equivalence (4.11) on one polyhedron.

Claim: The MATs under the coefficient equivalence $\boldsymbol{B}_{\alpha\beta} : (\hat{\boldsymbol{n}}_{\alpha\beta,\gamma} \otimes \hat{\boldsymbol{n}}_{\alpha\beta,\gamma}) = \boldsymbol{B}_{\gamma\alpha} : (\hat{\boldsymbol{n}}_{\gamma\alpha,\beta} \otimes \hat{\boldsymbol{n}}_{\gamma\alpha,\beta})$ on one polyhedron α have 6 degrees of freedom.

Proof: Suppose the polyhedron have $n_F^{(\alpha)}$ faces, $n_E^{(\alpha)}$ edges and $n_V^{(\alpha)}$ vertices. We know the Euler's rule is $n_F^{(\alpha)} + n_V^{(\alpha)} - n_E^{(\alpha)} = 2$, and each vertex has three edges in a polygon

$3n_V^{(\alpha)} = 2n_E^{(\alpha)}$. From the two relations we get

$$n_E^{(\alpha)} = 3n_F^{(\alpha)} - 6. \tag{4.13}$$

Each MAT has 3 degrees of freedom, thus in total there are $3n_F^{(\alpha)}$ degrees of freedom. For each edge there is 1 relation, thus there are in total $n_E^{(\alpha)}$ constraints to $3n_F^{(\alpha)}$ parameters. Therefore, for one polyhedron, the MATs have $3n_F^{(\alpha)} - n_E^{(\alpha)} = 6$ degrees of freedom. $\square$

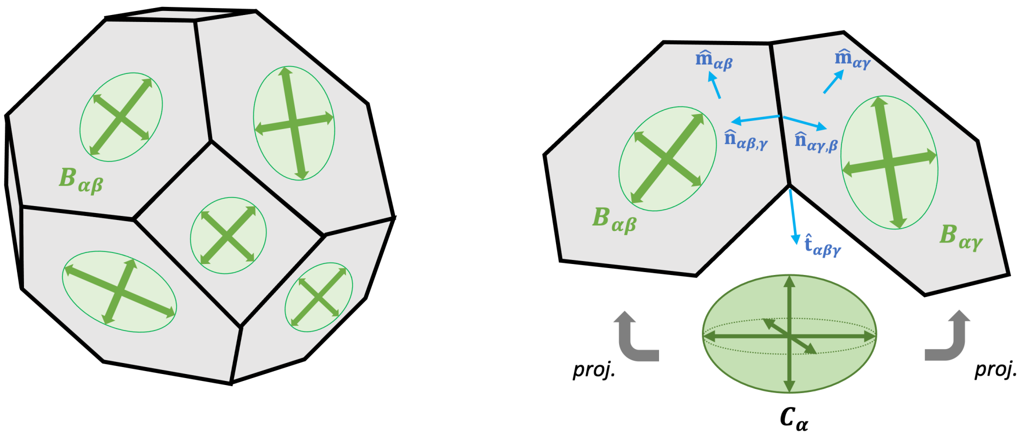
$B_{\alpha\beta}$
$\hat{\mathbf{m}}_{\alpha\beta}$
$\hat{\mathbf{m}}_{\alpha\gamma}$
$\hat{\mathbf{n}}_{\alpha\beta,\gamma}$
$\hat{\mathbf{n}}_{\alpha\gamma,\beta}$
$B_{\alpha\beta}$
$\hat{\mathbf{t}}_{\alpha\beta\gamma}$
$B_{\alpha\gamma}$
proj.
proj.
C_α

Figure 4.2. Membrane anisotropy and cellular anisotropy tensors

We know that a three-dimensional symmetric tensor has 6 degrees of freedom. So we hypothesis that there exists a tensor $\boldsymbol{C}_\alpha$ for a polyhedral cell α, such that each MAT $\boldsymbol{B}_{\alpha\beta}$ is a certain 'projection' of $\boldsymbol{C}_\alpha$ to the face $M_{\alpha\beta}$. By analyzing some special cases, we guess out and prove the projecting operations as the following claim.

Claim: If we project a three-dimensional symmetric tensor $\boldsymbol{C}_\alpha$ to each face in a polyhedron as

$$\boldsymbol{B}_{\alpha\beta} = -\hat{\boldsymbol{m}}_{\alpha\beta} \times \boldsymbol{C}_\alpha \times \hat{\boldsymbol{m}}_{\alpha\beta}, \tag{4.14}$$

then these projected tensors $\boldsymbol{B}_{\alpha\beta}$ satisfy the coefficient equivalence $\boldsymbol{B}_{\alpha\beta} : (\hat{\boldsymbol{n}}_{\alpha\beta,\gamma} \otimes \hat{\boldsymbol{n}}_{\alpha\beta,\gamma}) = \boldsymbol{B}_{\gamma\alpha} : (\hat{\boldsymbol{n}}_{\gamma\alpha,\beta} \otimes \hat{\boldsymbol{n}}_{\gamma\alpha,\beta})$. Here $\hat{\boldsymbol{m}}_{\alpha\beta}$ denotes the face normal.

Proof: As shown in Figure 4.2, using the relation $\hat{\boldsymbol{m}}_{\alpha\beta} \times \hat{\boldsymbol{n}}_{\alpha\beta,\gamma} = \hat{\boldsymbol{t}}_{\alpha\beta\gamma}$, we can simplify the left-hand-side coefficient as

$$\begin{aligned}
\boldsymbol{B}_{\alpha\beta} : (\hat{\boldsymbol{n}}_{\alpha\beta,\gamma} \otimes \hat{\boldsymbol{n}}_{\alpha\beta,\gamma}) &= -((\hat{\boldsymbol{m}}_{\alpha\beta} \times \boldsymbol{C}_\alpha) \times \hat{\boldsymbol{m}}_{\alpha\beta} \cdot \hat{\boldsymbol{n}}_{\alpha\beta,\gamma}) \cdot \hat{\boldsymbol{n}}_{\alpha\beta,\gamma} \\
&= -((\hat{\boldsymbol{m}}_{\alpha\beta} \times \hat{\boldsymbol{n}}_{\alpha\beta,\gamma}) \cdot (\hat{\boldsymbol{m}}_{\alpha\beta} \times \boldsymbol{C}_\alpha)) \cdot \hat{\boldsymbol{n}}_{\alpha\beta,\gamma} \\
&= -\hat{\boldsymbol{t}}_{\alpha\beta\gamma} \cdot ((\hat{\boldsymbol{m}}_{\alpha\beta} \times \boldsymbol{C}_\alpha) \cdot \hat{\boldsymbol{n}}_{\alpha\beta,\gamma}) \\
&= \hat{\boldsymbol{t}}_{\alpha\beta\gamma} \cdot ((\hat{\boldsymbol{m}}_{\alpha\beta} \times \hat{\boldsymbol{n}}_{\alpha\beta,\gamma}) \cdot \boldsymbol{C}_\alpha) \\
&= \boldsymbol{C}_\alpha : (\hat{\boldsymbol{t}}_{\alpha\beta\gamma} \otimes \hat{\boldsymbol{t}}_{\alpha\beta\gamma}).
\end{aligned} \tag{4.15}$$

In the similar way, we can derive the right-hand-side coefficient as $\boldsymbol{B}_{\gamma\alpha} : (\hat{\boldsymbol{n}}_{\gamma\alpha,\beta} \otimes \hat{\boldsymbol{n}}_{\gamma\alpha,\beta}) = \boldsymbol{C}_\alpha : (\hat{\boldsymbol{t}}_{\alpha\beta\gamma} \otimes \hat{\boldsymbol{t}}_{\alpha\beta\gamma})$, which is equal to left-hand-side. □

Therefore, we confirm the hypothesis that each MAT of a polyhedron α can be expressed as the projection of a tensor $\boldsymbol{C}_\alpha$. We call the tensor $\boldsymbol{C}_\alpha$ as cellular anisotropy tensor (CAT).

4.2.4. Global anisotropy tensor of cellular aggregate

We then consider the Polyhedral tessellation and investigate the relations among the CATs of all cells. For any MAT $\boldsymbol{B}_{\alpha\beta}$, it is both a projection of $\boldsymbol{C}_\alpha$ and a projection of $\boldsymbol{C}_\beta$. So for any adjacent cell pair α and β, there is

$$\hat{\boldsymbol{m}}_{\alpha\beta} \times \boldsymbol{C}_\alpha \times \hat{\boldsymbol{m}}_{\alpha\beta} = \hat{\boldsymbol{m}}_{\alpha\beta} \times \boldsymbol{C}_\beta \times \hat{\boldsymbol{m}}_{\alpha\beta}. \tag{4.16}$$

Additional to this, we also have the shear force balance equations (4.7), in which $\boldsymbol{B}_{\alpha\beta}$ can be substituted by $\boldsymbol{C}_\alpha$ terms. As shown in Figure 4.3, at a vertex $\boldsymbol{r}_{\alpha\beta\gamma\delta}$ formed by four cells, we have construct the relations between the four CATs.

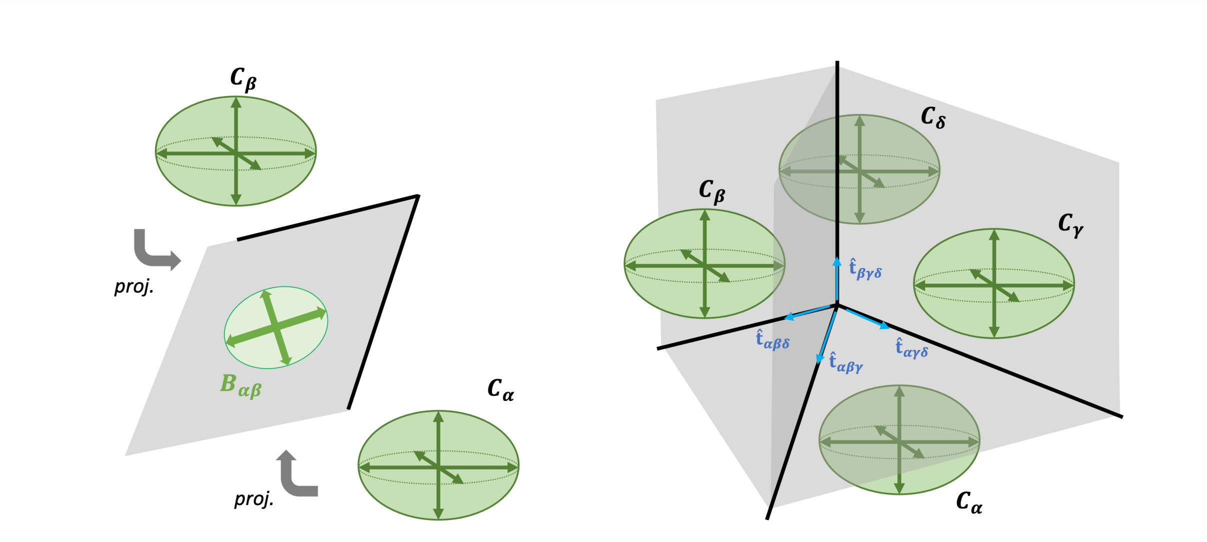
C_β
proj.
$B_{\alpha\beta}$
C_α
proj.
C_δ
C_β
C_γ
$\hat{t}_{\beta\gamma\delta}$
$\hat{t}_{\alpha\beta\delta}$
$\hat{t}_{\alpha\beta\gamma}$
$\hat{t}_{\alpha\gamma\delta}$
C_α

Figure 4.3. Global anisotropy tensor of cellular aggregate

Claim: For a vertex $\boldsymbol{r}_{\alpha\beta\gamma\delta}$, the four CATs $\boldsymbol{C}_\alpha, \boldsymbol{C}_\beta, \boldsymbol{C}_\gamma, \boldsymbol{C}_\delta$ satisfying the projection equivalence (4.16) and shear force balance (4.7) implies

$$\boldsymbol{C}_\alpha = \boldsymbol{C}_\beta = \boldsymbol{C}_\gamma = \boldsymbol{C}_\delta. \tag{4.17}$$

Lemma: The degrees of freedom for these four CATs is 6.

Proof of Lemma: Each CAT has 6 degrees of freedom, thus there are 24 degrees of freedom in total. Then consider the constraints on these degrees. Each equation (4.16) provides three constraints, which can be written equivalently as

$$\begin{aligned}
\boldsymbol{C}_\alpha : (\hat{\boldsymbol{t}}_{\alpha\beta\gamma} \otimes \hat{\boldsymbol{t}}_{\alpha\beta\gamma}) &= \boldsymbol{C}_\beta : (\hat{\boldsymbol{t}}_{\alpha\beta\gamma} \otimes \hat{\boldsymbol{t}}_{\alpha\beta\gamma}),\\
\boldsymbol{C}_\alpha : (\hat{\boldsymbol{t}}_{\alpha\beta\delta} \otimes \hat{\boldsymbol{t}}_{\alpha\beta\delta}) &= \boldsymbol{C}_\beta : (\hat{\boldsymbol{t}}_{\alpha\beta\delta} \otimes \hat{\boldsymbol{t}}_{\alpha\beta\delta}),\\
\boldsymbol{C}_\alpha : (\hat{\boldsymbol{t}}_{\alpha\beta\gamma} \otimes \hat{\boldsymbol{t}}_{\alpha\beta\delta}) &= \boldsymbol{C}_\beta : (\hat{\boldsymbol{t}}_{\alpha\beta\gamma} \otimes \hat{\boldsymbol{t}}_{\alpha\beta\delta}).
\end{aligned} \tag{4.18}$$

So there are 18 constraints in total since there are 6 such equations (4.16). However, it is obviously to notice that $\boldsymbol{C}_\alpha : (\hat{\boldsymbol{t}}_{\alpha\beta\gamma} \otimes \hat{\boldsymbol{t}}_{\alpha\beta\gamma}) = \boldsymbol{C}_\beta : (\hat{\boldsymbol{t}}_{\alpha\beta\gamma} \otimes \hat{\boldsymbol{t}}_{\alpha\beta\gamma})$ and $\boldsymbol{C}_\beta : (\hat{\boldsymbol{t}}_{\alpha\beta\gamma} \otimes \hat{\boldsymbol{t}}_{\alpha\beta\gamma}) = \boldsymbol{C}_\gamma : (\hat{\boldsymbol{t}}_{\alpha\beta\gamma} \otimes \hat{\boldsymbol{t}}_{\alpha\beta\gamma})$ can derive $\boldsymbol{C}_\alpha : (\hat{\boldsymbol{t}}_{\alpha\beta\gamma} \otimes \hat{\boldsymbol{t}}_{\alpha\beta\gamma}) = \boldsymbol{C}_\gamma : (\hat{\boldsymbol{t}}_{\alpha\beta\gamma} \otimes \hat{\boldsymbol{t}}_{\alpha\beta\gamma})$. Therefore, for each edge there is one dependency between these 18 constraints. So there are $18 - 4 = 14$ independent constraints of equations (4.16). Plus the additional 4 shear force balance constraints, the four CATs' degrees of freedom under constraints are $24 - 14 - 4 = 6$. $\square$

Proof of Claim: According to the Lemma, the four CATs has 6 degrees of freedom. We only need to proof that the 6 degrees is for a global symmetric tensor $\boldsymbol{C}$, and check whether $\boldsymbol{C}_\alpha = \boldsymbol{C}_\beta = \boldsymbol{C}_\gamma = \boldsymbol{C}_\delta = \boldsymbol{C}$ can satisfy all the constraints.

It is trivial that equations (4.16) are satisfied. As for the shear force balance (4.7), we need use CAT to express the shear force:

$$
\begin{aligned}
F^{(t)}_{\alpha\beta,\gamma} &= q_{\alpha\beta}\boldsymbol{B}_{\alpha\beta} : (\hat{\boldsymbol{n}}_{\alpha\beta,\gamma} \otimes \hat{\boldsymbol{t}}_{\alpha\beta\gamma}) \\
&= -q_{\alpha\beta}\boldsymbol{C} : .(\hat{\boldsymbol{t}}_{\alpha\beta\gamma} \otimes \hat{\boldsymbol{n}}_{\alpha\beta,\gamma}).
\end{aligned}
\tag{4.19}
$$

Therefore the equation (4.12) is equivalent to

$$
(\boldsymbol{C} \cdot \hat{\boldsymbol{t}}_{\alpha\beta\gamma}) \cdot (q_{\alpha\beta}\hat{\boldsymbol{n}}_{\alpha\beta,\gamma} + q_{\beta\gamma}\hat{\boldsymbol{n}}_{\beta\gamma,\alpha} + q_{\gamma\alpha}\hat{\boldsymbol{n}}_{\gamma\alpha,\beta}) = 0. \tag{4.20}
$$

This is true because the second bracket is exactly the dual triangle equation. So we have proved that the four CATs to be equal will satisfy all the force balance equations at the edges. □

The equivalence of CATs (4.17) implies that for a cellular aggregate, there exist a global anisotropy tensor $\boldsymbol{C}$ that equals to every CAT. Consequently, in a cellular aggregate, the anisotropic surface tension of membrane $M_{\alpha\beta}$ is

$$
\boldsymbol{T}_{\alpha\beta} = -q_{\alpha\beta}(\hat{\boldsymbol{m}}_{\alpha\beta} \times \boldsymbol{C} \times \hat{\boldsymbol{m}}_{\alpha\beta}), \tag{4.21}
$$

which can satisfy the tension balance on edges. When $\boldsymbol{C} = b\boldsymbol{I}$ is an isotropic tensor, then the system is degenerated to scenario of isotropic surface tensions.

4.2.5. Conclusion

An anisotropic surface tension is an in-plane stress tensor. It applies different normal forces and shear forces on different edges. A cellular aggregate in equilibrium is the Polyhedron tessellation that normal forces and shear forces are balanced at each edge. By investigating this multi-cellular system, we discover the analytical solutions of anisotropic tensions and the free parameters.

Roughly speaking, though we allow the surface tension to be anisotropic, the magnitudes of tensions are still as in isotropic scenario. Although we allow each membrane surface tension has its own anisotropy, every membrane anisotropy is the projection to a global anisotropy tensor. Those consequences are the emergent simplicity from the complex system.

4.3. Anisotropic force balance on Ellipsoidal-Curved Polyhedral tessellation

After the theoretical analysis of anisotropic force balance on the cellular aggregates with uniform pressure, we start to generalize the theory into non-uniform pressure scenario. We first set up the mechanics in this system, including isotropic hydrostatic pressures and in-homogeneous and anisotropic surface tensions (4.3.1). We then consider the pressure-tension balance on membranes, find out the analytical solutions of anisotropic Young-Laplace relations on ellipsoidal interfaces (4.3.2). Then we investigate the tension balance on edges within a special class of Ellipsoidal-Curved Polyhedral tessellation (4.3.3 and 4.3.4). Consequently, we discover new emergent simplicity when we introduce more complexities into the system (4.3.5).

4.3.1. Assumptions

In the cellular aggregate, the intracellular pushing stress comes from the hydrostatic pressure within cell. Therefore, the cellular pressure should still be treated as an isotropic stress. Inside each cell volume, the stress balance requires the magnitude of pressure to be homogeneous, thus we use one scalar number P_α to represent it. However, the pressures of different cells are set to be different in this system.

Pressure difference in two sides of a membrane cause the curvature of it. In this model, we assume that the surface tension on the membrane to be anisotropic. However, this assumption does not induce the homogeneity of tensions on a curved membrane. More fundamentally, it is not a well-defined concept of homogeneity, because the tension is an in-plane tensor yet the tangential planes are different at different points of a curved face. But we still require the continuity of the tensor within the faces, in order to satisfy local in-plane tension balance on a smooth surface.

4.3.2. Anisotropic Young-Laplace relation

The Young-Laplace relation between pressure difference and anisotropic surface tensions can be derived using differential geometry knowledge [**35, 36, 37**]. We state the result here:

$$(P_\alpha - P_\beta)\hat{\boldsymbol{m}} = -\nabla_S \cdot \boldsymbol{T}_{\alpha\beta}. \tag{4.22}$$

In equation (4.22), $\hat{\boldsymbol{m}}$ represent the face normal, as shown in Figure 4.4. $\boldsymbol{T}_{\alpha\beta}$ is a surface stress tensor field which can be anisotropic and in-homogeneous. ∇_S represent the surface derivative. This equation is in vector form, since the tangent force balance is not guaranteed as in isotropic scenario. The normal direction of the equation (4.22) can be expressed as

$$P_\alpha - P_\beta = \frac{T_{11}}{R_1} + \frac{T_{22}}{R_2}, \tag{4.23}$$

where R_1 and R_2 are the principal radii of curvature, T_{11} and T_{22} are the stress components at these two principle directions.

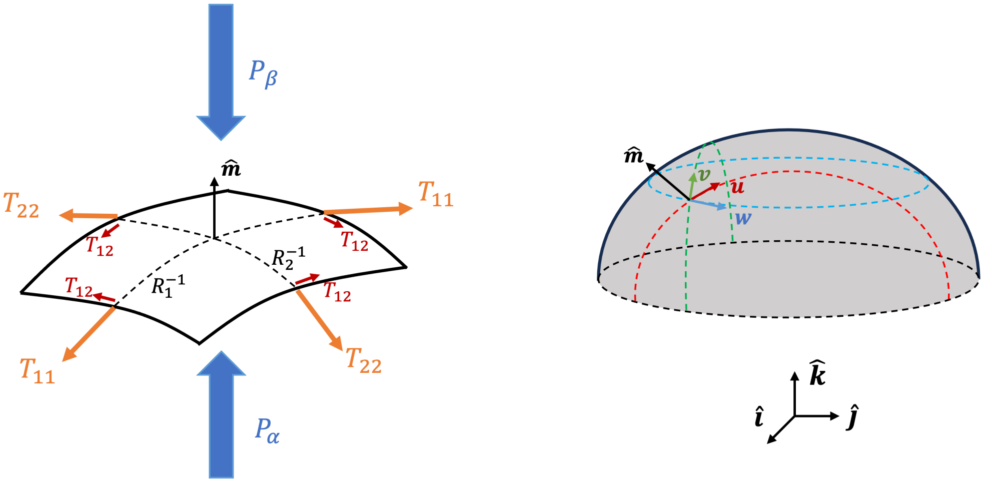

Figure 4.4. Anisotropic Young-Laplace relation

It is a pure mathematical question to find all possible solutions of surface shapes and stress tensor fields. But here we only introduce an analytical solution to this anisotropic Young-Laplace equation (4.22) on ellipsoids.

Claim: On an ellipsoid $\boldsymbol{r} = ax\hat{\boldsymbol{i}} + by\hat{\boldsymbol{j}} + cz\hat{\boldsymbol{k}}$ with $x^2 + y^2 + z^2 = 1$, the solution of stress tensor field that satisfy (4.22) is

$$\boldsymbol{T}_{\alpha\beta} = \frac{P_\alpha - P_\beta}{2}\boldsymbol{\sigma} = \frac{P_\alpha - P_\beta}{2l}\left[A\boldsymbol{u}\otimes\boldsymbol{u} + B\boldsymbol{v}\otimes\boldsymbol{v} + C\boldsymbol{w}\otimes\boldsymbol{w}\right]. \tag{4.24}$$

Here the vectors $\boldsymbol{u}, \boldsymbol{v}, \boldsymbol{w}$ are

$$\begin{aligned} \boldsymbol{u} &= zb\hat{\boldsymbol{j}} - yc\hat{\boldsymbol{k}}, \\ \boldsymbol{v} &= xc\hat{\boldsymbol{k}} - za\hat{\boldsymbol{i}}, \\ \boldsymbol{w} &= ya\hat{\boldsymbol{i}} - xb\hat{\boldsymbol{j}}, \end{aligned} \tag{4.25}$$

the coefficients A, B, C are

$$\begin{aligned} A &= \frac{1}{b^2} + \frac{1}{c^2} - \frac{1}{a^2}, \\ B &= \frac{1}{c^2} + \frac{1}{a^2} - \frac{1}{b^2}, \\ C &= \frac{1}{a^2} + \frac{1}{b^2} - \frac{1}{c^2}, \end{aligned} \tag{4.26}$$

and the length scale l is

$$l = \sqrt{\frac{x^2}{a^2} + \frac{y^2}{b^2} + \frac{z^2}{c^2}}. \tag{4.27}$$

Proof: We introduce some preliminary facts before the proof. First, the surface normal of the ellipsoid at $\boldsymbol{r} = ax\hat{\boldsymbol{i}} + by\hat{\boldsymbol{j}} + cz\hat{\boldsymbol{k}}$ is

$$\hat{\boldsymbol{m}} = \frac{x}{al}\hat{\boldsymbol{i}} + \frac{y}{bl}\hat{\boldsymbol{j}} + \frac{z}{cl}\hat{\boldsymbol{k}}. \tag{4.28}$$

It is easy to check

$$\hat{\boldsymbol{m}} \cdot \boldsymbol{u} = \hat{\boldsymbol{m}} \cdot \boldsymbol{v} = \hat{\boldsymbol{m}} \cdot \boldsymbol{w} = 0. \tag{4.29}$$

So $\boldsymbol{u}, \boldsymbol{v}, \boldsymbol{w}$ are all tangent directions of ellipsoid, thus the solution (4.24) is a stress tensor in the tangential plane.

The directional derivatives are defined as

$$\nabla = (\frac{\partial}{\partial r_1}, \frac{\partial}{\partial r_2}, \frac{\partial}{\partial r_3}) = (\frac{1}{a}\frac{\partial}{\partial x}, \frac{1}{b}\frac{\partial}{\partial y}, \frac{1}{c}\frac{\partial}{\partial z}). \tag{4.30}$$

The surface divergence of any vector field $\boldsymbol{\tau}$ is defined as

$$\nabla_S \cdot \boldsymbol{\tau} = \nabla \cdot \boldsymbol{\tau} - \nabla \boldsymbol{\tau} : (\hat{\boldsymbol{m}} \otimes \hat{\boldsymbol{m}}). \tag{4.31}$$

The surface divergence of a tensor field $\boldsymbol{\sigma}$ is a vector field $\nabla_S \cdot \boldsymbol{\sigma}$ that each component is defined as

$$(\nabla_S \cdot \boldsymbol{\sigma}) \cdot \hat{\boldsymbol{\imath}} = \nabla_S \cdot (\boldsymbol{\sigma}^T \cdot \hat{\boldsymbol{\imath}}). \tag{4.32}$$

And this equation is the same for component on $\hat{\boldsymbol{\jmath}}$ and $\hat{\boldsymbol{k}}$ direction.

Now, the Young-Laplace equation (4.22) is equivalent to $2l\hat{\boldsymbol{m}} = \nabla_S \cdot \boldsymbol{\sigma}$. Proving this is equivalent to prove

$$-\frac{2x}{al} = \nabla_S \cdot (\boldsymbol{\sigma}^T \cdot \hat{\boldsymbol{\imath}}). \tag{4.33}$$

Since $\boldsymbol{u} \cdot \hat{\boldsymbol{\imath}} = 0$, $\boldsymbol{v} \cdot \hat{\boldsymbol{\imath}} = -za$, $\boldsymbol{u} \cdot \hat{\boldsymbol{\imath}} = ya$, we have

$$\boldsymbol{\sigma}^T \cdot \hat{\boldsymbol{\imath}} = \boldsymbol{\sigma} \cdot \hat{\boldsymbol{\imath}} = \frac{1}{l}(-Baz\boldsymbol{v} + Cay\boldsymbol{w}). \tag{4.34}$$

Therefore, the surface divergence of this vector field is

$$\nabla_S \cdot (\boldsymbol{\sigma}^T \cdot \hat{\boldsymbol{\imath}}) = -Ba\nabla_S \cdot \left(\frac{z\boldsymbol{v}}{l}\right) + Ca\nabla_S \cdot \left(\frac{y\boldsymbol{w}}{l}\right) \tag{4.35}$$

Let us first compute $\nabla(z\boldsymbol{v}/l)$ using (4.25), (4.27), (4.30) as following:

$$\begin{aligned}\nabla\left(\frac{z\boldsymbol{v}}{l}\right) &= \frac{1}{l}\nabla(z\boldsymbol{v}) + z\boldsymbol{v}\otimes\nabla\frac{1}{l}\\ &= \frac{1}{l}\begin{bmatrix} 0 & 0 & -2az/c \\ 0 & 0 & 0 \\ cz/a & 0 & x \end{bmatrix} - \begin{bmatrix} -az^2 \\ 0 \\ czx \end{bmatrix}\begin{bmatrix} \frac{x}{a^3l^3} & \frac{y}{b^3l^3} & \frac{z}{c^3l^3}\end{bmatrix}.\end{aligned} \tag{4.36}$$

So the divergence $\nabla\cdot(z\boldsymbol{v}/l)$ is the trace of matrix:

$$\nabla\cdot\left(\frac{z\boldsymbol{v}}{l}\right) = \frac{x}{l} - \frac{z^2x}{l^3}\left(\frac{1}{c^2} - \frac{1}{a^2}\right). \tag{4.37}$$

It is not hard to compute the tensor component at normal direction:

$$\left(\nabla\frac{z\boldsymbol{v}}{l}\right) : (\hat{\boldsymbol{m}}\otimes\hat{\boldsymbol{m}}) = \frac{z^2x}{l^3}\left(\frac{1}{a^2} - \frac{1}{c^2}\right). \tag{4.38}$$

Thus according to the definition of surface divergence (4.31), we have

$$\nabla_S\cdot\left(\frac{z\boldsymbol{v}}{l}\right) = \nabla\cdot\left(\frac{z\boldsymbol{v}}{l}\right) - \left(\nabla\frac{z\boldsymbol{v}}{l}\right) : (\hat{\boldsymbol{m}}\otimes\hat{\boldsymbol{m}}) = \frac{x}{l}. \tag{4.39}$$

In the similar way, we compute

$$\nabla_S\cdot\left(\frac{y\boldsymbol{w}}{l}\right) = -\frac{x}{l}. \tag{4.40}$$

Therefore, take (4.39) and (4.40) into equation (4.35), we have

$$\nabla_S\cdot(\boldsymbol{\sigma}^T\cdot\hat{\boldsymbol{\imath}}) = -Ba\frac{x}{l} + Ca\left(-\frac{x}{l}\right) = -\frac{2x}{al}, \tag{4.41}$$

which is the equation (4.33) we intend to prove. Therefore, the tensor field $\boldsymbol{T}_{\alpha\beta} = (P_\alpha - P_\beta)\boldsymbol{\sigma}/2$ is the solution to Young-Laplace equation. $\square$

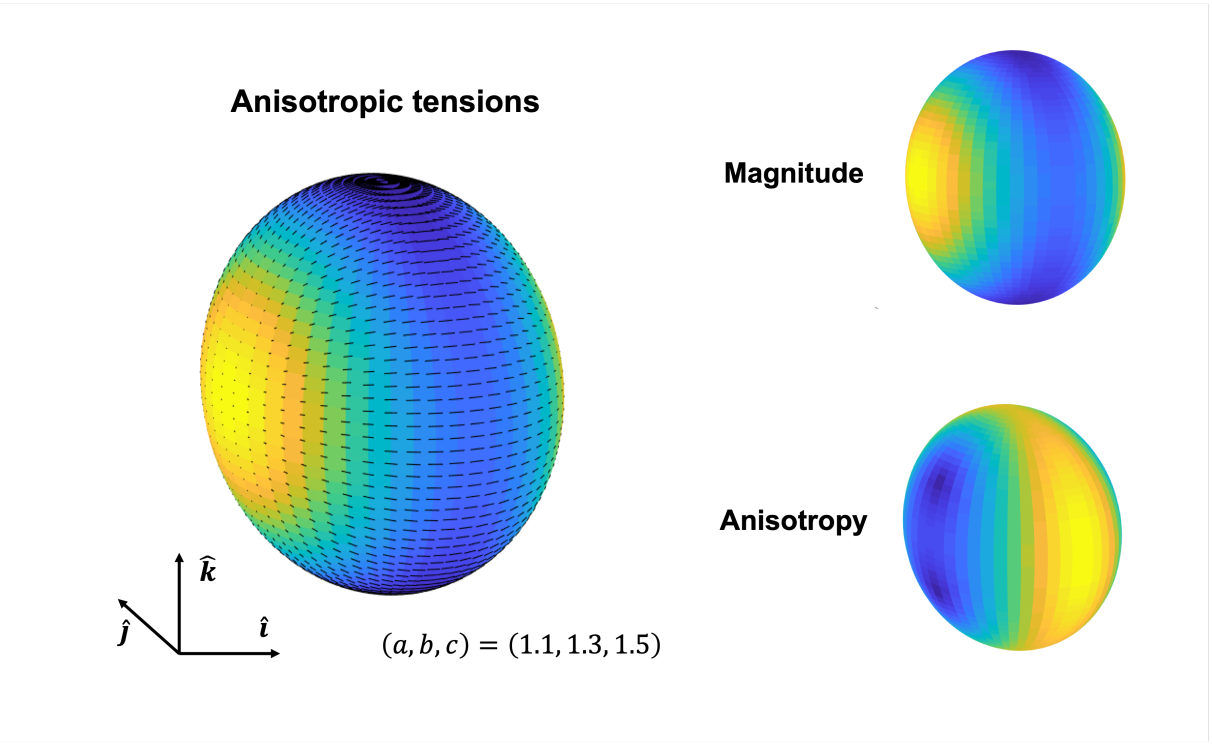

Figure 4.5. Analytical solution of anisotropic tension on ellipsoid

In Figure 4.5, we present the analytical solution of anisotropic tension on an ellipsoid. Three values are needed to fully represent an in-plane stress tensor: the trace of the tensor matrix, which is shown by color in Figure 4.5 to present the overall magnitude of the stress; the larger principle direction of the tensor matrix, which is shown by the short lines in Figure 4.5 present the anisotropic direction; the ratio of two eigenvalues of the tensor matrix, which is shown by the length of the short lines in Figure 4.5, to present the amount of anisotropy.

4.3.3. Ellipsoidal-Curved Polyhedral tessellation

It is a hard pure mathematical question that what is the possible 3d tessellation that is tilling by sections of ellipsoids. First, it is not assured that the interaction line of two ellipsoids is an elliptical curve. Thus it is further complicated to figure out the geometric constraints of the ellipsoids in the tessellation, since each curved edge is the common intersection of three ellipsoids. Second, if we only consider the tessellations that all edges are elliptical, it is still hard to parameterize the space of possible tessellations. Third, even if we can parameterize all the ellipsoid tessellations, it is not easy to verify the tension balance relations on every edge.

Here we only consider the Ellipsoidal-Curved Polyhedral tessellations that generalized from SCP tessellations. In this special class of tessellations, every ellipsoid section is 'stretched' by the corresponding sphere section in SCP tessellation. The 'stretchiness' can be given by a three-dimensional symmetric tensor $\boldsymbol{S}$. A point $\boldsymbol{r}$ on a sphere is thus moved to a new position $\boldsymbol{S}\cdot\boldsymbol{r}$. We also require the same stretch tensor $\boldsymbol{S}$ for every sphere section in SCP tessellation, in order to avoid mismatch of the edge interaction of three ellipsoids.

4.3.4. Tension balance on elliptical edges

Now the question is, could the three anisotropic surface tensions can be balanced on the elliptical edge in such Ellipsoidal-Curved Polyhedral tessellation? In order to answer this question, we will use the ideas of CAT and MAT in Polyhedral tessellation.

For a spherical membrane $M_{\alpha\beta}$ in SCP tessellation, there is a local dual line $\boldsymbol{q}^*_{\alpha\beta}(\boldsymbol{r})$ with respect to any point $\boldsymbol{r} = Rx\hat{\boldsymbol{\imath}} + Ry\hat{\boldsymbol{\jmath}} + Rz\hat{\boldsymbol{k}}$ on the sphere. Now, if we 'stretch' the sphere by $\boldsymbol{S} = a\hat{\boldsymbol{\imath}} \otimes \hat{\boldsymbol{\imath}} + b\hat{\boldsymbol{\jmath}} \otimes \hat{\boldsymbol{\jmath}} + c\hat{\boldsymbol{k}} \otimes \hat{\boldsymbol{k}}$, then the dual line will be stretched by $\boldsymbol{S}^{-1} = a^{-1}\hat{\boldsymbol{\imath}} \otimes \hat{\boldsymbol{\imath}} + b^{-1}\hat{\boldsymbol{\jmath}} \otimes \hat{\boldsymbol{\jmath}} + c^{-1}\hat{\boldsymbol{k}} \otimes \hat{\boldsymbol{k}}$. After this stretching, the direction of the dual line change from the sphere normal $\hat{\boldsymbol{m}} = x\hat{\boldsymbol{\imath}} + y\hat{\boldsymbol{\jmath}} + z\hat{\boldsymbol{k}}$ to the ellipse normal $\hat{\boldsymbol{m}} = \frac{x}{al}\hat{\boldsymbol{\imath}} + \frac{y}{bl}\hat{\boldsymbol{\jmath}} + \frac{z}{cl}\hat{\boldsymbol{k}}$, and the length of the dual line change to $q^*_{\alpha\beta}l$. Here the length scale l is defined as in (4.27).

Suppose the cellular pressure maintains previous value after stretching, then at the new point $\boldsymbol{r} = Rax\hat{\boldsymbol{\imath}} + Rby\hat{\boldsymbol{\jmath}} + Rcz\hat{\boldsymbol{k}}$ on the ellipse, the tension becomes

$$\boldsymbol{T}_{\alpha\beta} = q^*_{\alpha\beta} l \boldsymbol{B}_{\alpha\beta} = q^*_{\alpha\beta} l \left[\frac{A}{l^2} \boldsymbol{u} \otimes \boldsymbol{u} + \frac{B}{l^2} \boldsymbol{v} \otimes \boldsymbol{v} + \frac{C}{l^2} \boldsymbol{w} \otimes \boldsymbol{w} \right], \tag{4.42}$$

where A, B, C and $\boldsymbol{u}, \boldsymbol{v}, \boldsymbol{w}$ is as defined in (4.26) and (4.25). Here the tensor $\boldsymbol{B}_{\alpha\beta}$ is the MAT as in the Polyhedral tessellation scenario. We realize that this tensor is a projection of a three-dimensional tensor:

$$\boldsymbol{B}_{\alpha\beta} = -\hat{\boldsymbol{m}} \times \boldsymbol{C}_0 \times \hat{\boldsymbol{m}}, \tag{4.43}$$

with the definition

$$\boldsymbol{C}_0 = b^2c^2A\hat{\boldsymbol{\imath}} \otimes \hat{\boldsymbol{\imath}} + c^2a^2B\hat{\boldsymbol{\jmath}} \otimes \hat{\boldsymbol{\jmath}} + a^2b^2C\hat{\boldsymbol{k}} \otimes \hat{\boldsymbol{k}}. \tag{4.44}$$

We notice that the tensor $\boldsymbol{C}_0$ is a global CAT as in Polyhedral tessellation scenario.

Therefore, the tension balance on the elliptical edge is easy to get. At a point on edge $E_{\alpha\beta\gamma}$, let us consider the three tangential planes with respect to the three ellipsoids. For these three planes, the three corresponding stretched dual lines - $q^*_{\alpha\beta}l_{\alpha\beta}\hat{\boldsymbol{m}}_{\alpha\beta}$, $q^*_{\beta\gamma}l_{\beta\gamma}\hat{\boldsymbol{m}}_{\beta\gamma}$ and $q^*_{\gamma\alpha}l_{\gamma\alpha}\hat{\boldsymbol{m}}_{\gamma\alpha}$ - can form a dual triangle. The three anisotropic tensions that in the three planes are $q^*_{\alpha\beta} l_{\alpha\beta} \boldsymbol{B}_{\alpha\beta}$, $q^*_{\beta\gamma} l_{\beta\gamma} \boldsymbol{B}_{\beta\gamma}$ and $q^*_{\gamma\alpha} l_{\gamma\alpha} \boldsymbol{B}_{\gamma\alpha}$, respectively. Following the same proving steps as in the Polyhedral tessellation scenario, since the MATs - $\boldsymbol{B}_{\alpha\beta}$, $\boldsymbol{B}_{\beta\gamma}$ and $\boldsymbol{B}_{\gamma\alpha}$ - are projections of the global tensor $\boldsymbol{C}_0$, the normal tension balance and shear force balance are satisfied.

4.3.5. Conclusion

We emphasize here that we only consider a special class of the possible geometry of cellular aggregates that anisotropic surface tensions and pressure differences and be balanced. Even though, we discover the simplicity emerge from the complex setups. The anisotropic surface tensions are allowed to be in-homogeneous on curved membranes, which induces a lot of complexity since we cannot use countable number of parameters to describe it. However, to balance with pressure differences, the solution of the tension anisotropy is the projection of a global tensor that defined by the eccentricity of the ellipsoid. More surprisingly, such anisotropy conserves the tension balance on elliptical edges.

4.4. Anisotropic force inference

The theoretical results on the multicellular system with anisotropic tensions enable the possibility of constructing a force inference method. However, many mathematical assumptions need to be verified before we develop the techniques, the most important one of which is the ellipsoidal shapes of the membrane. Here we only discuss the central ideas of reconstructing the eccentricity of membrane faces.

We have constructed the analytical inverse mapping from Ellipsoidal-Curved Polyhedral (ECP) tessellation to the values of anisotropic tensions and pressures. To do the force inference, we only need to reconstruct the geometry parameters of ECP tessellation from the three-dimensional images. Since an ECP tessellation is stretched from a SCP tessellation, the parameters we are going to fit is the SCP parameters Ψ and the stretchiness $\boldsymbol{S}$. Inversely, a ECP tessellation can be stretched back to SCP tessellation by $\boldsymbol{S}^{-1}$, and then we can do the least-square fitting on the SCP tessellation. The loss function can be written as following:

$$E(\Psi, \boldsymbol{S}) = \frac{1}{N} \sum_{M_{\alpha\beta}} \sum_{i=1}^{n_{\alpha\beta}} \left[|\boldsymbol{S}^{-1} \cdot \boldsymbol{r}_{\alpha\beta}^{(i)} - \boldsymbol{\rho}_{\alpha\beta}(\Psi)| - R_{\alpha\beta}(\Psi) \right]^2 . \tag{4.45}$$

The initial guess of the symmetric tensor $\boldsymbol{S}$ can be set as identical matrix $\boldsymbol{I}_3$, and the trace of $\boldsymbol{S}$ should be constrained.

In the future, we will apply the least-square fitting method onto the synthetic image data and real live-images to verify the accuracy and sensitivity of it.

CHAPTER 5

Dynamical model of embryo morphogenesis

5.1. Background

In previous chapters, the most important assumption we made when building the mechanical models is the mechanical equilibrium. This assumption comes from the observation of laser ablation experiment, where we discover the timescale of mechanical response is much smaller than the timescale of developmental movement. By this assumption, we are able to decouple the geometry and mechanics, and build the force balance equations which map a mechanical state to a certain geometric state.

However, in some morphogenesis processes that cellular movement is fast, such as germ-band extension process in drosophila embryos, the dynamical effects of movement cannot be neglected. In the physical aspects, the tissues in development are viscoelastic materials. When the timescale of movement speed is relatively large, the system is likely to perform as fluid rather than solid. In this case, the passive forces like viscosity need to be included into the model, and thus should be considered in the force inference method.

In fact, the studies of dynamical force inference started before the static inference method. In these studies [**38**], we take a video instead of an image at a certain timepoint to do the inference. However, these methods do not notice the fact that cellular geometry is close to the equilibrium, thus the inverse mapping is very sensitive. In this chapter, we take use of the theoretical consequences in static force inference and construct a robust method of dynamical force inference. In order to build the fundamental ideas and avoid the challenges in three dimensions, we only discuss the dynamics in two-dimensional cellular lattice.

5.2. Dynamical model on 2d cellular lattice

The geometry of two-dimensional cellular lattice is commonly quantified as a polygonal tessellation. In the similar way as in three-dimensional cases, we denote the polygonal shapes as cell C_α, denote the boundary edges between two cells as membranes $M_{\alpha\beta}$, and denote the vertices where three cells meet as $\boldsymbol{r}_{\alpha\beta\gamma}$.

As for modeling the mechanics, we assume the cellular pressures to be uniform across the two-dimensional lattice, and only consider the tensions on the membrane. Therefore, we do not consider the curvatures of membranes, the shape of each cell is a polygon whose edges are straight lines. We denote the membrane tension at $M_{\alpha\beta}$ as $T_{\alpha\beta}$, and the force direction is along the membrane from one vertex to another vertex.

As for the dynamics, we assume the movement of cells causes the resistance that is applying on the vertices. The resistance is proportional to the velocity of a vertex $\boldsymbol{r}_{\alpha\beta\gamma}$, is given by

$$\boldsymbol{F}^{(r)}_{\alpha\beta\gamma} = -\mu \frac{d\boldsymbol{r}_{\alpha\beta\gamma}}{dt}. \tag{5.1}$$

Here the parameter μ is a global constant representing the viscosity or fraction factor. In biological point of view, the resistance of epithelial cells comes from the relative movement to the basal substance.

Therefore, for each vertex, we can build the mechanical relations between active forces - membrane tensions - and passive forces - vertex resistance. The equation is given as

$$T_{\alpha\beta}\hat{\boldsymbol{t}}_{\alpha\beta} + T_{\beta\gamma}\hat{\boldsymbol{t}}_{\beta\gamma} + T_{\gamma\alpha}\hat{\boldsymbol{t}}_{\gamma\alpha} = \mu\frac{d\boldsymbol{r}_{\alpha\beta\gamma}}{dt}. \tag{5.2}$$

Here the unit vectors $\hat{\boldsymbol{t}}_{\alpha\beta}$ represent the membrane directions.

This dynamical model is coupling the geometric information (edge angles), the mechanical information (membrane tensions) and the kinetic information (vertex movements), and is of a collective system, the cellular array. Although the topological information and its transformation is also important during embryogenesis, we mainly focus on the tissue's mechanical states where topology takes only small role on that. We simply assume the topology information is given and not change over the timepoints we investigate. For the a multicellular system, the dynamical equation (5.2) can be written in matrix form:

$$\underline{\underline{G}}\underline{T} = \underline{f}. \tag{5.3}$$

Here $\underline{T} = [T_{\alpha\beta}, T_{\alpha\gamma}, ...]^t$ is the 1d matrix of tensions, and $\underline{f} = [f_{1x}, f_{1y}, f_{2x}, f_{2y}, ...]^t$ is the friction matrix. The 2D geometry matrix $\underline{\underline{G}} = G(\underline{r})$ includes the information of edge angles, and is defined by vertex locations $\underline{r}$. The system is a linear mechanical relation.

Our first interest to the dynamical system is the equilibrium states, also known as the fixed points of dynamical equations. This happens when the right-hand-side of equation (5.3) is 0, which is what we discussed in previous chapters. Noll et al's work [**28**] has shown that under this circumstance, neither the geometry and the mechanical state is

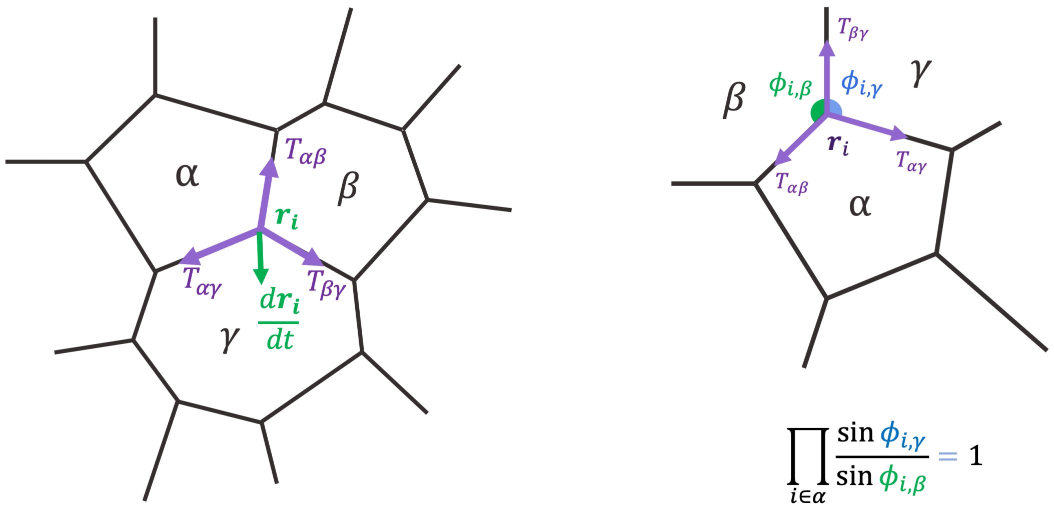
α
$T_{\alpha\beta}$
β
$\boldsymbol{r_i}$
$T_{\alpha\gamma}$
$T_{\beta\gamma}$
$\frac{d\boldsymbol{r_i}}{dt}$
γ
$T_{\beta\gamma}$
β
$\phi_{i,\beta}$
$\phi_{i,\gamma}$
γ
$\boldsymbol{r_i}$
$T_{\alpha\beta}$
$T_{\alpha\gamma}$
α
$\prod_{i\in\alpha}\frac{\sin\phi_{i,\gamma}}{\sin\phi_{i,\beta}}=1$

Figure 5.1. Dynamical model on 2d cellular lattice

free to choose. Here we re-illustrate the observations from counting the dimensionality of geometry space and mechanical space.

We use N_C, N_E and N_V denoting the number of cells, edges and vertices, respectively. Euler's topology rule tells us $N_C + N_V - N_E = 1$ in two dimensions. Besides, since each vertex is an end of three edges, there should be $2N_E = 3N_V$. The two relations point out that $N_V \approx 2N_C$ and $N_E \approx 3N_C$ when the right-hand-side 1 is neglected for large number of cells N_C. Obviously, the polygonal tessellation is fully defined by the vertex locations once the topology information is given, thus the dimensionality is $2N_V = 4N_C$. As for the mechanical space, each membrane has a value of tension, thus the dimensionality is $N_E = 3N_C$.

If three tensions are balanced at a vertex, the ratio of tensions is given by the edge angles:

$$\frac{T_{\alpha\beta}}{\sin\phi_{i,\gamma}} = \frac{T_{\beta\gamma}}{\sin\phi_{i,\alpha}} = \frac{T_{\gamma\alpha}}{\sin\phi_{i,\beta}}. \tag{5.4}$$

Here the angles are as shown in the right panel of Figure 5.1. Under equilibrium, while tension balance is satisfied everywhere, consider the vertices around one cell C_α, the edge angles must satisfy

$$\prod_{i\in\alpha} \frac{\sin\phi_{i,\gamma}}{\sin\phi_{i,\beta}} = \prod_{i\in\alpha} \frac{T_{\alpha\beta}}{T_{\alpha\gamma}} = 1. \tag{5.5}$$

It sets a constraint to the edge angles around each cell. So there are N_C constraints in total, thus the geometry subspace of equilibrium is $3N_C$ dimensional. As discussed in three-dimensional scenario, the subspace can be parameterized by weighted Voronoi tessellation, where the parameters are $\Psi = \{\boldsymbol{q}_\alpha, \theta_\alpha\}_{\alpha=1,2,\ldots,N_C}$. There are also dualities between geometry and mechanics, and we realize that the corresponding dual networks of have $2N_C$ degrees of freedom.

5.3. Dynamical force inference method

As we illustrate, the dynamical model is coupling the geometric information, the mechanical information and the kinetic information. While the geometric and kinetic information are easily measured from the video of imaging cell boundary markers, there is no direct and non-invasive measurement on membrane tension. Although all the geometric and kinetic information can be measured by image analysis, the measurement errors will increase the rank of the geometry matrix $\underline{\underline{G}}$, thus make the linear system unsolvable.

For a general linear problem $\underline{\underline{A}}\underline{x} = \underline{b}$, the classic method of solving for the best fitted solution is to minimize $||\underline{\underline{A}}\underline{x} - \underline{b}||$. The solution is $\underline{x} = \tilde{\underline{\underline{A}}}^{-1}\underline{b}$, where $\tilde{\underline{\underline{A}}}^{-1}$ is the pseudo-inverse matrix of $\underline{\underline{A}}$. This method is proved not robust in equilibrium force inference, in which case $\underline{b} = 0$. Physically speaking, in this method we trust the geometry measurement $\underline{\underline{A}}$ and try to minimize velocity noise. The idea of increasing the robustness of equilibrium force inference is to find the closest equilibrium geometry to the measurement. In algebra, we try to find the best fitted matrix $\underline{\underline{A}}^*$ which guarantee the existence of exact solution of $\underline{\underline{A}}^*\underline{x} = \underline{0}$. The definition of 'distance' is the deviation of vertex location. The observed geometry matrix is $\underline{\underline{A_0}} = A(\underline{r})$, while the best fitted matrix is $\underline{\underline{A}}^* = A(\underline{r} + \underline{\epsilon})$, denoting $\underline{\underline{A_\epsilon}}$.

Let's generalize the idea to dynamic force inference. We try to find the closest geometry and velocity $\underline{\underline{A}}^*$ and $\underline{b}^*$ that there exists exact solution of $\underline{\underline{A}}^*\underline{x} = \underline{b}^*$. Similarly, $\underline{\underline{A}}^* = \underline{\underline{A_\epsilon}}$ and $\underline{b}^* = \underline{b} + \underline{\xi}$. The 'distance' is the combined deviation of geometry and velocity, $E = |\underline{\epsilon}|^2 + |\underline{\xi}|^2$. For a given $\underline{\epsilon}$, the smallest $\underline{\xi}$ is reached when $\underline{x} = \tilde{\underline{\underline{A_\epsilon}}}^{-1}\underline{b}$. Therefore, we can just minimize the distance as a function of $\underline{\epsilon}$:

$$E(\underline{\epsilon}) = |\underline{\epsilon}|^2 + |\underline{\xi}|^2 = |\underline{\epsilon}|^2 + |\underline{\underline{A_\epsilon}}(\tilde{\underline{\underline{A_\epsilon}}}^{-1}\underline{b}) - \underline{b}|^2. \tag{5.6}$$

In the MATLAB code, we use minimization function *fminunc* to get $\underline{\underline{A}}^*$. Besides, we should normalize $\underline{\epsilon}$ and $\underline{\xi}$ by the scale of membrane length $\bar{r}$ and the scale of friction $\bar{f}$. Besides, in order to have a better convergence rate, we constrain the geometry deviation $\underline{\epsilon}$ such that keeps the edge angles in $(0, \pi)$.

In order to investigate the robustness, we take use of a two-dimensional vertex model to simulate the epithelial tissue dynamics generating synthetic data. We add Gaussian noise on both geometry information and velocity information of the synthetic data, then

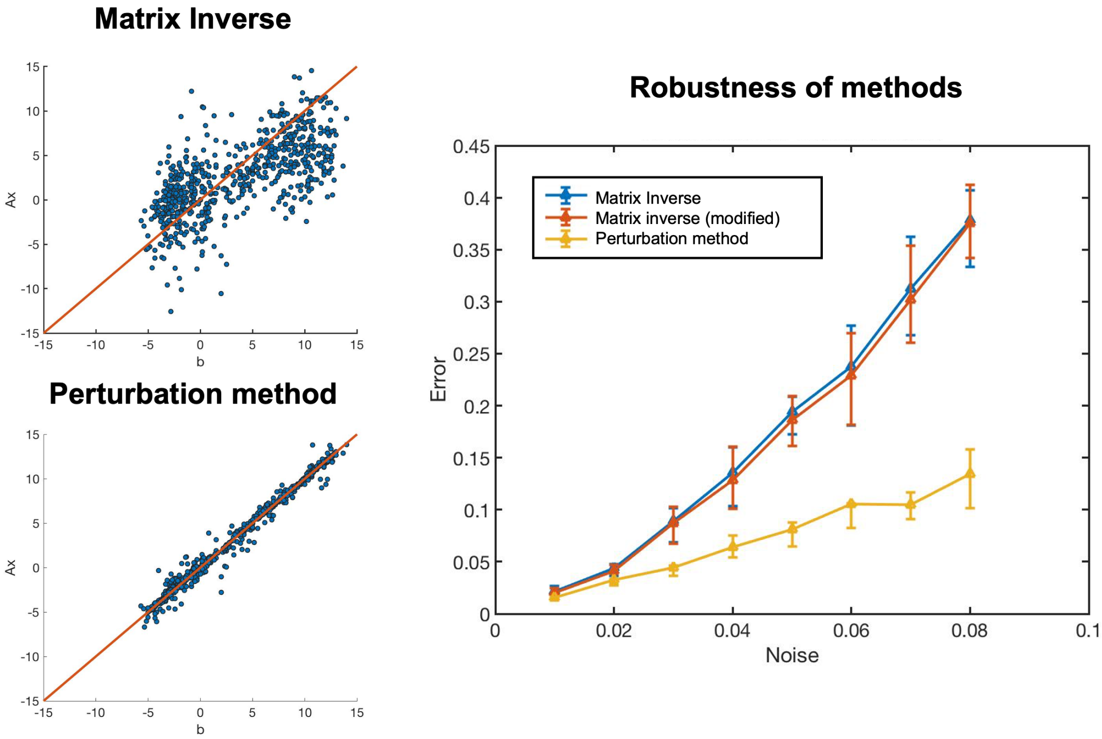

Figure 5.2. Robustness of dynamical force inference method

infer the forces based on the noisy 'measurements'. Comparing to the Matrix Inverse method, the solution by the perturbation method has less error. The fitting results are shown in Figure 5.2.

5.4. Results on drosophila germ-band extension

We then apply the dynamical force inference method onto the videos of drosophila germ-band extension. By image analysis on the video, we take the membrane geometries in the middle where the cell boundaries are well-segmented. We take the pixels that belong to three different cells as the vertex positions. From two subsequent images, we could measure the velocities of the vertices. Based on the geometry information and kinetic information, we could apply the dynamical force inference method to measure the mechanical patterns.

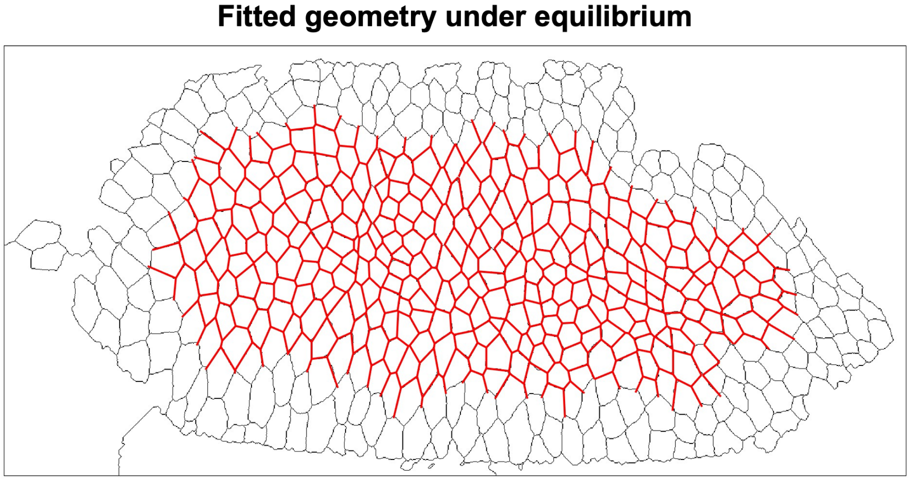

Fitted geometry under equilibrium

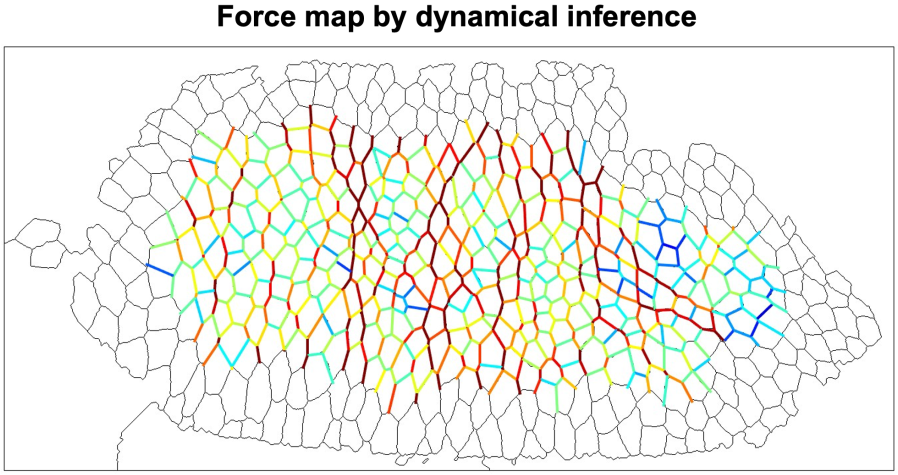

Force map by dynamical inference

Figure 5.3. Results on drosophila germ-band extension

Before applying the dynamical force inference, we first investigate the geometry of cellular lattice. In the top panel of Figure 5.3, we first show the fitting results of the equilibrium geometry, which is the subspace of general polygonal tessellations. The spatial-temporal fitting error distribution of the static geometry is less than 3%, from which we could confirm the small deviations between equilibrium tessellation to the observed tissue geometry.

In the bottom panel of Figure 5.3, we show the dynamical force inference results that provide the dynamical value of tension for each membrane. The tension pattern shows apparent anisotropy in vertical directions. This result implies that the membrane tensions along dorsal-ventral axis is higher than the membrane tensions along the anterior-posterior axis. This results meet to the known mechanisms in drosophila molecular data, which is an evidence that verifies our force inference method.

5.5. Mechanical-feedback model based on myosin-driven contractility

The quasi-static nature of germ-band extension in Drosophila indicates that some mechanical feedback always drives the system back to equilibrium. Given a mechanical state in the equilibrium subspace, equation (5.2) will drive the geometry state to its corresponding geometry equilibrium. However, if the given mechanical state is away from the $2N_C$ dimensional equilibrium subspace, the system will keep moving forever. So there must be some mechanical regulator that determines membrane tensions, and it must depend on the geometry information.

In microscopical view, the membrane tension comes from the actomyosin bundles along the cell boundary. Here we introduce the membrane 'rest length' l_{ij} of the underlying actomyosin filament and assume a simple elastic form:

$$T_{ij} = K(r_{ij} - l_{ij}), \tag{5.7}$$

where the constant K is the elastic module and $r_{ij} = |\vec{r}_i - \vec{r}_j|$ is the edge length. Under this model, for a given set of rest lengths $\underline{l}$, the dynamical system is going to converge to a geometry where the elastic energy function $El(\underline{r}) = \sum_{ij} \frac{1}{2}K(r_{ij} - l_{ij})^2$ reach to its minimum. We claim that the minimum exists since $El(\underline{r})$ is non-negative, and also that the minimum is unique because the dimensionality of rest length space is $N_F = 3N_C$, which is equal to the dimensionality of equilibrium subspace. The corresponding fixed points of geometry and mechanics are $\underline{r}^* = r^*(\underline{l})$ and $\underline{T}^* = T^*(\underline{l})$, which cannot be analytically expressed. Therefore, the rest length $\underline{l}$ is a latent coordinate of the equilibrium subspace.

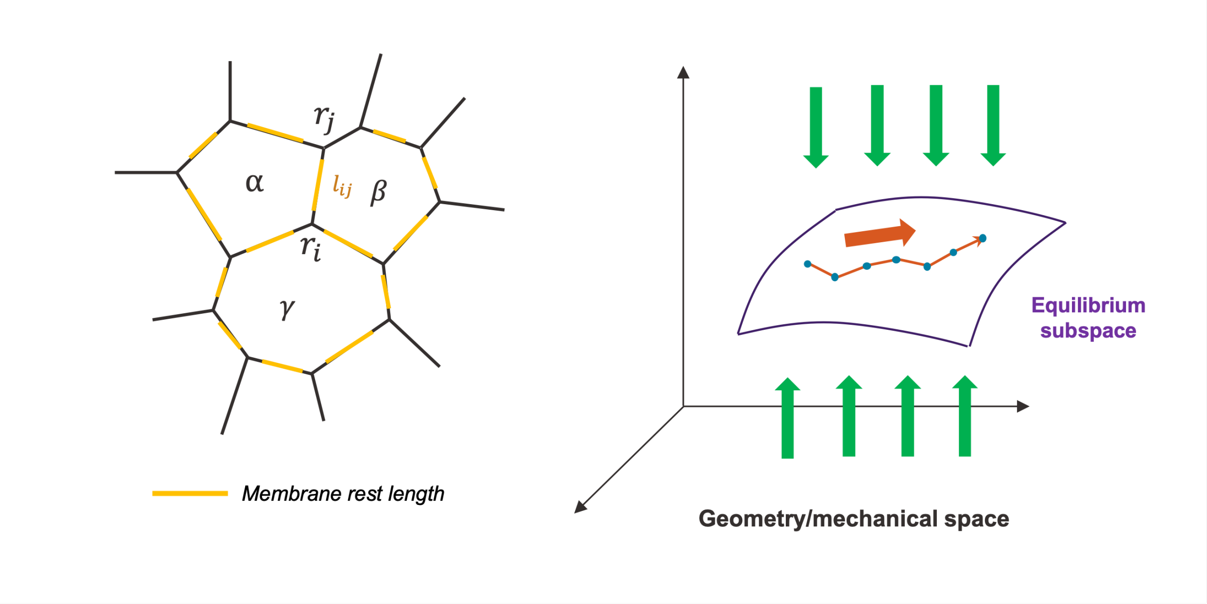

Figure 5.4. Mechanical and geoemtry subspace

However, the rest length is also a dynamical variable which is regulated by the myosin level m_{ij} on the membrane:

$$l_{ij}^{-1}\frac{dl_{ij}}{dt} = \tau_l^{-1} W\left(\frac{T_{ij}}{m_{ij} a T_S}\right). \tag{5.8}$$

The 'walking kernel' $W(x)$ determines the pace of myosin contracting the actin bundle, which is based on single-molecule experiments. While the load per myosin motor T_{ij}/am_{ij} reaches to the 'stall force' T_S, the actin bundle will stay at the its current length. For simplicity, the linearization of the equation around this fixed point can be expressed as

$$l_{ij}^{-1}\frac{dl_{ij}}{dt} = \alpha\left(\frac{T_{ij}}{\beta m_{ij}} - 1\right). \tag{5.9}$$

Additional to this dynamical model, we introduce a molecular information, the myosin density $\underline{m}$, which is encoded by genes. This system will reach to equilibrium while $\underline{T}^* = \beta\underline{m}^*$, i.e. the tensions are proportional to the myosin density. Because $\underline{T}^*$ is in $2N_C$ subspace, the equilibrium myosin $\underline{m}^*$ should also be in $2N_C$ subspace of a $F = 3N_C$ space. This indicates the myosin density is changable, and further there should be a feedback regulatory. One hypothesis on myosin feedback model is that myosin recruitment depends on the strain rate of rest length:

$$m_{ij}^{-1}\frac{dm_{ij}}{dt} = \gamma l_{ij}^{-1}\frac{dl_{ij}}{dt}, \tag{5.10}$$

where γ represents the recruitment rate. We assume the recruitment is slower than both mechanical relaxation and actomyosin contractile. We realize that this formula is analytically solvable. The solution is $m_{ij} = \lambda_{ij} l_{ij}^{\gamma}$ with the coefficient λ_{ij} determined by the initial state. And thus the stationary is reached when $\underline{T}^* = \beta\underline{\underline{\Lambda}}\underline{l}^{*\gamma}$. Here $\underline{\underline{\Lambda}}$ denotes the coefficient matrix with only diagonal elements $\underline{\lambda}$. Recall that we already have $\underline{T}^* = T^*(\underline{l}^*)$, thus the fixed point of $\underline{l}^*$ is at the solution of $\underline{x}$ for $T^*(\underline{x}) = \beta\underline{\underline{\Lambda}}\underline{x}^{\gamma}$. The solution exists and uniquely depends on $\underline{\lambda}$, which has $3N_C$ dimensionality.

CHAPTER 6

Discussion

6.1. Summary

The phenomena in morphogenesis is always simple that the cells seem to have group intelligence. But this simplicity is built on complex mechanisms in every level of biology. This big mystery is waiting for in-depth understanding from many aspects.

We aim to solve this mystery in morphogenesis from the aspect of mathematical modeling. We believe the keystone between complexity and simplicity is mechanics, thus we build the force inference methods to construct the mechanical atlas for embryos. We utilize the current advances in imaging techniques, applying the novel mathematical knowledge to parameterize the geometries in low-dimensional space and analytically solve the inverse problems. For the first time, we are able to know the 3d embryo mechanics spatially and temporally that cause the simple collective behavior.

On the other hand, in the context of ascidian gastrulation, we deepen our understanding of the complex foundations that produce the mechanical patterns. By the collaborations of biophysical mechanisms (cortical dynamics and hydrostatic states) and biochemical mechanisms (molecular and chemical gradient), at genetic level (cell-fate), molecular level (myosin reallocation) and cellular level (cell-cycle), the embryo makes a well-organized system that accomplishes the higher-level task.

6.2. Future

Apart from the theoretical tools and the biological insights that is provide in our study, the idea of bridging genotype to phenotype via mechanics is also worth exploring for other topics in developmental biology.

For a broader context of biology, there still remain many mysteries of observed emergent simplicity in every level. In evolution, simple trajectories emerge from the complex individual physiology and complex environmental selection. In ecology, simple successions emerge from the complex interactions between species and the complex interactions between life and environment. Those questions are also wait for in-depth understanding by us.

References

[1] Claudio Collinet and Thomas Lecuit. Programmed and self-organized flow of information during morphogenesis. *Nature Reviews Molecular Cell Biology*, 22(4):245–265, 2021.

[2] Lila Solnica-Krezel and Diane S Sepich. Gastrulation: making and shaping germ layers. *Annual review of cell and developmental biology*, 28:687–717, 2012.

[3] Joseph C Corbo, Anna Di Gregorio, and Michael Levine. The ascidian as a model organism in developmental and evolutionary biology. *Cell*, 106(5):535–538, 2001.

[4] Lance A Davidson, MAR Koehl, Raymond Keller, and George F Oster. How do sea urchins invaginate? using biomechanics to distinguish between mechanisms of primary invagination. *Development*, 121(7):2005–2018, 1995.

[5] Maria Leptin. Drosophila gastrulation: from pattern formation to morphogenesis. *Annual review of cell and developmental biology*, 11(1):189–212, 1995.

[6] Amy E Shyer, Alan R Rodrigues, Grant G Schroeder, Elena Kassianidou, Sanjay Kumar, and Richard M Harland. Emergent cellular self-organization and mechanosensation initiate follicle pattern in the avian skin. *Science*, 357(6353):811–815, 2017.

[7] Wen Yih Aw and Danelle Devenport. Planar cell polarity: global inputs establishing cellular asymmetry. *Current opinion in cell biology*, 44:110–116, 2017.

[8] Léo Guignard, Ulla-Maj Fiúza, Bruno Leggio, Julien Laussu, Emmanuel Faure, Gaël Michelin, Kilian Biasuz, Lars Hufnagel, Grégoire Malandain, Christophe Godin, et al. Contact area–dependent cell communication and the morphological invariance of ascidian embryogenesis. *Science*, 369(6500), 2020.

[9] Hanna L Sladitschek, Ulla-Maj Fiuza, Dinko Pavlinic, Vladimir Benes, Lars Hufnagel, and Pierre A Neveu. Morphoseq: Full single-cell transcriptome dynamics up to gastrulation in a chordate. *Cell*, 181(4):922–935, 2020.

[10] Barry M Gumbiner. Cell adhesion: the molecular basis of tissue architecture and morphogenesis. *Cell*, 84(3):345–357, 1996.

[11] Peter F Davies and Satish C Tripathi. Mechanical stress mechanisms and the cell. an endothelial paradigm. *Circulation research*, 72(2):239–245, 1993.

[12] Daniel A Fletcher and R Dyche Mullins. Cell mechanics and the cytoskeleton. *Nature*, 463(7280):485–492, 2010.

[13] Guillaume T Charras, Justin C Yarrow, Mike A Horton, L Mahadevan, and TJ Mitchison. Non-equilibration of hydrostatic pressure in blebbing cells. *Nature*, 435(7040):365–369, 2005.

[14] Christian Frantz, Kathleen M Stewart, and Valerie M Weaver. The extracellular matrix at a glance. *Journal of cell science*, 123(24):4195–4200, 2010.

[15] Lance Davidson and Ray Keller. Measuring mechanical properties of embryos and embryonic tissues. *Methods in cell biology*, 83:425–439, 2007.

[16] Karine Guevorkian, Marie-Josée Colbert, Mélanie Durth, Sylvie Dufour, and Françoise Brochard-Wyart. Aspiration of biological viscoelastic drops. *Physical review letters*, 104(21):218101, 2010.

[17] Jean-Léon Maître, Hélène Berthoumieux, Simon Frederik Gabriel Krens, Guillaume Salbreux, Frank Jülicher, Ewa Paluch, and Carl-Philipp Heisenberg. Adhesion functions in cell sorting by mechanically coupling the cortices of adhering cells. *science*, 338(6104):253–256, 2012.

[18] Kapil Bambardekar, Raphaël Clément, Olivier Blanc, Claire Chardès, and Pierre-François Lenne. Direct laser manipulation reveals the mechanics of cell contacts in vivo. *Proceedings of the National Academy of Sciences*, 112(5):1416–1421, 2015.

[19] Konstantin Doubrovinski, Michael Swan, Oleg Polyakov, and Eric F Wieschaus. Measurement of cortical elasticity in drosophila melanogaster embryos using ferrofluids. *Proceedings of the National Academy of Sciences*, 114(5):1051–1056, 2017.

[20] Matteo Rauzi, Pascale Verant, Thomas Lecuit, and Pierre-François Lenne. Nature and anisotropy of cortical forces orienting drosophila tissue morphogenesis. *Nature cell biology*, 10(12):1401–1410, 2008.

[21] Xiaoyan Ma, Holley E Lynch, Peter C Scully, and M Shane Hutson. Probing embryonic tissue mechanics with laser hole drilling. *Physical biology*, 6(3):036004, 2009.

[22] Otger Campàs, Tadanori Mammoto, Sean Hasso, Ralph A Sperling, Daniel O'connell, Ashley G Bischof, Richard Maas, David A Weitz, Lakshminarayanan Mahadevan, and Donald E Ingber. Quantifying cell-generated mechanical forces within living embryonic tissues. *Nature methods*, 11(2):183–189, 2014.

[23] Alessandro Mongera, Payam Rowghanian, Hannah J Gustafson, Elijah Shelton, David A Kealhofer, Emmet K Carn, Friedhelm Serwane, Adam A Lucio, James Giammona, and Otger Campàs. A fluid-to-solid jamming transition underlies vertebrate body axis elongation. *Nature*, 561(7723):401–405, 2018.

[24] Kaoru Sugimura, Pierre-François Lenne, and François Graner. Measuring forces and stresses in situ in living tissues. *Development*, 143(2):186–196, 2016.

[25] P Graham Cranston, Jim H Veldhuis, Sriram Narasimhan, and G Wayne Brodland. Cinemechanometry (cmm): A method to determine the forces that drive morphogenetic movements from time-lapse images. *Annals of biomedical engineering*, 38:2937–2947, 2010.

[26] Kevin K Chiou, Lars Hufnagel, and Boris I Shraiman. Mechanical stress inference for two dimensional cell arrays. *PLoS computational biology*, 8(5):e1002512, 2012.

[27] Silvanus Alt, Poulami Ganguly, and Guillaume Salbreux. Vertex models: from cell mechanics to tissue morphogenesis. *Philosophical Transactions of the Royal Society B: Biological Sciences*, 372(1720):20150520, 2017.

[28] Nicholas Noll, Madhav Mani, Idse Heemskerk, Sebastian J Streichan, and Boris I Shraiman. Active tension network model suggests an exotic mechanical state realized in epithelial tissues. *Nature physics*, 13(12):1221–1226, 2017.

[29] Nicholas Noll, Sebastian J Streichan, and Boris I Shraiman. Variational method for image-based inference of internal stress in epithelial tissues. *Physical Review X*, 10(1):011072, 2020.

[30] George E Davis, Kayla J Bayless, and Anil Mavila. Molecular basis of endothelial cell morphogenesis in three-dimensional extracellular matrices. *The Anatomical Record: An Official Publication of the American Association of Anatomists*, 268(3):252–275, 2002.

[31] Kandice R Johnson, Jennifer L Leight, and Valerie M Weaver. Demystifying the effects of a three-dimensional microenvironment in tissue morphogenesis. *Methods in cell biology*, 83:547–583, 2007.

[32] Kristin Sherrard, François Robin, Patrick Lemaire, and Edwin Munro. Sequential activation of apical and basolateral contractility drives ascidian endoderm invagination. *Current Biology*, 20(17):1499–1510, 2010.

[33] Yinan Wan, Katie McDole, and Philipp J Keller. Light-sheet microscopy and its potential for understanding developmental processes. *Annual review of cell and developmental biology*, 35:655–681, 2019.

[34] Edwin Munro, Jeremy Nance, and James R Priess. Cortical flows powered by asymmetrical contraction transport par proteins to establish and maintain anterior-posterior polarity in the early c. elegans embryo. *Developmental cell*, 7(3):413–424, 2004.

[35] Morton E Gurtin and A Ian Murdoch. A continuum theory of elastic material surfaces. *Archive for rational mechanics and analysis*, 57:291–323, 1975.

[36] Morton E Gurtin, Jorg Weissmüller, and Francis Larche. A general theory of curved deformable interfaces in solids at equilibrium. *Philosophical Magazine A*, 78(5):1093–1109, 1998.

[37] Tungyang Chen, Min-Sen Chiu, and Chung-Ning Weng. Derivation of the generalized young-laplace equation of curved interfaces in nanoscaled solids. *Journal of Applied Physics*, 100(7), 2006.

[38] G Wayne Brodland, Vito Conte, P Graham Cranston, Jim Veldhuis, Sriram Narasimhan, M Shane Hutson, Antonio Jacinto, Florian Ulrich, Buzz Baum, and Mark Miodownik. Video force microscopy reveals the mechanics of ventral furrow invagination in drosophila. *Proceedings of the National Academy of Sciences*, 107(51):22111–22116, 2010.

APPENDIX A

The MATLAB codes for numerical schemes

A.1. Force inference code

```
function Psi = force_inference(Cdat,Fdat,Psi,lmt)
%FORCE_INFERENCE Infer Voronoi parameters by minimizing error
    function
%   Cdat - Cellular information
%   Fdat - Face information
%   Psi - Voronoi parameters (power, weight, site)
%   lmt - Limitation of minimizing

cellnum = length(Cdat)-1;
check_real = isreal(error_function(Psi,Fdat));
while ~check_real
    Psi = Psi.*random('Normal',1,0.001,cellnum,5);
    check_real = isreal(error_function(Psi,Fdat));
end
pp = Psi(:,1);
Psi(:,1) = pp/mean(pp);
```

```
%% minimize error function
ef = @(psi)error_function(psi,Fdat);
options1 = optimoptions(@fmincon,'Display','iter','
   MaxFunctionEvaluations',2e5,'ObjectiveLimit',lmt);
Aeq = [ones(1,cellnum),zeros(1,cellnum*4)];
beq = cellnum;
lb = zeros(5*cellnum,1);
ub = [5*ones(cellnum,1);100*ones(cellnum,1);300*ones(cellnum
   *3,1)];
Psi = fmincon(ef,Psi,[],[],Aeq,beq,lb,ub,[],options1);

end




%%%%%%%%%%%%%%%%%%%%%%%%%%
function error = error_function(psi,Fdat)

psi = [0,0,0,0,0;psi];
error = 0;
pxn = 0;
```

```
for ii=1:length(Fdat)
    px = Fdat(ii).Pixels;
    c1 = Fdat(ii).Cells(1);
    c2 = Fdat(ii).Cells(2);
    p1 = psi(c1,1);
    p2 = psi(c2,1);
    q1 = psi(c1,3:5);
    q2 = psi(c2,3:5);
    t1 = psi(c1,2);
    t2 = psi(c2,2);
    rho = (p1*q1-p2*q2)/(p1-p2);
    r = sqrt(p1*p2*(q1-q2)*(q1-q2)'/(p1-p2)^2+(p1*t1^2-p2*t2
       ^2)/(p1-p2));
    ww = px-ones(size(px,1),1)*rho;
    dd = sqrt(sum(ww.^2,2));
    error = error+sum((dd-r).^2);
    pxn = pxn+size(px,1);
end

error = error/pxn;

end
```

A.2. Synthetic analysis

```
function ev = sensitivity_analysis(Cdat,Fdat)
%SENSITIVITY_ANALYSIS compute the eigenvalues of the inverse
   matrix
%    Cdat - Cellular information
%    Fdat - Face information
%    ev - Eigenvalues of inverse matrix

%% compute matrix size
nofc=length(Cdat)-1;
nofp=0;
nm=zeros(length(Fdat)+1);
for ii=1:length(Fdat)
    nofp=nofp+size(Fdat(ii).PixelN,1);
    nm(ii+1)=nofp;
end
M=zeros(nofp,nofc*5);
K=zeros(nofp,3);

%% set up the matrix and inverse
```

```
for ii=1:length(Fdat)
    px=Fdat(ii).PixelN;
    c1=Fdat(ii).Cells(1);
    c2=Fdat(ii).Cells(2);
    p1=Cdat(c1).Power;
    p2=Cdat(c2).Power;
    t1=Cdat(c1).Weight;
    t2=Cdat(c2).Weight;
    q1=Cdat(c1).Dual;
    q2=Cdat(c2).Dual;
    rho=(p1*q1-p2*q2)/(p1-p2);
    R=sqrt(p1*p2*(q1-q2)*(q1-q2)'/(p1-p2)^2+(p1*t1^2-p2*t2^2)
       /(p1-p2));
    ni=px-rho;
    rr=sqrt(sum(ni.^2,2))*ones(1,3);
    ni=(px-rho)./rr;
    c1=c1-1;
    c2=c2-1;
    if c1>0
        dq=p1*ni/(p1-p2)+p1*p2*(q1-q2)/(2*R*(p1-p2)^2);
        dt=p1*t1/(R*(p1-p2));
        dp=-p2*ni*(q1'-q2')/(p1-p2)^2-p2*((t1^2-t2^2)*(p1-p2)
           +(p1+p2)*(q1-q2)*(q1'-q2'))/(2*R*(p1-p2)^3);
        M(nm(ii)+1:nm(ii+1),5*c1-4)=dp;
        M(nm(ii)+1:nm(ii+1),5*c1-3)=dt;
        M(nm(ii)+1:nm(ii+1),5*c1-2:5*c1)=dq;
    end
    dq=p2*ni/(p2-p1)+p1*p2*(q2-q1)/(2*R*(p2-p1)^2);
    dt=p2*t2/(R*(p2-p1));
    dp=-p1*ni*(q2'-q1')/(p2-p1)^2-p1*((t2^2-t1^2)*(p2-p1)+(p1
       +p2)*(q1-q2)*(q1'-q2'))/(2*R*(p2-p1)^3);
    M(nm(ii)+1:nm(ii+1),5*c2-4)=dp;
    M(nm(ii)+1:nm(ii+1),5*c2-3)=dt;
    M(nm(ii)+1:nm(ii+1),5*c2-2:5*c2)=dq;
    K(nm(ii)+1:nm(ii+1),:)=ni;
end
ev = 1./svd(M);


end
```

Vita

Name:

Siqi Liu

Date and Place of Birth:

July 7th, 1995

Tai'an, China

Education:

- Bachelor of Engineering in Engineering Mechanics (Tsien Excellence in Education Program), Tsinghua University, Beijing, China, 2018
- Bachelor of Science in Mathematical Science and Applied Mathematics, Tsinghua University, Beijing, China, 2018
- Doctor of Philosophy in Applied Mathematics, Northwestern University, Evanston, IL, USA, 2023

Works:

- Liu, S., Lemaire, P., Munro, E., & Mani, M. (2022). A mathematical theory for the mechanics of three-dimensional cellular aggregates reveals the mechanical atlas for Ascidian embryogenesis. bioRxiv, 2022-11. (Preprint)